A MODIFIED ELASTO-PLASTIC PRESSURE DEPENDENT NUMERICAL COMBINED HARDENING MODEL FOR CHARACTERIZING PERMANENT DEFORMATION UNDER CYCLIC LOADING

A Dissertation

by

ATISH A. NADKARNI

Submitted to the Office of Graduate and Professional Studies of
Texas A&M University
in partial fulfillment of the requirements for the degree of

DOCTOR OF PHILOSOPHY

Chair of Committee,	Dallas N. Little
Co-Chair of Committee,	David H. Allen
Committee Members,	Robert L. Lytton
	Anastasia Muliana
	Masoud K. Darabi
	Navneet Garg
	John F. Rushing
Head of Department,	Robin Autenrieth

December 2020

Major Subject: Civil Engineering

ABSTRACT

Rutting is an extremely important load related distress in flexible pavements and is attributed to frequent passes of tire load, resulting in formation of longitudinal depression in the wheel track. This research developed a numerical model to capture the rutting in base layer, which is a critical aspect.

The isotropic Drucker-Prager model does not capture the evolution of yield surface beyond first few load cycles in the case of cyclic loading simulating frequent passes of aircraft tires. An elasto-plastic model having a progressively evolving yield surface with the introduction of a new parameter, γ, has been introduced in this dissertation. The mechanism allows yield surface to progressively evolve and reduce in size, even in the case of cyclic loading with constant load amplitudes such as a typical aircraft wheel.

It was reasoned that permanent deformation in elasto-plasticity occurs due to irreversible plastic strain. However, as the material is unloaded, the stress state returns to the elastic region. The proposed model results in further plastic deformation because the yield surface reduces in size; due to which the stress state in the next loading cycle lies outside the reduced yield surface.

Addition of the combined hardening model along with incorporation of γ parameter resulted in increased equivalent plastic strain and vertical plastic strain; thereby resulting in increased rutting.

Finally, refinements to the parameter γ were recommended in order to make the proposed model more realistic. These refinement are sought by researching through the fundamentals of the granular base material's micro-mechanics and conducting study on reverse-mapping the monotonic test stress-strain curve from cyclic tests.

DEDICATION

This dissertation is dedicated to my wife, Arti Sardessai Nadkarni, for her love and support. To my parents, Anjali and Anil Nadkarni without whom, nothing would have been possible for me.

To Manguirish Nadkarni for being a great brother.

To my dearest friends, whom I hold close for all lifetimes to come.

To my extended family whose small part I am; proudly calling ourselves the Nadkarnis' of Kalatri.

ACKNOWLEDGMENTS

Foremost, I would like to thank my committee Chair and advisor, Dr. Dallas N. Little. He has been an inspiration and has always tried to teach me the virtues of trying to reach excellence through the details. He has been an inspiration in terms of his teaching and research, both. Moreover, without his patience and understanding with my work, along with continued financial support, none of this would have been possible.

I am grateful to the Co-Chair of my committee, Dr. David H. Allen. He has been the guiding hand for me in the world of numbers and computations, to the extent that he has been able to alter aspects of my perspective.

I thank Dr. Robert L. Lytton for being a part of my advisory committee and giving helpful insights and suggestions. I am grateful to Dr. Anastasia Muliana for accepting to be a part of my committee. I owe immense gratitude to Dr. Masoud K. Darabi for his guidance. Thank you, Dr. Navneet Garg for the guidance as well as financial support. Thank you, Dr. John F. Rushing for you valuable support. I owe gratitude to all the above committee members for reading this dissertation and responding with valuable insights and comments.

I would like to thank my colleagues from Texas A&M University for their encouragement and support: Dr. Lorena Garcia Cucalon, Dr. Narain Hariharan, Dr. Pavan Akula, Dr. Javier Saavedra, and Dr. Eisa Rahmani. I thank my colleagues from University of Kansas: Dr. Rashmi Kola and Dr. Mohammad Bazzaz.

Finally, I thank all my seniors and colleagues from the Texas A&M University laboratories: Mr. Rick Canatella, Mr. Lee Gustavus, Mr. Ross Taylor, and Mr. Ethan Karnei.

CONTRIBUTORS AND FUNDING SOURCES

Contributors

This work was supported by dissertation committee consisting of Professor Dr. Dallas N. Little (advisor), Dr. David H. Allen (co-advisor), Dr. Robert L. Lytton, and Dr. Anastasia Muliana.

Financial support was provided by Dr. Navneet Garg through the Federal Aviation Administration grants for Texas A&M university and University of Kansas (through Dr. Masoud K. Darabi). Dr. John F. Rushing supported by lending laboratory materials.

All other work conducted for the dissertation was completed by the student independently.

Funding Sources

Graduate study was supported by a Research Assistantship from Dr. Dallas N. Little through the Texas A&M University.

NOMENCLATURE

PANDA	Pavement Analysis using Non-linear Damage Approach
2D	Two Dimensional
3D	Three Dimensional
HMA	Hot Mix Asphalt
WMA	Warm Mix Asphalt
FEM	Finite Element Method
I_1	First invariant of the total stress tensor
J_2	Second invariant of the deviatoric stress tensor
σ_{ij}	Components of total stress tensor
σ_{ys}	Yield stress
$d\epsilon_{ij}^{pl}$	Components of plastic strain tensor
n_{ij}	Components of deviatoric vector indicating direction of flow
β	Combined hardening factor
γ	Progressively evolving yield surface factor

TABLE OF CONTENTS

Page

LIST OF FIGURES

FIGURE Page

LIST OF TABLES

TABLE Page

1. INTRODUCTION AND DISSERTATION STRUCTURE

Rutting is a ubiquitous problem in asphalt concrete pavements. It is extremely pronounced at high temperatures in airfield pavements such as runways and taxiways. Mechanically, rutting is described as permanent deformation induced in pavement layers as a result of frequent passes of tire load, resulting in formation of longitudinal depression in the wheel track. Although numerous construction techniques are used to reduce the rutting problem [2], they do not suffice. Developing a numerical model to capture the rutting in base layer is a critical aspect of pavement design that needs comprehensive research.

1.1 Federal Aviation Administration (FAA) Approach to Rutting

In recent years, various advancements have been made in investigation of pavement response under high tire pressures and predicting rutting performance. Material properties, tire load, tire pressure, and temperature are some of the factors that affect rutting. For classifying tire pressure, a common technique used in airport pavement design is the pavement classification number (PCN) methodology. Recently, the International Civil Aviation Organization (ICAO) increased the tire pressure limits on pavements falling under the PCN methodology. In particular, the maximum tire pressure for Category X aircraft was increased from the previous limit of 218 psi to 254 psi.

The newer aircraft such as Boeing 787 and Airbus 350 have tire pressures higher than 220 psi. In hot mix asphalt (HMA) and warm mix asphalt (WMA) pavements, such high tire pressures result in localized and concentrated load effects. These in turn have pronounced effect on rutting. Thus the new generation of aircraft have created a new set of challenges in evaluating the rutting performance of airfield pavements, especially under higher pavement temperatures and tire pressures.

To understand the behavior of pavement under heavy tire pressures, the FAA in 2013 added an outdoor testing facility: National Airport Pavement and Materials Research Center (NAPMRC). This facility contains a state-of-the-art Heavy Vehicle Simulator, Airfields Mark VI (HVS-A).

NAPMRC is based at the FAA's Airport Technology Research and Development Branch at the William J. Hughes Technical Center (WJHTC) in Atlantic City, New Jersey.

The NAPMRC facility was primarily established for understanding the behavior of surface asphalt layer. Consequently tire pressure, wheel load, and pavement temperature are deemed to be the primary input parameters in the experimental design as compared to landing gear load, which is typically deemed to be more critical to understanding the behavior of lower, granular layers of the pavement structure.

1.2 PANDA Approach to Rutting

Previously, a finite element (FE) based computer program on materials constitutive relationship [3] known as Pavement Analysis Using Non-linear Damage Approach (PANDA) was developed to predict the response of asphalt concrete pavements subjected to varied traffic loading and environmental conditions. The program, which is among the very comprehensive and sophisticated mechanistic-based constitutive relationships available in literature, is also being continually improved with additions and refinements. It incorporates Schapery's viscoelastic [4], Perzyna-type viscoplasticity [5] with extended Drucker-Prager yield surface, hardening-relaxation viscoplastic [6], viscodamage [7], moisture-induced damage [8], and oxidative aging ([9] and [10]) constitutive relationships that can be used to model the performance of airfield and roadway pavements subjected to high tire pressures and environmental factors ([11] and [12]).

1.3 Problem Statement

Studies by FAA indicate that rutting is associated with the base layer of airport HMA pavements ([13],[14],and [15]). Analysis of rutting distress occurring in pavement base layers composed of granular materials is based on plasticity theory. In this, the stress-strain curve has an elastic and a plastic portion, separated by a yield point. Many plasticity models, such as the elasto-plastic rate-independent ones, are available in literature to characterize the rutting distress. These usually have the three most common hardening rules: isotropic hardening rule; kinematic hardening rule; and a combination of the two, the so-called combined hardening rule. The isotropic

Drucker-Prager model does not capture the evolution of yield surface beyond the first few load cycles that simulate frequent passes of aircraft tires. In case of many granular materials, it has been observed that actual reyielding takes place at stress levels in between those predicted by isotropic and kinematic hardening mechanisms. Thus, a single combined hardening model is proposed to be evaluated. The model has a progressively reducing yield surface with the introduction of a new parameter, which allows the yield surface to progressively evolve even in the case of cyclic loading.

1.4 Organization of Dissertation

This dissertation describes and evaluates a combined hardening Drucker-Prager model with a progressively evolving yield surface for granular materials. Chapter I introduces the topic of rutting and efforts to solve the problem as handled by airport pavement community. Chapter II reviews literature on rutting in general with a focus on plasticity theory as applicable to granular materials. Chapter III fully describes the material model created along with the numerical and computational development. Chapter IV documents the full-scale experiment conducted at FAA's NAPMRC facility, the laboratory studies conducted to identify material properties, and studies conducted to qualify the numerical simulation cycles and load times. Chapter V highlights the validation of the structural model. Finally, Chapter VI summarizes the research and presents the conclusions.

The numerical material model is presented in APPENDIX A.

2. LITERATURE REVIEW

This chapter describes the rutting problem in HMA and WMA paved airport runway and taxiway flexible pavements as documented in existing literature with a focus on the unbound granular layers. The typical unbound granular layers in an HMA or WMA airport pavement are base and subbase. It is to be noted that the particular focus of this dissertation and work is the base layer. While the phrase "HMA layer" signifies the asphalt layer, the phrase "HMA pavement" signifies a generic reference to an asphalt concrete flexible pavement system. Relevant mechanical models on base layer are also documented. The literature has been reviewed with an aim to develop a case for implementing a more sophisticated and mechanics-based pressure-dependent plasticity constitutive model for analyzing the base layer.

2.1 The Rutting Problem in Pavements

Rutting is a critical distress in HMA and WMA pavements, particularly affecting the base layer. Previously, some experiments have been performed by the FAA to quantify layer-wise distribution of the total rutting on a flexible pavement. The results indicated that granular layers contribute to most of the rutting ([13],[14],and [15]). Application of tire heavy load/pressure results in formation of depression in the wheel path. In a pavement cut section, this depression appears as a downward vertical deformation termed rutting.

A number of permanent deformation models for granular layers have been documented in the literature. A log-normal relation between the permanent strain and number of loading cycles has been proposed [16]. A log-log relationship between the permanent strain and number of load applications instead of the log normal approach has also been suggested ([17] and [18]).

2.2 Role of Plasticity in Permanent Deformation

Traditionally, the failure of granular material has been based upon plasticity theory. In accordance with the plasticity theory, the stress-strain curve has an elastic and a plastic part, separated by a yield point. The theory assumes that the elastic part of the stress-strain curve results in com-

pletely recoverable elastic deformations.

When loading continues immediately beyond the elastic region, a point (or a stress state) is reached beyond which the variation of stress with strain is no longer linear. This is called the yield point and the stress corresponding to the yield point is called the yield stress. Such a loading results in plastic strains which are permanent in nature and thus, non-recoverable.

This literature review documents some of the failure criteria that have been traditionally used in characterizing the plasticity of granular materials and metals. The criteria that were developed for metals have been listed for documentation and general comprehension. The Coulomb-Mohr and Drucker-Prager criteria have been documented as applicable to materials such as roadway bases, subbases, and even pharmaceutical tablets.

2.2.1 Background

The mechanical behavior described as plasticity generally involves yielding, flow, and hardening. The parameters such as yielding and hardening may involve unique modifications to the existing models and are described below generally.

- **Yielding** is signified by the yield surface in the stress space which defines the boundary between elastic and plastic regions of deformations. In order to determine the onset of plastic deformation in a material, we assume a basic parameter known as the yield criterion. If the stress state at a point satisfies the yield criterion, the point deforms plastically. If not, there exists only elastic, recoverable deformation at that point. All deformations within the yield surface are perfectly recoverable.

- **Flow** defines the evolution of strain with loading. In general, if the strain increment direction is perpendicular to the yield surface at any given point on the yield surface, the flow is associated. Otherwise, the flow is non-associated. Non-associated flow involves the concept of plastic potential. In such a case, the plastic strain increment is directly proportional to the gradient of plastic potential, which is not perpendicular to the yield surface.

- **Hardening** parameter defines the evolution of the yield surface through the process of plastic

deformation. For example, if with the incrementation of stress beyond yield point the yield surface expands equally and uniformly in all directions, the phenomenon is designated as isotropic hardening. It is to be noted that an equal and uniform contraction of the yield surface can also result, which typically happens in granular materials. This phenomenon is called softening, and its nature is isotropic. In some cases, the yield surface beyond certain stress increment value translates without any rotation. This phenomenon is called kinematic hardening.

- **Special types of hardening** as in isotropic, anisotropic, and kinematic hardening can occur in various combinations. For example, isotropic hardening may be followed by kinematic hardening as much as anisotropic hardening by kinematic hardening.

2.2.2 Mises Criterion

This criterion, attributed mainly to von Mises [19] and Huber [20], assumes that yielding occurs when the second invariant of the deviatoric stress tensor J_2 reaches a critical value. It should be noted that because the dependence is not on I_1, which is the first invariant of the stress (total) tensor, the yield surface remains parallel to the hydrostatic axis. Hence, in the three dimensional stress space, the von Mises criterion results in a yield surface that resembles the surface of a cylinder, the axis of which is the hydrostatic axis.

This criterion represents an ellipse in the two dimensional stress space. In general, von Mises criterion is given by: $J_2 - k^2 = 0$ for yielding or plastic deformation and $J_2 < k^2$ for elastic deformation. Here, k is a material property.

2.2.3 Tresca Criterion

This criterion [21] assumes that yielding occurs when the maximum shear stress reaches a critical value *k* of the material. As in the von Mises criterion, because the dependence is not on I_1, the yield surface remains parallel to the hydrostatic axis. In the three dimensional stress space, the Tresca criterion results in a yield surface that resembles the surface of a hexagonal prism, the axis of which is the hydrostatic axis. This criterion represents a hexagon in the two dimensional stress

space.

In general, Tresca criterion is given by: $T_{max} = k$ for yielding or plastic deformation and $T_{max} < k$ for elastic deformation. Here, as in the von Mises criterion, *k* is a material property. In case of materials that are pressure sensitive, the yield criteria is dependent upon I_1, the first invariant of the stress tensor. Materials that qualify in this category are granular and porous in nature.

2.2.4 Coulomb-Mohr Criterion

This criterion [22] assumes that the critical yielding stress depends not only on the maximum shear stress but also on the normal stress. This assumption implies a dependence on hydrostatic stress (and also, I_1). The yield surface does not remain parallel to the hydrostatic axis. In the three dimensional stress space, the yield surface resembles a hexagonal cone. The locus of this cone on any deviatoric plane is an irregular hexagon and its axis is parallel to the hydrostatic axis.

2.2.5 Drucker-Prager Criterion

The von Mises criterion, as mentioned above, assumes that yielding occurs when J_2 reaches a critical value. Daniel Drucker and William Prager proposed and established a variation [23] of this criterion by adding a scalar multiplier of I_1, thereby rendering the yield criterion dependent upon hydrostatic stress. Hence, in the three dimensional stress space, this so-called Drucker-Prager criterion results in a yield surface that resembles a right circular cone. The axis of this cone is parallel to the hydrostatic axis, while the cross section on any deviatoric plane is a circle. This criterion is generally represented as follows:

$$f = \sqrt{J_2} + \alpha I_1 - k \tag{2.1}$$

Here, α and k are material constants related to friction angle and cohesion, respectively.

The Drucker-Prager Cap (DPC) model ([24] & [25])for isotropic material adds two features to the standard model:

1. The cap surface, which represents the material densification beyond yield point. Beyond

yield point, the material hardens due to cold working principle, and the model is then bound by an elliptical surface.

2. The transition surface. This is essential in order to ensure a smooth transition between the Drucker-Prager yield surface and the CAP surface, because abruptness and corners in the yield surfaces presents computational hardships and inaccuracies.

In general, an extension of the Drucker-Prager model involves:

1. Curved yield surfaces in the meridional plane.

2. Circular yield surfaces on the deviatoric stress plane (or the octahedral plane).

3. Nonassociated flow laws.

2.2.6 Yield Criteria in Pavement Engineering (Granular Materials)

The effect of increasing axle loads and tire pressure on pavement deterioration using three dimensional (3D) finite element method (FEM) simulations [26] was studied at Canterbury Accelerated Pavement Testing Indoor Facility in New Zealand. Strains, interface stresses, and deflections were measured. Evaluations were conducted at the pavement base and subbase layers. The FEM results were compared to results from two elastic layered analysis programs: ELSYM5 and CIRCLY. While ELSYM5 assumes isotropy, CIRCLY accounts for material anisotropy. The FEM analysis used the Drucker-Prager model with isotropic hardening and associated flow.

The results for the base layers analysis indicated a general agreement between the measured strains and the ones calculated using the two elastic programs. The FEM model predicted higher strains. The authors' assertion was that all three methods effectively estimated the base layer strains because the base layer behaves elastically under the simulated tire loads.

The results for the subbase layer indicated CIRCLY results to match the measured strains better than ELSYM5. Furthermore, FEM results indicated the best match to the measured strains. The authors concluded that CIRCLY was a better estimator of the strains in comparison to ELSYM5

because in spite of both being elastic programs, CIRCLY had the ability to address anisotropy. Additionally, the fact that the FEM results matched the measured strains more closely was attributed to the subgrade being plastic in nature, resulting in FEM being a better simulator of plasticity as modeled using the Drucker-Prager model.

Another study [27] used a dynamic vehicle model to estimate the dynamic wheel force, and also a 3D FEM nonlinear dynamic pavement model to determine the response. The aim of the study was to analyze the effect of pavement roughness on vehicle bounce, and also to investigate the effect of vehicle bounce on pavement roughness progression. The authors used the elastic-plastic Drucker-Prager model to characterize the base as well as the subbase of the pavement structure.

Incorporation of base and subbase rutting in pavement design [28], which was until then generally assumed to be insignificant was done by applying the flow theory of plasticity. This required a yield surface and material parameters from results of laboratory triaxial testing.

An hierarchical single surface (HISS) modeling approach [29] was introduced in which yield surface and flow were used without investigating the elastic response because the authors were only interested in the amount of permanent deformation that was associated with a given stress state. Hence, the complete stress-strain behavior of the granular materials investigated was not defined.

Using the postulate that pavement loading can be simulated in the laboratory triaxial tests using principal stress pulses that are mostly haversine [16], the authors stipulated that for base, subbase, and subgrade, principal stress pulses after small initial hydrostatic consolidation are appropriate because these upper layers have very low consolidations pressures. The basic hierarchical model was used, that consisted of series of yield surfaces that expand with increasing plastic strains. The surfaces are plotted on the $I_1 - \sqrt{J_2}$ stress space.

A method for evaluation of both the resilient elastic and residual plastic properties from repeated load testing has also been recommended [30]. The author described the residual properties of the material using three parameters: *(a)* the slope of the permanent strain versus number of load repetitions on log-log scale, *(b)* the loading stress-strain curve of the first cycle, and *(c)* the resilient

properties of the material. The analysis was based on theory of elastoplasticity and the following models were outlined:

1. Vermeer ([31] & [32])

2. HISS (hierarchical single surface)

The Vermeer model uses the Mohr-Coulomb law wherein the shear and volumetric flow surfaces are independent and their intersection results in "corners," creating a computational problem in numerical analysis. The model involves four parameters and was primarily developed for cohesionless materials. The HISS model uses the Drucker-Prager theory and consists of a single surface; requiring parameters to describe the failure law as well as the evolution of the plastic deformation. Both models were recommended for the residual properties.

A method which allows implicit stress integration of the Drucker-Prager model with kinematic hardening [33] for granular materials subjected to cyclic loading has also been described. Stress integration is the computation of the incremental stress changes corresponding to incremental strain change at each step during FEM modelling process, and the study tries to implement the algorithm so that it simulates the Drucker-Prager material with kinematic hardening. The author computes the scalar plastic parameter from the yield surface and plastic potential functions, from which the stress increment is calculated. From this, and the total strain increment, the elastic-plastic constitutive matrix is calculated. Finally, using the concept of back stress and Drucker linear kinematic hardening theory, the stress integration is achieved. The kinematic hardening definition used is the one which calculates the back stress with respect to dynamic relaxation; which is the theory of Armstrong-Frederick kinematic hardening.

3. DESCRIPTION OF MODELS

3.1 Introduction

In this study, a new modified Drucker-Prager combined hardening model for incorporating cyclic hardening in the base layer is postulated. The constitutive model captures rutting in the granular layers by the means of evolution of plastic strain components. This chapter presents the relevant equations in the derivation of the model. Furthermore, wherever required, the asphalt concrete has been modeled using the constitutive package PANDA [3] as mentioned earlier. The basic and relevant tenets of the model have also been described. To summarize, this chapter describes:

1. A new postulated variation of the Drucker-Prager combined hardening model as applicable to granular materials.

2. Relevant aspects of the PANDA constitutive package.

3.2 Modified Combined Hardening Drucker-Prager Model

A new modified Drucker-Prager combined hardening model for incorporating cyclic hardening in the base layer is postulated and described in this section. The constitutive model is based on the classical Drucker-Prager [23] model, vastly described in literature and used in an almost ubiquitous manner in the area of constitutive modeling of plastic and viscoplastic materials. The modifications to the models as applicable to granular media is conducted on the basis of a previous model developed for ABAQUS [34]. We commence through linear elasticity.

3.2.1 Elasticity

The strain tensor is first decoupled into elastic and plastic parts:

$$\epsilon_{ij} = \epsilon_{ij}^{el} + \epsilon_{ij}^{pl} \tag{3.1}$$

where ϵ_{ij}^{el} and ϵ_{ij}^{pl} are the elastic and plastic parts of the strain tensor, respectively. The strain formulation for a simple linear elastic isotropic material is written as:

$$\sigma_{ij} = 2G\epsilon_{ij}^{el} + K\epsilon_{kk}^{el}\delta_{ij} \tag{3.2}$$

where σ_{ij} is the stress tensor; G is the shear modulus; K is the bulk modulus; and δ_{ij} is the Kronecker delta, which is a second-order identity (unit) tensor. In the incremental form, the stress tensor, σ_{ij}, is expressed as:

$$\sigma_{ij}|_{n+1} = \sigma_{ij}|_{n} + \Delta\sigma_{ij} \tag{3.3}$$

where $\sigma_{ij}|_{n+1}$ is the updated stress at time, $t|_{n+1}$ which occurs after a time interval (increment) of Δt since time, $t|_n$; $\sigma_{ij}|_n$ is the updated stress at time, $t|_n$; and $\Delta\sigma_{ij}$ is the total stress increment. However, σ_{ij} is also expressed as follows:

$$\sigma_{ij} = D_{ijlk}\epsilon_{kl} \tag{3.4}$$

where D_{ijlk} is the fourth order elasticity tensor. Using Equation 3.4 in Equation 3.3, the incremental form is rewritten as:

$$\sigma_{ij}|_{n+1} = \sigma_{ij}|_{n} + D_{ijlk}\Delta\epsilon_{kl} \tag{3.5}$$

Decoupling the hydrostatic and deviatoric parts of Equation 3.5, we write:

$$\sigma_{ij}|_{n+1} = \sigma_{ij}|_{n} + [2G\delta_{ik}\delta_{jl} + \lambda\delta_{ij}\delta_{kl}]\Delta\epsilon_{kl} \tag{3.6}$$

where λ is the Lame's constant. Solving the indicial notations in Equation 3.6 results in:

$$\sigma_{ij}|_{n+1} = \sigma_{ij}|_{n} + 2G\Delta\epsilon_{ij} + \lambda\Delta\epsilon_{kk}\delta_{ij} \tag{3.7}$$

The increment in the total strain tensor, $\Delta\epsilon_{ij}$, in Equation 3.7 above can be decoupled into deviatoric and hydrostatic parts as:

$$\Delta\epsilon_{ij} = \Delta e_{ij} + \frac{1}{3}\Delta\epsilon_{kk}\delta_{ij} \tag{3.8}$$

where e_{ij} is the deviatoric part of the total strain tensor. Using Equation 3.8 in Equation 3.7; the relation between λ and K; and manipulating the terms for convenience, we get:

$$\sigma_{ij}|_{n+1} = \sigma_{ij}|_n + 2G\Delta e_{ij} + K\Delta\epsilon_{kk}\delta_{ij} \tag{3.9}$$

3.2.2 Yield Function

The Drucker-Prager yield function, Equation 2.1, which has already been defined earlier, is restated in this section in a format that is convenient for granular materials and is expressed in terms of σ_{eff}, the effective stress. Firstly, the effective stress is defined as:

$$\sigma_{eff} = \sqrt{3J_2} \tag{3.10}$$

The Drucker-Prager yield criterion, which is a function of I_1 and J_2, is expressed as:

$$f(I_1, J_2) = \sqrt{3J_2} + aI_1 - \sigma_{ys} \tag{3.11}$$

where a is a material parameter related to cohesion; and σ_{ys} is the yield strength of the material under uniaxial loading conditions. Using Equation 3.10 in Equation 3.11 and dropping the parentheses connected with f for convenience, we express the yield function as:

$$f = \sigma_{eff} + aI_1 - \sigma_{ys} \tag{3.12}$$

We compare the above yield function to the ABAQUS yield function as:

$$f = t - p\tan\theta - d \tag{3.13}$$

where t is the effective stress which is given as:

$$t = \frac{\sigma_{eff}}{2}[1 + \frac{1}{K} - (1 - \frac{1}{K})(\frac{r}{\sigma_{eff}})^3] \tag{3.14}$$

where p is the hydrostatic pressure; θ is the slope of the yield surface in the $p-t$ stress plane for the linear Drucker-Prager model, or the friction angle of the material in the meridional stress plane; d is the yield stress, σ_{ys}; and K is a material parameter related to the convexity of the yield surface in the deviatoric plane. The yield stress is as function of equivalent plastic strain, ϵ_{eq}^{pl}, which is expressed as:

$$\epsilon_{eq}^{pl} = \sqrt{\frac{2}{3}\epsilon_{ij}^{pl}\epsilon_{ij}^{pl}} \tag{3.15}$$

In Equation 3.14, if $K = 1$, the yield surface in the deviatoric plane becomes circular. Accordingly, this study assumes the yield surface to be circular in the deviatoric plane. Implicit with this assumption is that the overall shape of the Drucker-Prager yield surface is right-circular cone. Furthermore, Equation 3.14 is now rewritten as:

$$t = \sigma_{eff} \tag{3.16}$$

The Figure 3.1 shows the graphical formation of the linear Drucker-Prager model.

The formulation developed in this study for granular materials is assuming associated flow. In general, ψ is the dilation angle. The associated flow formulation is achieved by setting $\psi = \beta$.

In the compression regime the pressure, p, is defined as:

$$p = -\frac{1}{3}I_1 \tag{3.17}$$

Using Equation 3.16 and Equation 3.17 in Equation 3.13, we write:

$$f = \sigma_{eff} + \frac{1}{3}I_1 \tan\theta - \sigma_{ys} \tag{3.18}$$

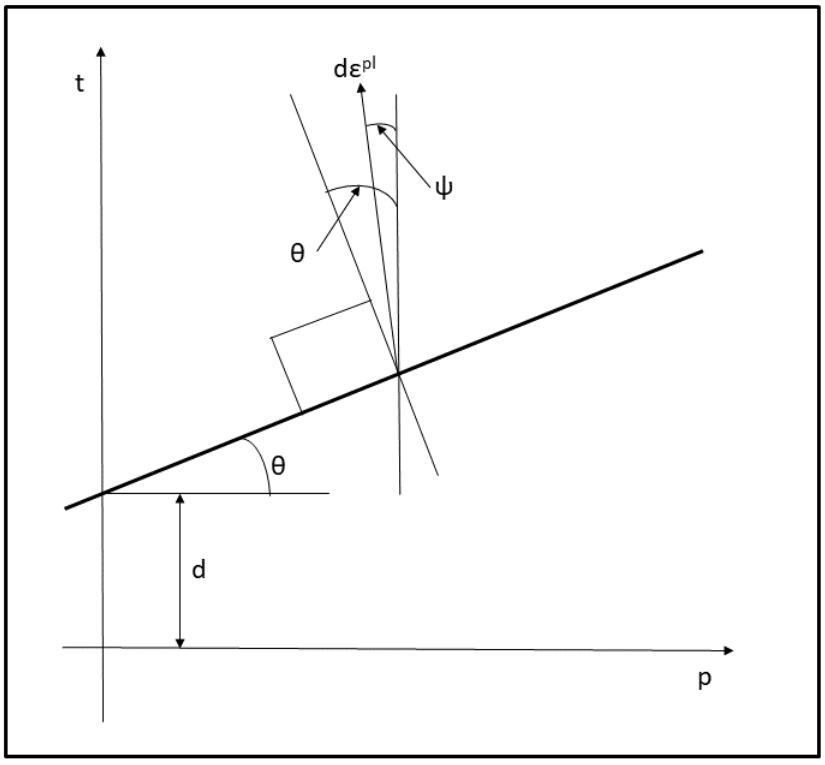

Figure 3.1: Linear Drucker-Prager Model in $p - t$ Plane

Comparing Equation 3.12 and Equation 3.18, we write:

$$a = \frac{1}{3} \tan \theta \tag{3.19}$$

Using Equation 3.17 and Equation 3.19 in Equation 3.18, we write:

$$f = \sigma_{eff} - 3ap - \sigma_{ys} \tag{3.20}$$

The form in Equation 3.20 is primarily used in the development of the modified Drucker-Prager formulation in this study.

3.2.3 Flow Rule

The flow rule for the associated plasticity model is:

$$d\epsilon_{ij}^{pl} = d\phi \frac{\partial f}{\partial \sigma_{ij}} \tag{3.21}$$

where the notation d associated with a physical quantity without any denominator indicates derivative of that quantity with respect to time. In this section, we derive the flow equation of the pressure dependent Drucker-Prager model. We recall that the stress tensor is expressed as:

$$\sigma_{ij} = s_{ij} + \frac{1}{3}\sigma_{kk}\delta_{ij} \tag{3.22}$$

where s_{ij} is the deviatoric stress tensor. The effective stress and hydrostatic pressure as defined as:

$$\sigma_{eff} = \sqrt{\frac{3}{2}s_{ij}s_{ij}} \tag{3.23}$$

and,

$$p = -\frac{\sigma_{kk}}{3} \tag{3.24}$$

Using Equation 3.23 and Equation 3.24 in Equation 3.20, we write:

$$f = \sqrt{\frac{3}{2}s_{ij}s_{ij}} - 3a(-\frac{\sigma_{kk}}{3}) - \sigma_{ys} \tag{3.25}$$

The gradient of the yield function, $\frac{\partial f}{\partial \sigma_{ij}}$, is evaluated by taking the partial derivative of Equation 3.25:

$$\frac{\partial f}{\partial \sigma_{ij}} = \frac{3}{2}\frac{s_{ij}}{\sigma_{eff}}\frac{\partial s_{ij}}{\partial \sigma_{kl}} + a\delta_{ij} \tag{3.26}$$

We denote deviatoric vector, n_{ij}, for convenience such that:

$$n_{ij} = \frac{3}{2}\frac{s_{ij}}{\sigma_{eff}} \tag{3.27}$$

Using Equation 3.26 and Equation 3.27 in Equation 3.21, we write:

$$d\epsilon_{ij}^{pl} = d\phi[n_{ij}\frac{\partial s_{ij}}{\partial \sigma_{kl}} + a\delta_{ij}] \tag{3.28}$$

Indicial notation and manipulations therewith, since both n_{ij} and s_{ij} are deviatoric vectors, result in the final form of Equation 3.28 being:

$$d\epsilon_{ij}^{pl} = d\phi[n_{ij} + a\delta_{ij}] \tag{3.29}$$

From Equation 3.20, following two equations can be derived:

$$\frac{\partial f}{\partial \sigma_{eff}} = 1 \tag{3.30}$$

and,

$$\frac{\partial f}{\partial p} = -3a \tag{3.31}$$

We conveniently insert Equation 3.30 into the deviatoric part and Equation 3.31 into the hydrostatic part of Equation 3.29, to obtain:

$$d\epsilon_{ij}^{pl} = [d\phi\frac{\partial f}{\partial \sigma_{eff}}]n_{ij} + \frac{1}{3}[-d\phi\frac{\partial f}{\partial p}]\delta_{ij} \tag{3.32}$$

The deviatoric portion of the plastic strain rate is designated as de_q^p and the volumetric portion of the plastic strain rate is designated as $d\epsilon_p^p$. The equations, accordingly, are:

$$de_q^p = d\phi\frac{\partial f}{\partial \sigma_{eff}} \tag{3.33}$$

and,

$$d\epsilon_p^p = -d\phi\frac{\partial f}{\partial p} \tag{3.34}$$

Using Equation 3.33 and Equation 3.34 in Equation 3.32, we write:

$$d\epsilon_{ij}^{pl} = de_q^p n_{ij} + \frac{1}{3} d\epsilon_p^p \delta_{ij} \tag{3.35}$$

3.2.4 Internal State Variables

The model consists of one internal state variable that is derived form the principle of plastic work done [34]. This state variable is the equivalent plastic strain, ϵ_{eq}^{pl}. This equation is stated below [34]:

$$d\epsilon_{eq}^{pl} = \frac{\sigma_{eff} de_q^p - p d\epsilon_p^p}{\sigma_{ys}} \tag{3.36}$$

The above Equation is written in its incremental form as:

$$\Delta\epsilon_{eq}^{pl} = \frac{\sigma_{eff} \Delta e_q^p - p \Delta\epsilon_p^p}{\sigma_{ys}} \tag{3.37}$$

3.2.5 Numerical Integration of the Model

The integration method used is the backward Euler method as described in the formulation by Allen [34]. In the numerical integration of plasticity model, we assume for each increment that the applied strain increment is elastic. Therefore, Equation 3.9, in accordance with the stated assumption, is rewritten below with all strain terms having superscript "el" indicating that the increment is elastic.

$$\sigma_{ij}|_{n+1} = \sigma_{ij}|_n + 2G\Delta e_{ij}^{el} + K\Delta\epsilon_{kk}^{el}\delta_{ij} \tag{3.38}$$

The above Equation 3.38 is decomposed such that the elastic strain components may be expressed by subtracting the plastic strain increment from the total strain increment. Hence, decomposed form of Equation 3.38 is:

$$\sigma_{ij}|_{n+1} = \sigma_{ij}|_n + 2G(\Delta e_{ij} - \Delta e_{ij}^{pl}) + K(\Delta\epsilon_{kk} - \Delta\epsilon_{kk}^{pl})\delta_{ij} \tag{3.39}$$

The incremental form of Equation 3.35 is:

$$\Delta\epsilon_{ij}^{pl} = \Delta e_q^p n_{ij} + \frac{1}{3}\Delta\epsilon_p^p \delta_{ij} \tag{3.40}$$

Comparing the plastic component terms in Equation 3.39 and Equation 3.40, we see that the deviatoric part analogous to Δe_{ij}^{pl} is:

$$\Delta e_{ij}^{pl} \sim \Delta e_q^p n_{ij} \tag{3.41}$$

and the hydrostatic part analogous to $\Delta\epsilon_{kk}^{pl}$ is:

$$\Delta\epsilon_{kk}^{pl} \sim \Delta\epsilon_p^p \tag{3.42}$$

Using Equation 3.41 and Equation 3.42 and rewriting Equation 3.39:

$$\sigma_{ij}|_{n+1} = \sigma_{ij}|_n + 2G(\Delta e_{ij} - \Delta e_q^p \, n_{ij}|_{n+1}) + K(\Delta\epsilon_{kk} - \Delta\epsilon_p^p)\delta_{ij} \tag{3.43}$$

We write the full form of $\sigma_{ij}|_n$:

$$\sigma_{ij}|_n = 2G \, \epsilon_{ij}|_n + \lambda \, \epsilon_{kk}|_n \, \delta_{ij} \tag{3.44}$$

However, using Equation 3.8, which is in incremental form, we expand the strain term in Equation 3.44 along similar lines:

$$\sigma_{ij}|_n = 2G[e_{ij}|_n + \frac{1}{3} \, \epsilon_{kk}|_n \, \delta_{ij}] + \lambda \, \epsilon_{kk}|_n \, \delta_{ij} \tag{3.45}$$

and the final form of the above Equation is:

$$\sigma_{ij}|_n = 2G \, e_{ij}|_n + K \, \epsilon_{kk}|_n \, \delta_{ij} \tag{3.46}$$

Using Equation 3.46 in Equation 3.43, we get:

$$\sigma_{ij}|_{n+1} = 2G\ e_{ij}|_n + 2G(\Delta e_{ij} - \Delta e^p_q\ n_{ij}|_{n+1}) + K\ \epsilon_{kk}|_n\ \delta_{ij} + K(\Delta\epsilon_{kk} - \Delta\epsilon^p_p)\delta_{ij} \tag{3.47}$$

Rearranging the terms of Equation 3.47:

$$\sigma_{ij}|_{n+1} = 2G(\ e_{ij}|_n + \Delta e_{ij}) - 2G\Delta e^p_q\ n_{ij}|_{n+1} + K(\ \epsilon_{kk}|_n + \Delta\epsilon_{kk})\delta_{ij} - K\Delta\epsilon^p_p\delta_{ij} \tag{3.48}$$

Equation 3.48 is the final predictor-corrector form for development of integral equation for the modified Drucker-Prager formulation. Using Equation 3.24 in Equation 3.22 and writing for the end of $(n+1)^{th}$ time increment:

$$\sigma_{ij}|_{n+1} = \ s_{ij}|_{n+1} - \ p|_{n+1}\ \delta_{ij} \tag{3.49}$$

where, after comparing with Equation 3.48:

$$s_{ij}|_{n+1} = 2G(\ e_{ij}|_n + \Delta e_{ij}) - 2G\Delta e^p_q\ n_{ij}|_{n+1} \tag{3.50}$$

and,

$$-\ p|_{n+1}\ \delta_{ij} = K(\ \epsilon_{kk}|_n + \Delta\epsilon_{kk})\delta_{ij} - K\Delta\epsilon^p_p\delta_{ij} \tag{3.51}$$

In the predictor-corrector methods in numerical integration of plasticity models, the above Equation 3.50 and Equation 3.51 represent the predictor and corrector parts. The predictor part is, in general, the stress state assuming a completely elastic solution while the corrector part brings the stress tensor back to the yield surface. The predictor part of the equation is indicated with the superscript "pr". The predictors parts are:

$$s^{pr}_{ij} = 2G(\ e_{ij}|_n + \Delta e_{ij}) \tag{3.52}$$

and,

$$-p^{pr}\delta_{ij} = K(\epsilon_{kk}|_n + \Delta\epsilon_{kk})\delta_{ij} \tag{3.53}$$

Using Equation 3.52 in Equation 3.50 and Equation 3.53 in Equation 3.51, we get:

$$s_{ij}|_{n+1} = s_{ij}^{pr} - 2G\Delta e_q^p \, n_{ij}|_{n+1} \tag{3.54}$$

which is the deviatoric predictor equation, and,

$$-p|_{n+1}\,\delta_{ij} = -p^{pr}\delta_{ij} - K\Delta\epsilon_p^p\delta_{ij} \tag{3.55}$$

Using Equation 3.54 and Equation 3.55 and rewriting Equation 3.49:

$$\sigma_{ij}|_{n+1} = s_{ij}^{pr} - 2G\Delta e_q^p \, n_{ij}|_{n+1} - p^{pr}\delta_{ij} - K\Delta\epsilon_p^p\delta_{ij} \tag{3.56}$$

We then and the deviatoric and pressure predictors to give the total predicted stress as:

$$\sigma_{ij}^{pr} = s_{ij}^{pr} - p^{pr}\delta_{ij} \tag{3.57}$$

Using Equation 3.57 in Equation 3.56, we get:

$$\sigma_{ij}|_{n+1} = \sigma_{ij}^{pr} - 2G\Delta e_q^p \, n_{ij}|_{n+1} - K\Delta\epsilon_p^p\delta_{ij} \tag{3.58}$$

Eliminating δ_{ij} from Equation 3.55, we get the pressure predictor equation as:

$$-p|_{n+1} = -p^{pr} - K\Delta\epsilon_p^p \tag{3.59}$$

From indicial notations manipulations, we know:

$$\sigma_{ij}n_{ij} = \sigma_{eff} \tag{3.60}$$

and,

$$n_{ij}n_{ij} = \frac{3}{2} \tag{3.61}$$

Projecting Equation 3.58 on to vector n_{ij}, we get:

$$\sigma_{eff}|_{n+1} = \sigma_{eff}^{pr} - 3G\Delta e_q^p \tag{3.62}$$

From Equation 3.27, we cal also write:

$$n_{ij}|_{n+1} = \frac{3}{2}\frac{s_{ij}|_{n+1}}{\sigma_{eff}|_{n+1}} \tag{3.63}$$

Using Equation 3.63 in Equation 3.54, we get:

$$s_{ij}|_{n+1} = \frac{s_{ij}^{pr}}{1 + \frac{3G\Delta e_q^p}{\sigma_{eff}|_{n+1}}} \tag{3.64}$$

Combining and rearranging the terms in Equation 3.62, Equation 3.63, and Equation 3.64, we write:

$$n_{ij}|_{n+1} = \frac{3}{2}\frac{s_{ij}^{pr}}{\sigma_{eff}^{pr}} \tag{3.65}$$

The right-hand-side (RHS) of Equation 3.65 is the predictor for vector n_{ij} and may be written as n_{ij}^{pr}. Accordingly, Equation 3.65 is rewritten as:

$$n_{ij}|_{n+1} = n_{ij}^{pr} \tag{3.66}$$

Rearranging and manipulating for convenience the terms of Equations 3.20, 3.30, 3.31, 3.33, and 3.34, we write:

$$de_q^p(-3a) + d\epsilon_p^p = 0 \tag{3.67}$$

and in the incremental form, Equation 3.67 is expressed as:

$$\Delta e_q^p(-3a) + \Delta \epsilon_p^p = 0 \tag{3.68}$$

Thus, the numerical integration scheme generates five non-linear equations that are solved using the Newton-Raphson method. These are Equations 3.20, 3.37, 3.59, 3.62, and 3.68 and they are re-stated below:

$$f = \sigma_{eff} - 3ap - \sigma_{ys} \tag{3.69}$$

$$\Delta \epsilon_{eq}^{pl} = \frac{\sigma_{eff} \Delta e_q^p - p \Delta \epsilon_p^p}{\sigma_{ys}} \tag{3.70}$$

$$-p|_{n+1} = -p^{pr} - K \Delta \epsilon_p^p \tag{3.71}$$

$$\sigma_{eff}|_{n+1} = \sigma_{eff}^{pr} - 3G \Delta e_q^p \tag{3.72}$$

$$\Delta e_q^p(-3a) + \Delta \epsilon_p^p = 0 \tag{3.73}$$

The equations above are solved using the general guidance provided in ABAQUS [35] and in the Allen model [34]. The below paragraphs highlight briefly the solution.

$$\frac{f(x_n)}{x_n - x_{n+1}} = slope = f'(x_n) \tag{3.74}$$

where x_n is the value of variable x at the n^{th} trial. We desire the value of x when the function, $f(x)$ vanishes (is zero). If a term, c_x, is introduced such that $x_n + c_x = x_{n+1}$, we see that c_x is the correction applied to the existing value x_n to get the next value, x_{n+1}. Hence:

$$x_n + c_x = x_{n+1} \tag{3.75}$$

Combining Equations 3.74 and 3.75:

$$f'(x_n) c_x = -f(x_n) \tag{3.76}$$

Here, $f'(x)$ is the Jacobian matrix for solving Equations 3.69 and 3.73 for obtaining the primary unknowns. The two primary unknowns, or the variables representing x are $\Delta\epsilon_p^p$ and Δe_q^p. Upon obtaining their values, Equations 3.70, 3.71, and 3.72 are solved by substitution so as to obtain other three unknowns. Finally, the equations, dropping the time interval subscripts for convenience, for the five unknowns are [34]:

$$\Delta\epsilon_p^p = \frac{a[\sigma_{eff}^{pr} - \sigma_{ys} - 3ap^{pr}]}{3Ka^2 + G} \tag{3.77}$$

$$\Delta e_q^p = \frac{\sigma_{eff}^{pr} - \sigma_{ys} - 3ap^{pr}}{9Ka^2 + 3G} \tag{3.78}$$

$$p = \frac{p^{pr}G + Ka\sigma_{eff}^{pr} - Ka\sigma_{ys}}{3Ka^2 + G} \tag{3.79}$$

$$\sigma_{eff} = \frac{3aGp^{pr} + 3Ka^2\sigma_{eff}^{pr} + G\sigma_{ys}}{3Ka^2 + G} \tag{3.80}$$

$$\Delta\epsilon_{eq}^{pl} = \frac{\sigma_{eff}^{pr} - \sigma_{ys} - 3ap^{pr}}{9Ka^2 + 3G} \tag{3.81}$$

From this, the strain and stress increments are determined. The Jacobian used for this model is the one used in ABAQUS for implicit methods such as von Mises plasticity [34]. Finally, the formulation for pressure dependent Drucker-Prager model used has the following equation for the equivalent plastic strain:

$$\Delta\epsilon_{eq}^{pl} = \frac{\sigma_{eff}^{pr} - \sigma_{ys}|_{n+1} + \sigma_{eff}|_n - \sigma_{ys}|_n - 3ap^{pr}}{9Ka^2 + 3G} \tag{3.82}$$

3.3 Combined Hardening Model and Necessity of Modification

In this section, the Drucker-Prager combined hardening model is briefly described along with the need for modification of the existing scheme.

3.3.1 Combined Hardening

When an elasto-plastic model is subjected to reversals in cyclic loading, it is observed that neither isotropic, nor kinematic hardening accurately estimate the material behavior or stress-strain response. In such as case, two internal state variables are required to accurately describe the model. The combined hardening general equation for the Drucker-Prager pressure dependent material is stated as:

$$f = \sqrt{\frac{3}{2}(s_{ij} - \alpha 2'_{ij})(s_{ij} - \alpha 2'_{ij})} + a(\sigma_{kk} - \alpha 2_{kk}) - \sigma_{ys} \tag{3.83}$$

where, $\alpha 2_{ij}$ is a second order tensor valued function indicating the location of the yield surface center. The two internal state variables to describe the model as σ_{ys} and $\alpha 2_{ij}$. While σ_{ys} is the variable capturing the growth in the size of the yield surface in case of isotropic hardening, $\alpha 2_{ij}$ is the location of the center of the yield surface and captures the translation, or the kinematic hardening part. The typical working of a combined hardening model for a uniaxial system of loading can be found in various sources in the literature [1]. Figure 3.2 depicts a typical combined hardening model for a uniaxial test.

3.3.2 Necessity of Base Yielding

On the basis of simulations conducted in this study using existing isotropic Drucker-Prager elastoplastic model, and literature review, it is proposed to incorporate a combined hardening mechanism in the elasto-plastic DP model, instead of the current isotropic hardening mechanism. As discussed earlier, plasticity models, and especially elasto-plastic rate-independent models require: a) yield function, b) flow rule, c) hardening rule, and d) evolution laws for all internal state variables involved. The three most common hardening rules are: isotropic hardening, kinematic hardening, and a combination of the two, the so-called combined hardening rule. In the following section, a brief explanation is given for the problem of non-yielding granular base and the required solution, which is the motivation for this work.

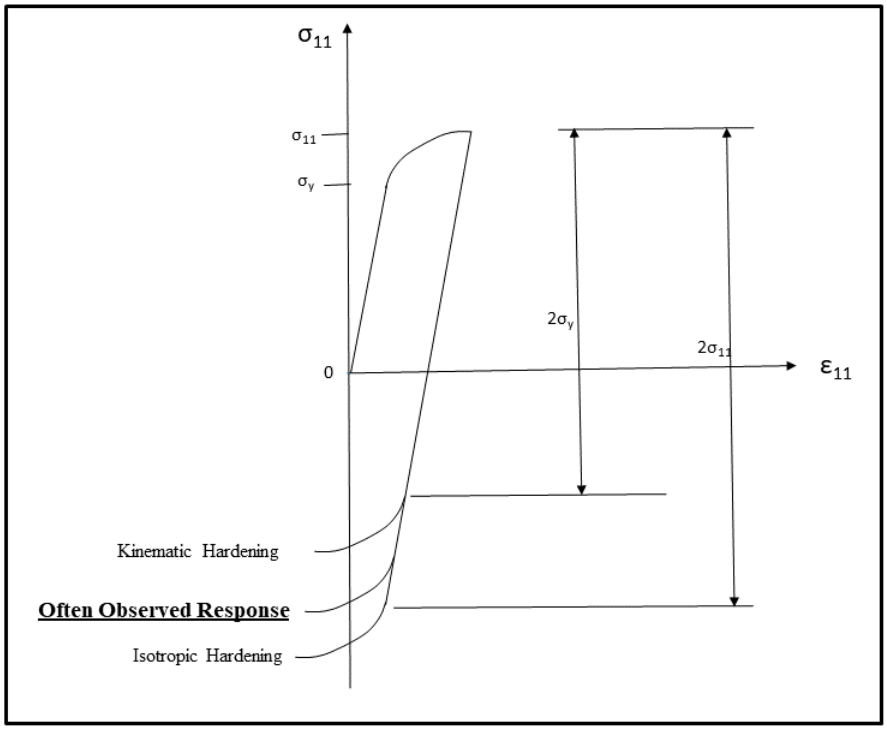

Figure 3.2: Uniaxial Test Comparison of Hardening Types

3.3.2.1 Reason for Modification

Isotropic hardening is characterized by a scalar valued variable that represents the size of the yield surface. In the stress space that represents plastic loading, the yield surface expands isotropically. This evolution of the yield surface, called hardening, is essential to capture the permanent deformation in the pavement. Permanent deformation occurs due to the irreversible plastic strain. However, in a given loading cycle, as the material is unloaded, the stress state falls back in the elastic region (inside the yield surface). Further plastic deformation is caused only if in the next loading cycle, the yield surface expands. For this to occur, the stress state in the next loading cycle should be outside the current yield surface. Translated for a uniaxial loading case, this implies that the value of stress component in the next loading cycle should be greater than the one in the

previous loading cycle.

For the three dimensional loading case in this research along with the loading pattern of NAPMRC, after the application of the first few load cycles of the last amplitude value, the stress state does not go beyond the yield surface. This results in plastic strains not evolving despite the application of further loading cycles. Isotropic hardening rule, thus, cannot capture the permanent deformations when the loading pattern is cyclic.

3.3.2.2 Applicability of Combined Hardening Rule

The permanent deformation data available from the NAPMRC testing indicates that the permanent deformation, and therefore the plastic strains, continue to evolve with each loading cycles. In literature, the mechanics of such a phenomenon can perhaps be captured if the yield surface is not allowed to expand but instead, made to translate. This form of hardening is known as kinematic hardening, which is characterized by a tensor valued function of stress which represents the translation of the yield surface. This results in yielding (or reyielding) at lower stress levels upon unloading or load reversals. This effect, knows as the Bauschinger effect [36], is required to be considered for the case of cyclic loading in order to capture the correct permanent deformation.

In case of many materials, it has been observed that actual reyielding in fact takes place at stress levels in between those predicted by isotropic and kinematic hardening mechanisms [37]. Thus, a single combined hardening model is proposed to be evaluated. This shall combine the internal state variables of both, isotropic and kinematic hardening mechanisms. The yield function for the combined hardening rule will now assume (and is a restatement of Equation 3.83) the form as follows [1] :

$$f = \sqrt{\frac{3}{2}(s_{ij} - \alpha 2'_{ij})(s_{ij} - \alpha 2'_{ij})} + a(\sigma_{kk} - \alpha 2_{kk}) - \sigma_{ys} \tag{3.84}$$

where, $\alpha 2_{ij}$ is a second order tensor valued function indicating the location of the yield surface center; and the primed component is its deviatoric part.

3.4 Development of the Constitutive Model

In this section, the constitutive model is validated using a single element in the ABAQUS analysis. Furthermore, the validation is accomplished using uniaxial loading system such that $\sigma_{22} \neq 0$, $\sigma_{ij} = 0$, *for all i,j*. It is noted that in the coordinate system chosen, the vertical direction is the $2-2$ direction. We restate Equation 3.29:

$$d\epsilon_{ij}^{pl} = d\phi[n_{ij} + a\delta_{ij}] \tag{3.85}$$

Squaring the above equation, we get:

$$d\epsilon_{ij}^{pl} d\epsilon_{ij}^{pl} = d\phi^2[n_{ij} + a\delta_{ij}][n_{ij} + a\delta_{ij}] \tag{3.86}$$

Multiplying by $\frac{2}{3}$, taking the square root, using Equation 3.61, and noting that $n_{ij}\delta_{ij} = n_{ii} = 0$, we get:

$$\sqrt{\frac{2}{3} d\epsilon_{ij}^{pl} d\epsilon_{ij}^{pl}} = d\phi\sqrt{1 + 2a^2} \tag{3.87}$$

Using Equation 3.15, we get:

$$d\epsilon_{eq}^{pl} = d\phi\sqrt{1 + 2a^2} \tag{3.88}$$

and finally:

$$d\phi = \frac{d\epsilon_{eq}^{pl}}{\sqrt{1 + 2a^2}} \tag{3.89}$$

We take $\bar{\sigma}$ as the Drucker-Prager effective stress. This is the total applied stress or the input stress in the single element or the structure being evaluated. It is expressed as:

$$\bar{\sigma} = \sigma_{eff} + aI_1 = \sigma_{eff} - 3ap \tag{3.90}$$

We observe, taking into account both Equations 3.12 and 3.20 that $\bar{\sigma}$ is basically that total effective stress which results in yielding if it is greater than the yield stress. We may rewrite both yield

forms as:

$$f = \bar{\sigma} - \sigma_{ys} \tag{3.91}$$

We express Equation 3.89 in a convenient manner by introducing $\bar{\sigma}$ in it such that:

$$d\phi = \frac{1}{\frac{d\bar{\sigma}}{d\epsilon_{eq}^{pl}}} \frac{d\bar{\sigma}}{\sqrt{1+2a^2}} \tag{3.92}$$

This form is convenient because the quantity, $\frac{d\bar{\sigma}}{d\epsilon_{eq}^{pl}}$, is the slope of the input yield curve, which we designate as H. One of the input material parameters of the Drucker-Prager model is the yield stress, σ_{ys}, versus equivalent plastic strain, ϵ_{eq}^{pl}, curve; and H is the slope of that curve at every increment. We rewrite Equation 3.92 as:

$$d\phi = \frac{1}{H} \frac{d\bar{\sigma}}{\sqrt{1+2a^2}} \tag{3.93}$$

The Prandtl-Reuss equation [38] in it simplified form applied to this model is as follows. We start with decoupling the strain tensor into its elastic and plastic parts, using Equation 3.1:

$$d\epsilon_{ij} = d\epsilon_{ij}^{el} + d\epsilon_{ij}^{pl} \tag{3.94}$$

The elastic part is further expanded as:

$$d\epsilon_{ij}^{el} = \frac{1+\nu}{E} d\sigma_{ij} - \frac{\nu}{E} d\sigma_{kk}\delta_{ij} \tag{3.95}$$

where E and ν are Young's modulus and Poisson's ratio, respectively; and the plastic part is expanded in accordance with Equation 3.85 as:

$$d\epsilon_{ij}^{pl} = d\phi[n_{ij} + a\delta_{ij}] \tag{3.96}$$

Using Equations 3.95 and 3.96 in 3.94, we write:

$$d\epsilon_{ij} = \frac{1+\nu}{E} d\sigma_{ij} - \frac{\nu}{E} d\sigma_{kk}\delta_{ij} + d\phi[n_{ij} + a\delta_{ij}] \tag{3.97}$$

For the uniaxial case:

$$d\epsilon_{22} = \frac{1+\nu}{E} d\sigma_{22} - \frac{\nu}{E} d\sigma_{22}\delta_{22} + d\phi[n_{22} + a\delta_{22}] \tag{3.98}$$

It is noted that in uniaxial loading of the type $\sigma_{22} \neq 0$, $\sigma_{ij} = 0$, *for all i,j*, we can write $\sigma_{kk} = \sigma_{22}$. Also, in the compressive loading regime, the sign of the load in compression is taken as negative(-). Finally, under uniaxial compressive loading conditions, the Drucker-Prager applied stress, $\bar{\sigma}$, shall be negative. We summarize the exact values of all quantities for uniaxial compressive case as:

$$\sigma_{22} = -\bar{\sigma} \tag{3.99}$$

$$\delta_{22} = 1 \tag{3.100}$$

and,

$$n_{22} = -1 \tag{3.101}$$

so that the final Prandtl-Reuss formation for the case under consideration is:

$$d\epsilon_{22} = -\frac{d\bar{\sigma}}{E} + d\phi[-1 + a] \tag{3.102}$$

3.4.1 Finite Element Model

The model mesh consists of a 3D cube of dimensions 1.00 mm for the side. The 2D FE mesh is shown in Figure 3.3. The direction "X" indicated in the Figure 3.3 was named the positive 1-1 direction. Hence, the components of stress (S11), strain (E11), and displacement (U1) in this direction are named accordingly in the ABAQUS analysis output and results. Similarly, the "Y"

direction was named positive 2-2. Hence, the direction positive 3-3 direction is the one perpendicular to the plane of the paper. The three boundary conditions imposed on the model were as follows. First, the front vertical face in the X-Y plane was constrained (fixed) against movement in the 3-3 direction; second, the left vertical face in the Y-Z plane was constrained against movement in the 1-1 direction; and third, the bottom horizontal face in the X-Z plane was constrained against movement in the 2-2 direction.

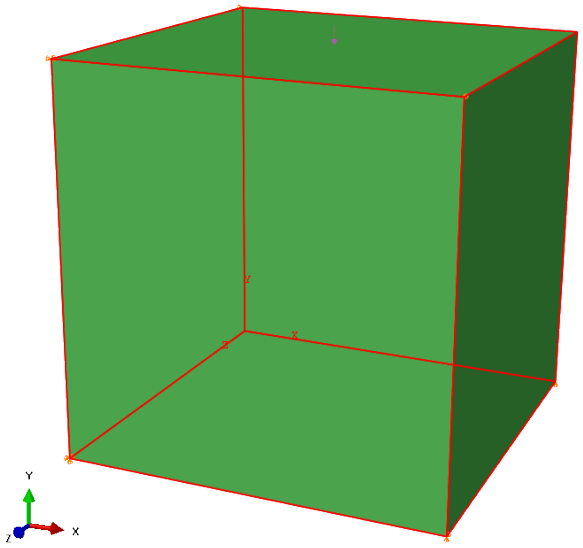

Figure 3.3: Three-Dimensional Finite Element Model

One element type was used in this analysis. The element type used was the ABAQUS continuum 8-node linear isoparametric element with reduced integration (C3D8R). An element aspect ratio of 1.0 was used.

3.4.2 Material Properties for Single Element

The model Young's modulus was 165.47 MPa, Poisson's ratio was 0.35, friction parameter, a was 0.2797, and combined hardening parameter, β was 1.000 (indicating isotropic hardening).

3.4.3 Input Yield Curve for Combined Hardening Model

The model needs a input yield curve of yield stress versus equivalent plastic strain in a uniaxial test. The input yield curve is given in Figure 3.4 [39]. It has been observed that the stress-strain curve of a cyclic test is, in general, lower in the X-Y axis plots as compared to the monotonic tests [39]. Cyclic tests, which represent in field the cyclic loading of systems such as the NAPMRC HVS-A, also represent realistic loading conditions on airport taxiways and runways. The input yield curve (stress-strain) curve is for granular material crushed limestone, Type 610 [39].

The aim of the proposed Drucker-Prager model is to include combined hardening, but ensuring that there is a progressive reduction in the yield surface size. This reduction is proposed as a function of equivalent plastic strain. A user material subroutine for ABAQUS finite element software, using constitutive package UMAT was modified for this study. This UMAT was based on previous similar works on Drucker-Prager and Mises models in ABAQUS.

The user material accepts a strain increment and calculates corresponding stress increment using the Newton-Raphson iterative process in line with the backward Euler method. At the start of the next increment calculations, all the components such as ϵ_{ij}^{el}, ϵ_{ij}^{pl}, $\alpha 2_{ij}$, ϵ_{eq}^{pl} are updated and also, the yield stress, σ_{ys} is updated. The equations are set up as follows. The usual formulation is described first. Subsequently, the modification to the model is described. We start with assigning a new variable, $\sigma_{ys}|_1$ to σ_{ys} in the usual formulation such that:

$$\sigma_{ys}|_1 = \sigma_{ys} \tag{3.103}$$

The next strain increment requires the previous yield surface, which in the isotropic hardening case is simply the updated yield surface (requiring no change). However, it modified for combined hardening such that:

$$\sigma_{ys}|_{prev} = \sigma_{ys}|_{initial} + (\sigma_{ys}|_1 - \sigma_{ys}|_{initial})\beta \tag{3.104}$$

where $\sigma_{ys}|_{initial}$ is the initial yield surface size. In case of pure isotropic hardening, $\beta = 1$ and:

$$\sigma_{ys}|_{prev} = \sigma_{ys}|_1 \tag{3.105}$$

and in case of pure kinematic hardening, $\beta = 0$ and:

$$\sigma_{ys}|_{prev} = \sigma_{ys}|_{initial} \tag{3.106}$$

as is required in the respective models. We see that in case of isotropic hardening, the yield surface keeps growing. In case of kinematic hardening, the yield surface does not change size and remains at its initial value. Finally, in case of combined hardening, the value of β decides the size and location of yield surface.

In the proposed model, the progressive reduction of the yield surface size is ensured with the introduction of a new factor, γ, which is a fitted exponential parameter capturing the difference between monotonic and cyclic stress-strain curves. The equations for the new formulation and explanation thereof are as follows:

$$\sigma_{ys}|_1 = \sigma_{ys} \tag{3.107}$$

Again a new parameter, $\sigma_{ys}|_0$, is introduced such that:

$$\sigma_{ys}|_0 = \sigma_{ys}|_1 \times e^{-\gamma \epsilon_{eq}^{pl}} \tag{3.108}$$

Finally, we get:

$$\sigma_{ys}|_{prev} = \sigma_{ys}|_{initial} + (\sigma_{ys}|_0 - \sigma_{ys}|_{initial})\beta \tag{3.109}$$

Figure 3.4 shows the effect of γ parameter on the yield curve. The subsequent yield size reduces progressively as a function of the equivalent plastic strain. The value of γ for pure isotropic hardening is 1.

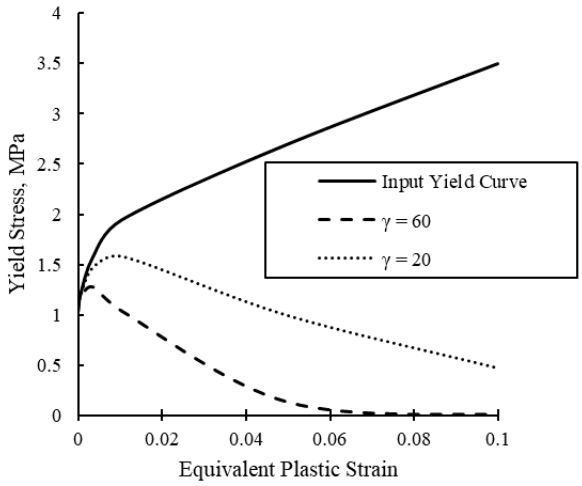

Figure 3.4: Input Yield Function

In case of pure isotropic hardening, $\beta = 1$, $\gamma = 1$ and:

$$\sigma_{ys}|_{prev} = \sigma_{ys}|_1 \tag{3.110}$$

and in case of pure kinematic hardening, $\beta = 0$ and:

$$\sigma_{ys}|_{prev} = \sigma_{ys}|_{initial} \tag{3.111}$$

as is required in the respective models.

3.4.4 Load

A cyclic load consisting of four (4) loading cycles was used for the validation as indicated in Figure 3.5. The amplitude used was 1.75 MPa, which is in the range of NAPMRC tire pressures; even though this is not a necessary condition for the evaluation. The magnitude was chosen after many trials to ensure that the quasi-static and small deformation conditions are maintained. The analysis was conducted for two values of γ; 0 and 60.

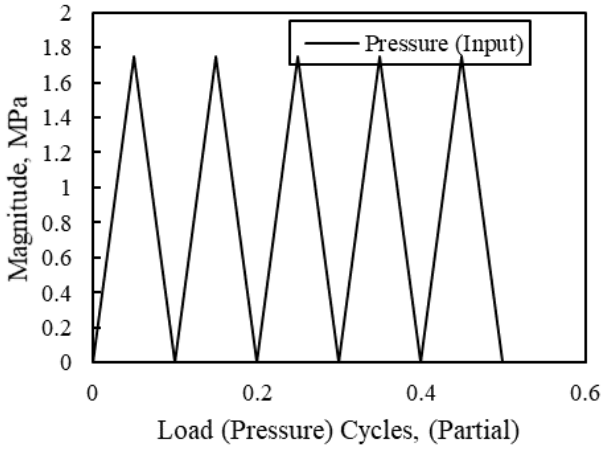

Figure 3.5: Cyclic Load for Constitutive Model Validation

3.4.5 Constitutive Modeling Results

The general deformation profile (3D) of the single element model is indicated in Figure 3.6. The legend indicates the vertical displacement, U2, at the end of the loading period, upon load removal, indicating permanent deformation.

The equivalent plastic strain is given in Figure 3.7 and vertical plastic strain is given in Figure 3.8. They were computed using constitutive package UMAT created for this study. The ABAQUS UMAT, as described earlier, has the facility to store solution dependent variables (SDVs) for convenience. Here, ϵ_{eq}^{pl} is stored as $SDV19$ as seen in the figures.

It was observed that ϵ_{eq}^{pl} increases with loading cycles, as the yield surface size in the subsequent cycle keeps decreasing when $\gamma = 60$. This decrease is a function of the yield curve. A yield curve which is realistic and applicable to the actual material being investigate is expected to pronounce the effect of the model.

Finally, the evolution of vertical component of plastic strain, ϵ_{22}^{pl}, was observed. The validation of the model is established if the this component evolves. It was noted that in the compression

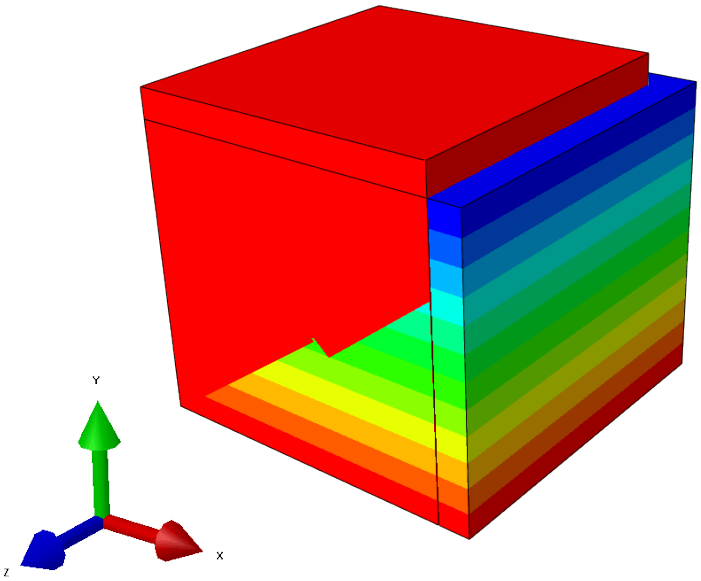

Figure 3.6: Single Element Vertical Deformation at End of Loading

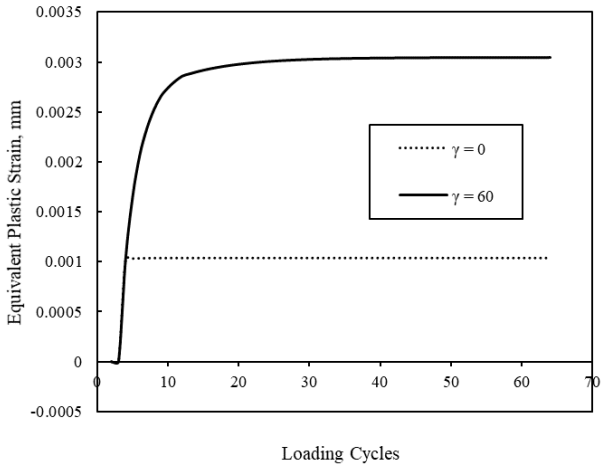

Figure 3.7: Equivalent Plastic Strain Evolution

regime, this component has a negative sign and should also evolve by increasing in the negative sense. Figure 3.8 indicates the evolution of ϵ_{22}^{pl}, which is stored as $SDV8$ for output purposes. It was seen that ϵ_{22}^{pl} increases negatively (or effectively decreases) with loading cycles, as the yield

surface size in the subsequent cycle keeps decreasing.

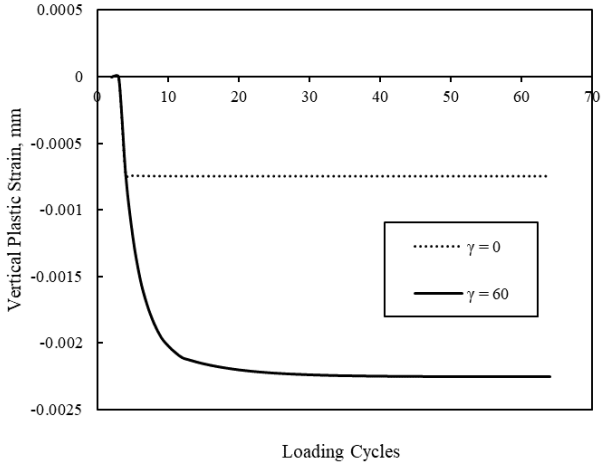

Figure 3.8: Vertical Plastic Strain Evolution

3.4.6 UMAT for ABAQUS Analysis

A constitutive user material subroutine in FORTRAN for carrying out model computations is given in APPENDIX A. Also, the standard ABAQUS subroutine for hardening is given in APPENDIX B.

4. EXPERIMENTAL DESIGN AND RESULTS

This section details the various experiments that were conducted for the purpose of this study. These include a brief description of the material properties experiments and the field testing conducted at the NAPMRC facility.

4.1 NAPMRC Field Experiment

The NAPMRC test section studied contained four outdoor lanes that were trafficked with the wheel loads. A 2D finite element study was conducted in order to simulate the rutting profile of the pavement sections during the NAPMRC field tests.

4.1.1 Heavy Vehicle Simulator, Pavement Structure and Materials, Strain Gauges

This section firstly describes the HVS-A procured by FAA and used for testing in this project, followed by depiction of the pavement sections in the various test lanes. The materials used in the pavement base, subbase, and subgrade are outlined. Finally, the asphalt strain gauges (ASG), transverse strain gauges (TSG) and longitudinal strain gauges (LSG), used in the research are described.

4.1.1.1 Heavy Vehicle Simulator

The FAA's existing National Airport Pavement Test Facility (NAPTF) and test vehicle (NAPTV) are used for full scale tests investigating the entire structure as a whole for providing insights into subgrade structural failures. In order to overcome limitations of indoor testing facilities, such as achieving the desirable pavement temperatures, which is critical in the study of performance of surface layers such as HMA and WMA, the idea of NAPMRC was conceived. The wheel load and tire pressures in combination with surface temperature are more critical than the landing gear load (due to minimum wheel load interaction affects). High tire pressure behaviours were typically characterized in the laboratory. Full-scale tests are needed so that the performance prediction models for HMA from laboratory tests can be validated/calibrated to the in-situ pavements. Full-

scale tests at high HMA temperatures are very crucial for the success of these projects. The FAA's recently acquired HVS-A provides that capability.

HVS-A is capable of applying both, bi-directional as well as unidirectional loading using a single wheel having a maximum capacity of 100,000 lb or dual wheels wherein each wheel load is 50,000 lb. The central controller facilitates automatic test sequences and communicates with the pavement instrumentation and data acquisition system. It is capable of applying a wander of $\pm$ 3 feet about the center line of the load path, resulting in a maximum wander width capacity of 6 feet.

4.1.1.2 Pavement Structure and Materials

The pavement structural sections that were tested in this study were newly constructed four lanes at the NAPMRC facility. The pavement design was in accordance with the FAARFIELD (FAA 2009) computer program. Figure 5.1 indicates the general pavement cross-section for hot mix asphalt (HMA) as well as warm mix asphalt (WMA).

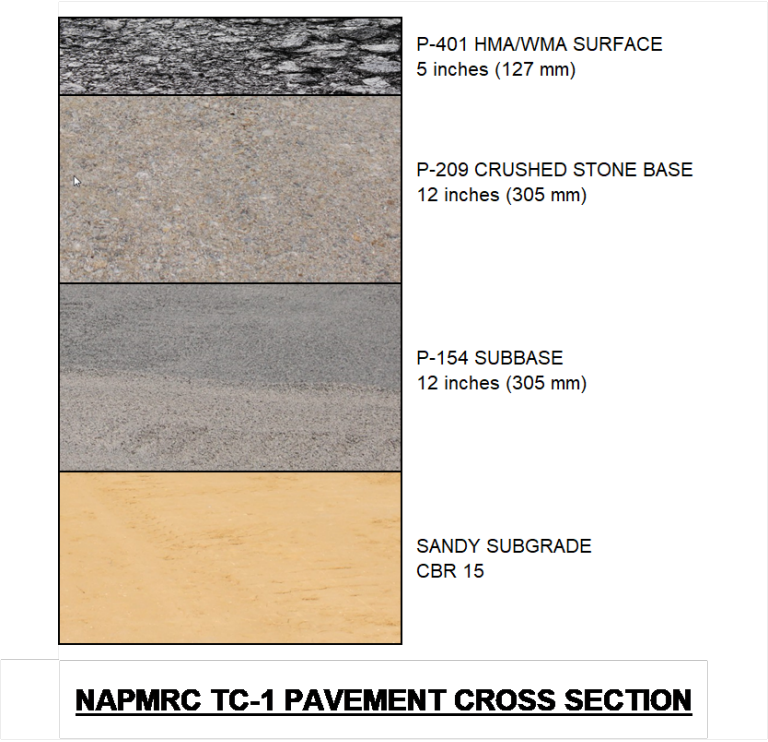

Figure 4.1: NAPMRC TC-1 Pavement Structure

The pavement structure was composed of a bottom layer of sandy subgrade having a CBR value of 15. This was overlaid with a 12 $inch$ thick subbase layer of FAA standard specification item P-154. P-154 is a subbase course composed of granular materials. Over the subbase was laid a 12 $inch$ thick base layer of FAA standard specification item P-209. P-209 is a base course composed of crushed aggregates. The top layer was a 5 $inch$ pavement course of FAA standard specification item P-401. P-401 is a pavement course composed of mineral aggregate and bituminous material mixed in a central mixing plant. The pavement course was either HMA or WMA in accordance with the experimental design indicated in sections below.

4.1.1.3 Specific Experimental Design

The NAPMRC Test Cycle-1 (TC-1) test sections consisted of four outdoor and two indoor pavement lanes as shown in Figure 4.2. Each lane was divided into North and South segments. The analysis for this work was conducted using data for the outdoor lanes, namely Lane 3 and Lane 4. Figure 4.2 depicts the TC-1 test sections layout. There were four outdoor lanes from Lane 1 through Lane 4.

The pavement structural composition for base course, subbase course, and subgrade were the same throughout the test sections. Lanes 1 and 2 consisted of a WMA pavement course having P-401 specifications, while Lanes 3 and 4 consisted of an HMA pavement course having P-401 specifications. The asphalt binder used in Lanes 1 and 3 was PG 76-22, while that used in Lanes 2 and 4 was PG 64-22.

Two types of tests were conducted, depending on the tire load: response tests and traffic tests. The test speed was 3.0 mph. Response tests were conducted at wheel loads of 20,000, 30,000, and 40,000 pounds. The load application was at different wander positions and as such, 22 passes were applied at each pavement test section at each tire load. Table 4.1 below indicates the lateral wander positions for each pass. The wander positions are measured from the left pavement edge and the center line of load application is at 36 inches.

Traffic tests were conducted at wheel loads of 61,300 pounds. The load application was at different wander positions and as such, 62 passes were applied to each pavement test section at

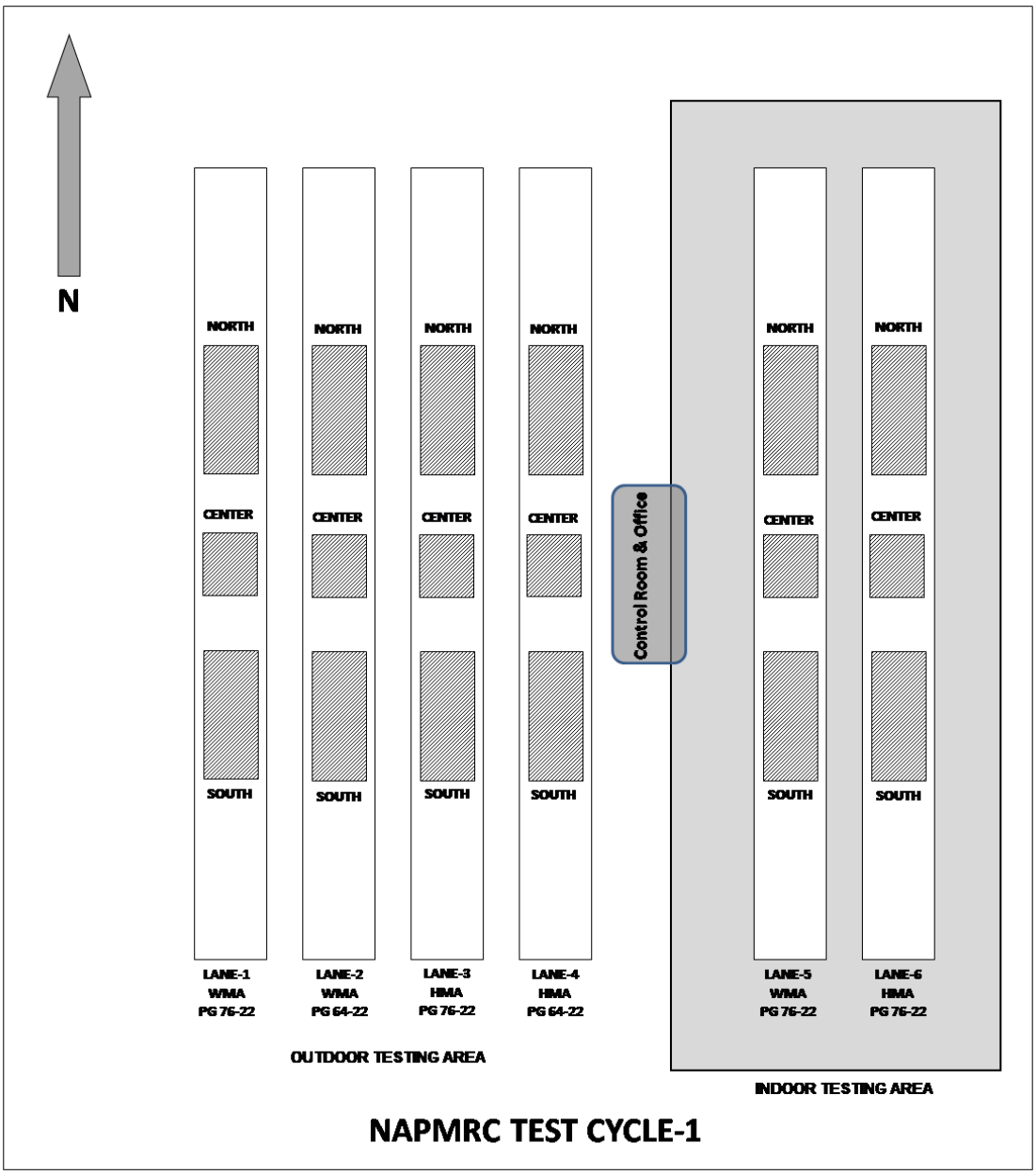

Figure 4.2: TC-1 Test Sections Layout

each tire load. Table 4.2 below indicates the lateral wander positions for each pass. The wander positions are measured from the left pavement edge and the center line of load application is at 36 inches.

Table 4.1: Lateral Wander Positions for Response Tests

Sequence No.	Wander Position, in	Track No.
1	16	-5
2	16	-5
3	20	-4
4	20	-4
5	24	-3
6	24	-3
7	28	-2
8	28	-2
9	32	-1
10	32	-1
11	36	0
12	36	0
13	40	1
14	40	1
15	44	2
16	44	2
17	48	3
18	48	3
19	52	4
20	52	4
21	56	5
22	56	5

Table 4.2: Lateral Wander Positions for Traffic Tests

Sequence No.	Wander Position, in	Track No.
1	16	-5
2	16	-5
3	24	-3
4	24	-3
5	32	-1
6	32	-1
7	40	1

Table 4.2 Continued

Sequence No.	Wander Position, in	Track No.
8	40	1
9	48	3
10	48	3
11	56	5
12	56	5
13	52	4
14	52	4
15	44	2
16	44	2
17	36	0
18	36	0
19	28	-2
20	28	-2
21	20	-4
22	20	-4
23	28	-2
24	28	-2
25	36	0
26	36	0
27	44	2
28	44	2
29	52	4
30	52	4
31	48	3

Table 4.2 Continued

Sequence No.	Wander Position, in	Track No.
32	48	3
33	40	1
34	40	1
35	32	-1
36	32	-1
37	24	-3
38	24	-3
39	32	-1
40	32	-1
41	40	1
42	40	1
43	48	3
44	48	3
45	44	2
46	44	2
47	36	0
48	36	0
49	28	-2
50	28	-2
51	32	-1
52	32	-1
53	40	1
54	40	1
55	36	0

Table 4.2 Continued

Sequence No.	Wander Position, in	Track No.
56	36	0
57	20	-4
58	20	-4
59	24	-3
60	24	-3
61	36	0
62	36	0

The four outdoor lanes, along with their North and South orientation, combined with two binder types and modifiers result in the following surface layer and tire pressure combinations. They are listed in Figure 4.3 below. The list is in accordance with the testing sequence.

4.1.1.4 NAPMRC Rutting Data

The NAPMRC Test Cycle-1 rutting data is indicated in this section in Tables 4.4 and 4.5. All the values are in millimeters, mm.

4.1.2 Material Parameters

This section describes the material parameters for asphalt, base, subbase, and subgrade layers. The analysis parameters and software used are also described.

4.1.2.1 Identification of Asphalt Layer Material Properties

The pavement section modeled was composed of an asphalt layer of FAA P-401 specification. The asphalt mix was 19 mm mix with all coarse aggregates procured from Springhouse, Springhouse, PA. The fine aggregates (Natural Sand) were procured from Hanson, Berlin, NJ. The asphalt binder content was 6%. Evotherm Type M was added for constructing the WMA layers. The percentage by weight of binder added to PG 76-22 binder was 0.5% and that for PG 64-22 was 0.4%. The main premise of the study is on characterization and rutting performance prediction of sublay-

Table 4.3: Testing Sequence and Layer Type

Sequence	Test Area Desig-nation	Surface Layer Material	Tire Pressure (psi)	Number of Loading Passes			
—	—	—	—	20,000 lb	30,000 lb	40,000 lb	61,300 lb
1	Lane-4 South (L4S)	HMA PG 64-22	210	22	22	22	62
2	Lane-2 South (L2S)	WMA PG 64-22	210	22	22	22	62
3	Lane-3 South (L3S)	HMA PG 76-22	210	22	22	22	62
4	Lane-1 South (L1S)	WMA PG 76-22	210	22	22	22	62
5	Lane-4 North (L4N)	HMA PG 64-22	254	22	22	22	62
6	Lane-2 North (L2N)	WMA PG 64-22	254	22	22	22	62
7	Lane-3 North (L3N)	HMA PG 76-22	254	22	22	22	62
8	Lane-1 North (L1N)	WMA PG 76-22	254	22	22	22	62

ers, the detailed procedure for the characterization of material properties associated with asphalt layer is therefore not mentioned. Procedure outlined in [40] was followed to analyze the dynamic modulus and phase angle to identify the viscoelastic parameters associated with PANDA-AP. More information on characterization of linear and nonlinear viscoelastic properties can found in [41].

In general, the hot mix asphalt (HMA) layer was modeled using the user material subroutine, PANDA. This allows the layer to be modeled as elastic, linear and non-linear viscoelastic, and

Table 4.4: NAPMRC Rutting Data - Lanes 1 and 2

LANE-1				LANE-2			
North		South		North		South	
Passes	Rut Depth	Passes	Rut Depth	Passes	Rut Depth	Passes	Rut Depth
0	0.0	0	0.0	0	0.0	0	0.0
18	5.0	18	4.7	18	8.3	18	9.7
48	7.6	48	7.3	48	13.6	48	13.3
124	12.3	62	8.4	74	11.7	124	17.7
186	14.7	124	11.3	124	20.5	186	20.9
248	16.0	186	13.3	186	27.8	248	25.4
310	18.7	248	14.6	248	32.9	496	37.1
372	20.4	372	17.7	310	37.6	620	37.8
496	23.3	496	19.2	372	38.7	868	45.4
620	25.8	620	21.2	496	49.8	930	47.6
868	31.0	868	25.3	1246	54.2	—	—
1116	35.2	1550	33.5	—	—	—	—
1364	39.3	1984	37.3	—	—	—	—
1612	41.5	2604	42.1	—	—	—	—
1860	44.0	3224	44.1	—	—	—	—
2356	49.8	3906	49.5	—	—	—	—
2852	55.9	—	—	—	—	—	—
2914	57.3	—	—	—	—	—	—

viscoplastic with or without hardening-relaxation. The viscodamage- and moisture damage-related parameters were assigned conventional values since these properties were not examined in the present study scope. Some material parameters used for modeling the asphalt layer in this study were obtained from the research group at the University of Kansas, Lawrence. They were from NAPTF pavement layers. The asphalt material parameters are presented in Table 4.6 for linear viscoelastic, Table 4.7 for non-linear viscoelastic, Tables 4.8, 4.9, and 4.10 for viscoplastic, and Table 4.11 for hardening-relaxation.

Table 4.5: NAPMRC Rutting Data - Lanes 3 and 4

LANE-3				LANE-4			
North		South		North		South	
Passes	Rut Depth	Passes	Rut Depth	Passes	Rut Depth	Passes	Rut Depth
0	0	0	0.0	0	0.0	0	0.0
18	4.1	18	4.2	18	7.9	18	5.2
48	6.6	48	6.0	48	13.0	48	9.1
74	5.8	62	7.3	124	23.2	62	11.8
124	10.8	124	10.1	186	29.6	124	15.5
186	13.0	186	12.6	248	35.0	186	19.2
248	14.4	248	14.5	496	53.4	248	23.2
310	16.4	372	18.2	620	60.5	310	27.3
372	15.7	496	20.7	—	—	372	30.9
496	19.6	620	23.4	—	—	434	33.6
620	22.4	868	26.8	—	—	496	34.8
868	25.6	1054	28.5	—	—	620	38.8
1116	29.5	1240	29.9	—	—	806	44.5
1364	32.4	1240	29.3	—	—	992	48.5
1612	34.2	1550	32.1	—	—	—	—
1860	37.2	1736	33.1	—	—	—	—
2108	38.7	2356	35.4	—	—	—	—
2356	39.9	2666	36.9	—	—	—	—
2604	41.5	3286	39.9	—	—	—	—
2852	43.6	3534	40.2	—	—	—	—
3100	45.0	—	—	—	—	—	—
3968	48.8	—	—	—	—	—	—

Table 4.6: Linear Viscoelastic Parameters

Mix type	**HMA of PG 76-22**		**WMA of PG 76-22**		**HMA of PG 64-22**		**WMA of PG 64-22**	
i	D_i	λ_i	D_i	λ_i	D_i	λ_i	D_i	λ_i
Prony Series Number	Creep Compliance Coefficients (1/MPa)	Time of Retardation (1/s)	Creep Compliance Coefficients (1/MPa)	Time of Retardation (1/s)	Creep Compliance Coefficients (1/MPa)	Time of Retardation (1/s)	Creep Compliance Coefficients (1/MPa)	Time of Retardation (1/s)
0	5.58E-05	-	5.63E-05	-	6.20E-05	-	3.85E-05	-
1	2.54E-05	4.35E+03	2.37E-05	4.21E+03	3.70E-05	1.65E+03	3.54E-05	7.47E+04
2	2.73E-05	4.01E+02	2.40E-05	3.93E+02	3.89E-05	1.78E+02	4.33E-05	5.95E+03
3	7.23E-05	3.69E+01	6.23E-05	3.67E+01	1.00E-04	1.92E+01	6.91E-05	4.73E+02
4	1.45E-04	3.40E+00	1.23E-04	3.42E+00	2.08E-04	2.07E+00	1.52E-04	3.76E+01
5	4.14E-04	3.13E-01	3.43E-04	3.19E-01	6.39E-04	2.24E-01	3.82E-04	2.99E+00
6	9.94E-04	2.88E-02	8.12E-04	2.98E-02	1.26E-03	2.41E-02	1.13E-03	2.38E-01
7	2.94E-03	2.65E-03	2.41E-03	2.78E-03	4.97E-03	2.60E-03	3.61E-03	1.89E-02
8	5.96E-03	2.44E-04	4.23E-03	2.59E-04	8.35E-03	2.81E-04	1.77E-02	1.51E-03
9	2.07E-02	2.25E-05	1.50E-02	2.42E-05	2.44E-02	3.03E-05	2.39E-02	1.20E-04
Shift Parameters								
$Temp$	a_T	$Log(a_T)$	a_T	$Log(a_T)$	a_T	$Log(a_T)$	a_T	$Log(a_T)$
-10	13762.86	4.1387	11578.01	4.0636	5813.25	3.7644	4023.92	3.6046
4.4	112.96	2.0529	106.61	2.0278	76.11	1.8815	65.54	1.8165
21.1	0.7301	-0.1366	0.7311	-0.136	0.7474	-0.1265	0.7527	-0.1234
37.8	0.0083	-2.0799	0.0082	-2.088	0.0113	-1.9456	0.012	-1.9194
54.4	0.0002	-3.7674	0.0002	-3.8184	0.0003	-3.5667	0.0003	-3.5622

Table 4.7: Non-Linear Viscoelastic Parameters

Mixture type			**HMA of PG 76-22**				**WMA of PG 76-22**				**HMA of PG 64-22**				**WMA of PG 64-22**			
Block		**Stress**	g_2	g_1	$g_2 \times g_1$	η	g_2	g_1	$g_2 \times g_1$	η	g_2	g_1	$g_2 \times g_1$	η	g_2	g_1	$g_2 \times g_1$	η
1	1	140	0.55	0.52	0.29	1.48	3.74	0.8	2.99	1.45	0.85	1.21	1.03	1.39	—	—	—	—
—	2	168	0.54	0.53	0.29	1.18	3.74	0.82	3.08	1.22	1.19	0.99	1.18	1.26	—	—	—	—
—	3	202	0.52	0.57	0.3	1.03	3.37	0.79	2.67	1.03	1.43	0.87	1.25	1.03	—	—	—	—
—	4	242	0.47	0.63	0.3	0.92	2.93	0.82	2.4	0.92	1.18	0.99	1.17	0.92	—	—	—	—
—	5	290	0.48	0.62	0.29	0.82	2.5	0.85	2.13	0.82	1.06	0.99	1.05	0.82	1.13	1.08	1.22	0.82
—	6	348	0.56	0.52	0.29	0.74	2.15	0.88	1.9	0.76	0.99	0.94	0.93	0.74	0.99	1.07	1.05	0.74
—	7	418	0.44	0.73	0.32	0.67	1.95	0.88	1.72	0.67	0.84	0.97	0.81	0.67	0.81	1.11	0.89	0.67
—	8	502	0.42	0.76	0.32	0.61	1.68	0.92	1.54	0.62	0.72	1.01	0.73	0.61	0.66	1.15	0.76	0.61
2	9	202	0.69	0.57	0.39	1.02	3.19	0.83	2.64	1.02	1.32	0.93	1.22	1.02	1.38	1.11	1.53	1.03
—	10	242	0.64	0.59	0.38	0.91	2.72	0.86	2.33	0.91	1.07	1.01	1.08	0.91	1.19	1.13	1.34	0.93
—	11	290	0.62	0.59	0.36	0.82	2.38	0.85	2.02	0.82	0.95	1	0.96	0.82	1.07	1.05	1.12	0.81
—	12	348	0.56	0.62	0.35	0.74	1.97	0.89	1.76	0.74	0.83	1.04	0.86	0.74	0.89	1.08	0.96	0.74
—	13	418	0.46	0.75	0.34	0.67	1.68	0.93	1.56	0.67	0.75	1.02	0.77	0.67	0.71	1.16	0.82	0.67
—	14	502	0.56	0.57	0.32	0.61	1.42	0.97	1.39	0.61	0.63	1.1	0.69	0.61	0.59	1.21	0.72	0.61

Table 4.7 Continued

Mixture type			**HMA of PG 76-22**				**WMA of PG 76-22**				**HMA of PG 64-22**				**WMA of PG 64-22**			
Block		**Stress**	g_2	g_1	$g_2 \times g_1$	η	g_2	g_1	$g_2 \times g_1$	η	g_2	g_1	$g_2 \times g_1$	η	g_2	g_1	$g_2 \times g_1$	η
—	15	602	0.41	0.77	0.31	0.57	1.23	1	1.24	0.57	0.53	1.15	0.61	0.57	0.52	1.19	0.62	0.57
—	16	722	0.36	0.85	0.31	0.53	1.08	1.01	1.09	0.53	0.49	1.13	0.55	0.53	0.46	1.19	0.54	0.53
3	17	290	0.68	0.64	0.44	0.82	2.22	0.88	1.96	0.82	0.95	1.02	0.97	0.81	0.91	1.14	1.03	0.81
—	18	348	0.55	0.73	0.4	0.74	1.85	0.92	1.7	0.74	0.82	1.02	0.84	0.73	0.8	1.14	0.91	0.74
—	19	418	0.52	0.71	0.37	0.67	1.55	0.96	1.5	0.67	0.7	1.06	0.74	0.67	0.66	1.19	0.79	0.67
—	20	502	0.44	0.79	0.34	0.61	1.6	0.42	0.67	0.61	0.61	1.09	0.66	0.61	0.55	1.23	0.68	0.61
—	21	602	0.39	0.81	0.31	0.57	1.14	1.01	1.15	0.57	0.54	1.09	0.58	0.57	0.48	1.21	0.59	0.57
—	22	722	0.37	0.81	0.3	0.53	1.01	1.05	1.05	0.53	0.47	1.12	0.53	0.53	0.44	1.18	0.52	0.53
—	23	867	0.35	0.82	0.29	0.5	0.87	1.09	0.95	0.5	0.39	1.23	0.48	0.5	0.38	1.19	0.45	0.5
—	24	1040	0.3	0.91	0.27	0.47	0.76	1.14	0.86	0.47	0.36	1.21	0.43	0.47	0.27	1.46	0.4	0.47
4	25	418	0.57	0.7	0.4	0.67	—	—	—	—	0.75	1.02	0.77	0.67	0.68	1.11	0.75	0.67
—	26	502	0.45	0.81	0.36	0.61	—	—	—	—	0.59	1.12	0.67	0.61	0.5	1.29	0.65	0.61
—	27	602	0.4	0.81	0.33	0.57	—	—	—	—	0.49	1.18	0.58	0.57	0.42	1.35	0.57	0.57
—	28	722	0.35	0.86	0.3	0.53	—	—	—	—	0.45	1.16	0.52	0.53	0.39	1.31	0.51	0.53

Table 4.7 Continued

Mixture type			**HMA of PG 76-22**				**WMA of PG 76-22**				**HMA of PG 64-22**				**WMA of PG 64-22**			
Block		**Stress**	g_2	g_1	$g_2 \times g_1$	η	g_2	g_1	$g_2 \times g_1$	η	g_2	g_1	$g_2 \times g_1$	η	g_2	g_1	$g_2 \times g_1$	η
—	29	867	0.32	0.89	0.28	0.5	—	—	—	—	0.39	1.21	0.47	0.5	0.33	1.32	0.44	0.5
—	30	1040	0.28	0.93	0.26	0.47	—	—	—	—	0.36	1.18	0.42	0.47	0.26	1.47	0.39	0.47
—	31	1248	0.26	0.94	0.25	0.45	—	—	—	—	0.34	1.16	0.39	0.45	0.24	1.45	0.35	0.45
—	32	1498	0.24	0.97	0.24	0.43	—	—	—	—	0.27	1.31	0.35	0.43	0.22	1.41	0.31	0.43
5	33	602	0.43	0.84	0.36	0.57	—	—	—	—	0.52	1.16	0.61	0.57	—	—	—	—
—	34	722	0.37	0.87	0.32	0.53	—	—	—	—	0.46	1.15	0.53	0.53	—	—	—	—
—	35	867	0.34	0.86	0.29	0.5	—	—	—	—	0.38	1.22	0.47	0.5	—	—	—	—
—	36	1040	0.3	0.87	0.26	0.47	—	—	—	—	0.33	1.26	0.42	0.47	—	—	—	—
—	37	1248	0.26	0.95	0.25	0.45	—	—	—	—	0.29	1.32	0.38	0.45	—	—	—	—
—	38	1498	0.23	1.03	0.23	0.43	—	—	—	—	0.26	1.34	0.34	0.43	—	—	—	—
—	39	1797	0.2	1.06	0.22	0.41	—	—	—	—	0.24	1.29	0.31	0.41	—	—	—	—
—	40	2157	0.2	0.98	0.2	0.4	—	—	—	—	0.21	1.32	0.28	0.4	—	—	—	—
6	41	867	0.37	0.86	0.32	0.5	—	—	—	—	0.4	1.18	0.48	0.5	—	—	—	—
—	42	1040	0.31	0.89	0.27	0.47	—	—	—	—	0.36	1.17	0.42	0.47	—	—	—	—

Table 4.7 Continued

Mixture type			**HMA of PG 76-22**				**WMA of PG 76-22**				**HMA of PG 64-22**				**WMA of PG 64-22**			
Block		**Stress**	g_2	g_1	$g_2 \times g_1$	η	g_2	g_1	$g_2 \times g_1$	η	g_2	g_1	$g_2 \times g_1$	η	g_2	g_1	$g_2 \times g_1$	η
—	43	1248	0.26	0.96	0.25	0.45	—	—	—	—	0.29	1.25	0.37	0.45	—	—	—	—
—	44	1498	0.23	0.98	0.22	0.43	—	—	—	—	0.25	1.31	0.32	0.43	—	—	—	—
—	45	1797	0.2	1.04	0.21	0.41	—	—	—	—	0.23	1.26	0.29	0.41	—	—	—	—
—	46	2157	0.19	1.03	0.2	0.4	—	—	—	—	0.19	1.36	0.26	0.4	—	—	—	—
—	47	2588	0.19	1	0.19	0.39	—	—	—	—	0.14	1.26	0.18	0.39	—	—	—	—

Table 4.8: Viscoplastic Parameters (Part 1)

Mixture	Binder	Average saturated yield stress (kPa)
HMA	PG 76-22	1553
HMA	PG 64-22	1403
WMA	PG 76-22	1452
WMA	PG 64-22	1332

Table 4.9: Viscoplastic Parameters (Part 2)

Parameter	**Recommended value**	**Physical significance**	**Assumed value**
α	0.15-0.3	Related to the angle of friction of the asphalt mixtures.	0.25
β	$\alpha - 0.05$	Related to the angle of friction and the dilation characteristics of asphalt mixtures.	0.2
d^{vp}	0.778	Ratio of yield strength in tension to that in compression. Fixed for most asphalt mixes.	0.778
σ_y^0	100 kPa	Yield stress quantity	100 kPa

4.1.2.2 Identification of Base, Subbase, and Subgrade Layer Material Properties

The granular base and subbase materials used in the pavement sections were specified as P-209 and P-154, respectively. The NAPMRC P-209 base is a crushed aggregate base course, and the NAPMRC P-154 subbase is a course manufactured screening according to FAA Advisory Circular Number 150/5370-10F.

Table 4.10: Viscoplastic Parameters (Part 3)

Mixture	Binder	Initial Yield Strength (kPa), k_0	Compressive Strength of Asphalt Material (kPa), k_1	Strain Hardening Rate (kPa), k_2	Viscoplastic Rate Sensitivity Exponent, N	Viscoplastic Fluidity (1/s), Γ^{vp}
HMA	PG 76-22	142	1411	180	1.92	0.008
HMA	PG 64-22	53	1350	170	2.06	0.016
WMA	PG 76-22	57	1395	173	1.98	0.009
WMA	PG 64-22	52	1280	165	2.13	0.023

Table 4.11: Hardening-Relaxation Parameters

Mixture	Binder	Hardening-relaxation Exponent, S_1	Hardening-relaxation Parameter (kPa), S_2	Hardening-relaxation Fluidity (1/s), Γ^{h-r}
HMA	PG 76-22	0.332	2.31E+05	2.29E-05
HMA	PG 64-22	0.347	9.67E+04	3.20E-05
WMA	PG 76-22	0.301	2.10E+05	2.22E-05
WMA	PG 64-22	0.336	6.25E+04	3.15E-05

The base layer was modeled either as linear elastic isotropic using the Drucker-Prager model (DP) (without CAP) depending on the type of analysis that was being conducted in this study. The subbase layer was modeled as linear elastic isotropic. The subgrade layer was, in every case, modeled as linear elastic isotropic.

When modeled as linear elastic isotropic, a Young's modulus of 376 MPa and a Poisson's ratio of 0.35 were used for the base. As mentioned above in this report, the subgrade in every case was modeled as linear elastic isotropic with Young's modulus of 40 MPa and a Poisson's ratio of 0.40.

When the base was modeled as DP, the ABAQUS subroutine of "extended Drucker-Prager model" along with subroutine "Drucker-Prager Hardening" was used. This elasto-plastic formulation did not assume any temperature dependency. The material angle of friction was 40°, the flow stress ratio was 1, and the dilation angle was 10°. Based on available material properties in liter-

ature, a hardening function was used in which the yield stress depends only on the plastic strain. In this case, a plot of uniaxial compression yield stress versus uniaxial compression plastic strain was used.

4.1.3 Finite Element Analysis

This section presents the two-dimensional (2D) finite element (FE) study that was conducted in order to simulate the rutting and strain profile of the eight pavement sections during the NAPMRC field tests. The geometry of the FE model, which includes the mesh and the loading scheme is described. This is followed by a description of the material properties. The finite element analysis was conducted using the commercially available FE software ABAQUS. The version used was 6.14.2.

4.1.3.1 Geometry of the FE Model

The pavement section consists of a 2D plane strain half-section of dimensions 1600.0×1220.0 mm in width and height, respectively. The 2D FE mesh is shown in Figure 4.3. In order to simulate plane strain conditions, two boundary conditions were imposed on the model. Firstly, the vertical edge at the middle dividing the pavement section into two equal halves was constrained (fixed) against movement in the horizontally. Secondly, the bottom horizontal edge was constrained against movement vertically. The direction "X" indicated in the figure was named the positive 1-1 direction. Hence, the components of stress (S11), strain (E11), and displacement (U1) in this direction are named accordingly in the ABAQUS analysis output and results. Similarly, the "Y" direction was named positive 2-2. Hence, the direction positive 3-3 direction is the one perpendicular to the plane of the paper.

Two element types were used in this analysis. Figure 5.4 shows the mesh with the element types. The element type used for the central portion of the mesh (shaded white) was the ABAQUS continuum plane strain four-node element with reduced integration (CPE4R). The element type used for the portions at the extreme right of the mesh (shaded green) was the ABAQUS continuum infinite plane strain four-node element (CINPE4). The infinite elements were used primarily for

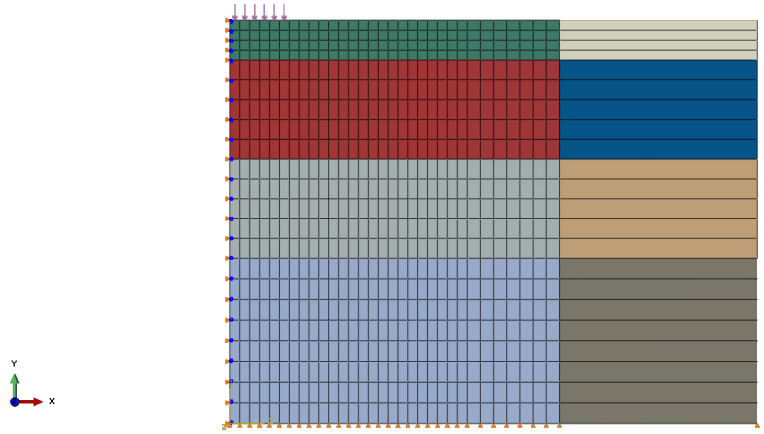

Figure 4.3: Two-dimensional FE Mesh

computational simplicity and to represent realistic boundary conditions.

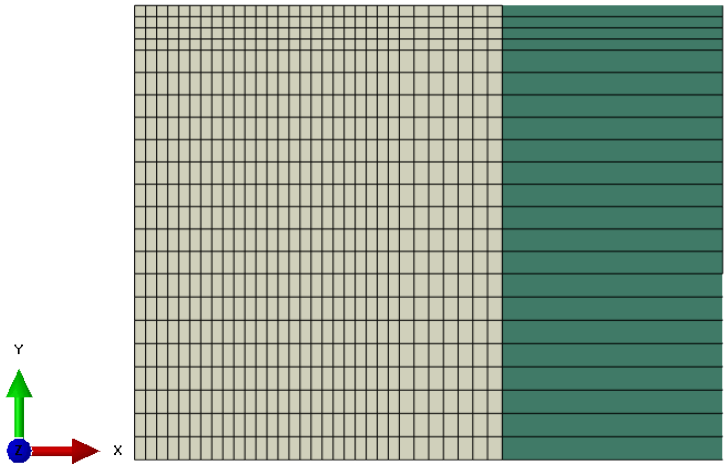

Figure 4.4: Element Types

The various sections used in the mesh are indicated in Figure 4.3 above. A maximum element aspect ratio of 1.6 was used. Element sizes used under the loads was $30 \times 30\ mm^2$ in asphalt section of the materials, shaded green. Maximum element size used, other than the infinite elements, was in the subgrade portion in the area farthest from loading and this was $40.0 \times 62.5\ mm^2$.

4.1.3.2 Loading Assumptions

The wheel load is of the type pressure, and is applied symmetrically at the middle on the top of pavement section. For calculation purpose, the tire imprint was assumed to be rectangular with the transverse dimension as 360 mm. In this study, four different tire loads were applied to the pavement, each with two different tire pressures. Hence, computationally in a 2D analysis for a constant tire pressure, an increase in load translates into an equivalent increase in the loading application time of each cycle. This loading time is the time the tire takes to traverse the distance equal to the longitudinal dimension of the tire imprint.

The load was applied in cyclic manner. The loading time of each cycle was calculated as the time the tire takes to traverse the longitudinal tire imprint dimension with a speed of 3.0 mph.

Frictional and tangential loading arising out of the wheel contact with asphalt surface were neglected. The loading was assumed to be applied on an infinite stripe bar along the length of the pavement at the center for a width of 360 mm. Hence, the assumed width (transverse to path of loading) of the tire imprint (or loading area) was 360 mm. From this, the length (in the longitudinal direction) of the tire imprint was calculated from two known quantities during testing: the tire load (20,000, 30,000, 40,000, or 61,300 pounds, depending on response/traffic tests) and tire pressure (254/210 psi for North/South lanes). Once this length was known, the duration of the load impulse was calculated by dividing the length by the speed of the tire. In this study, since only Lane 3 (North) and Lane 4 (North) were analyzed, a tire pressure of 254 psi (or 1.75 MPa) was used.

As mentioned above, the total number of passes including response and traffic tests for each lane were 128, which implies 128 cycles of loading and rest periods. However, for the purpose of the study, the rest periods were neglected by proving that in the present material formulation, there is no significant difference in the surface displacement under the load center point. Also, tire

wander was neglected. Table 4.12 indicates the loading durations for single cycle load application of each tire load and tire pressure combination. Numbers in parentheses indicate respective rest period durations.

Table 4.12: Loading Duration for Single Cycle Application

Single Loading Duration (for 1000 lb load), s					
Lane	Tire Pressure, psi	20	30	40	61.3
North	254	0.1 (25)	0.2 (25)	0.2 (25)	0.35 (35)

Figure 4.5 indicates a typical loading pattern. The pattern consists of loading applications as given hereunder.

1. Response test: 22 cycles of 20,000 lb load with loading time of 0.1 s and rest period (optional and as applicable) of 25 s, followed by,

2. Response test: 22 cycles of 30,000 lb load with loading time of 0.2 s and rest period (optional and as applicable) of 25 s, followed by,

3. Response test: 22 cycles of 40,000 lb load with loading time of 0.2 s and rest period (optional and as applicable) of 25 s, followed by,

4. Traffic test: 62 cycles of 61,300 lb load with loading time of 0.35 s and rest period (optional and as applicable) of 35 s.

The total loading cycles from (1) through (4) above amount to 128. Also, as indicated above in this section, in a 2D simulation, an increased load translates into an increased longitudinal tire imprint dimension and ultimately, into an increased loading time. However, the loading time of (2) and (3) above (0.2 s) is assumed same after rounding up to one decimal place and for amplitude computational simplicity.

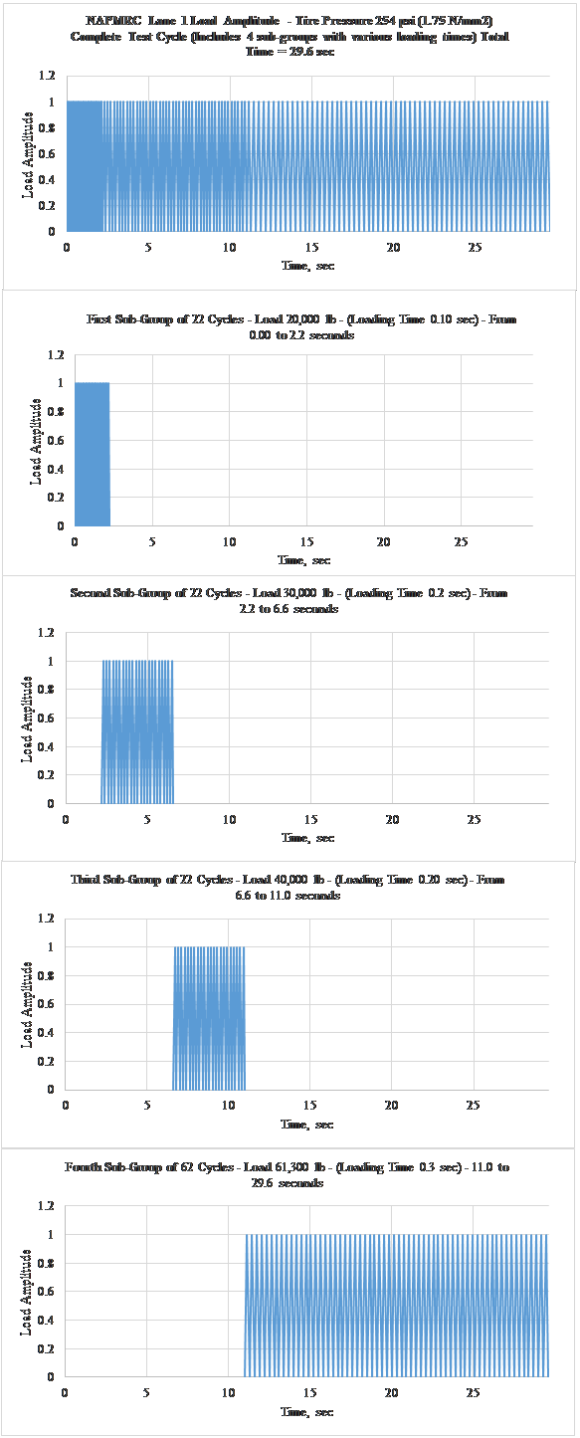

Figure 4.5: Typical NAPMRC Loading Pattern with No Rest Periodn

4.1.3.3 Wander

As described in Section 4.1.1.3, tire wander was applied in the NAPMRC experiment. However, all the simulations and validations conducted in this study were conducted without the application of any tire wander. Consequently, it is assumed that all tire load is applied in the same wheel track from start to the end of the analysis.

4.1.4 Validation with Full-Scale Accelerated Pavement Tests

The results of the FE analysis are presented in this section. As applicable and mentioned section-wise, Lane 3 and Lane 4 (North) analysis was conducted and compared with NAPMRC field rutting data obtained from the accelerated pavement testing on the respective lanes.

4.1.4.1 Applicability of Rest Period

As calculated from the data in Table 4.12, the total time required to complete 128 loading cycles with rest period is 3814.75 s and with no rest period is 29.6 s. It was evident that in order to proceed further with this study, it is essential to check the applicability of the rest period for the present structural modeling in view of the very large computational time difference. This study was conducted only on Lane 4. Six different cases were studied as follows.

1. 128 load cycles with rest period with (a) base linear elastic isotropic and (b) base DP.
2. 128 load cycles with no rest period with (a) base linear elastic isotropic and (b) base DP.
3. 2914 load cycles with no rest period with (a) base linear elastic isotropic and (b) base DP.

4.1.4.2 Load Cycles (128) with Rest Period

Figure 4.6 below indicates the deformation profile with linear elastic isotropic base and Figure 4.7 below indicates the deformation profile with elasto-plastic (DP) base. The vertical displacement (U2) on top of the asphalt layer under the center of load is plotted against time.

In either case, the asphalt layer was modeled as nonlinear viscoelastic (NLVE) and visoplastic with hardening-relaxation and (VP-HR). Furthermore, the subbase and the subgrade were both

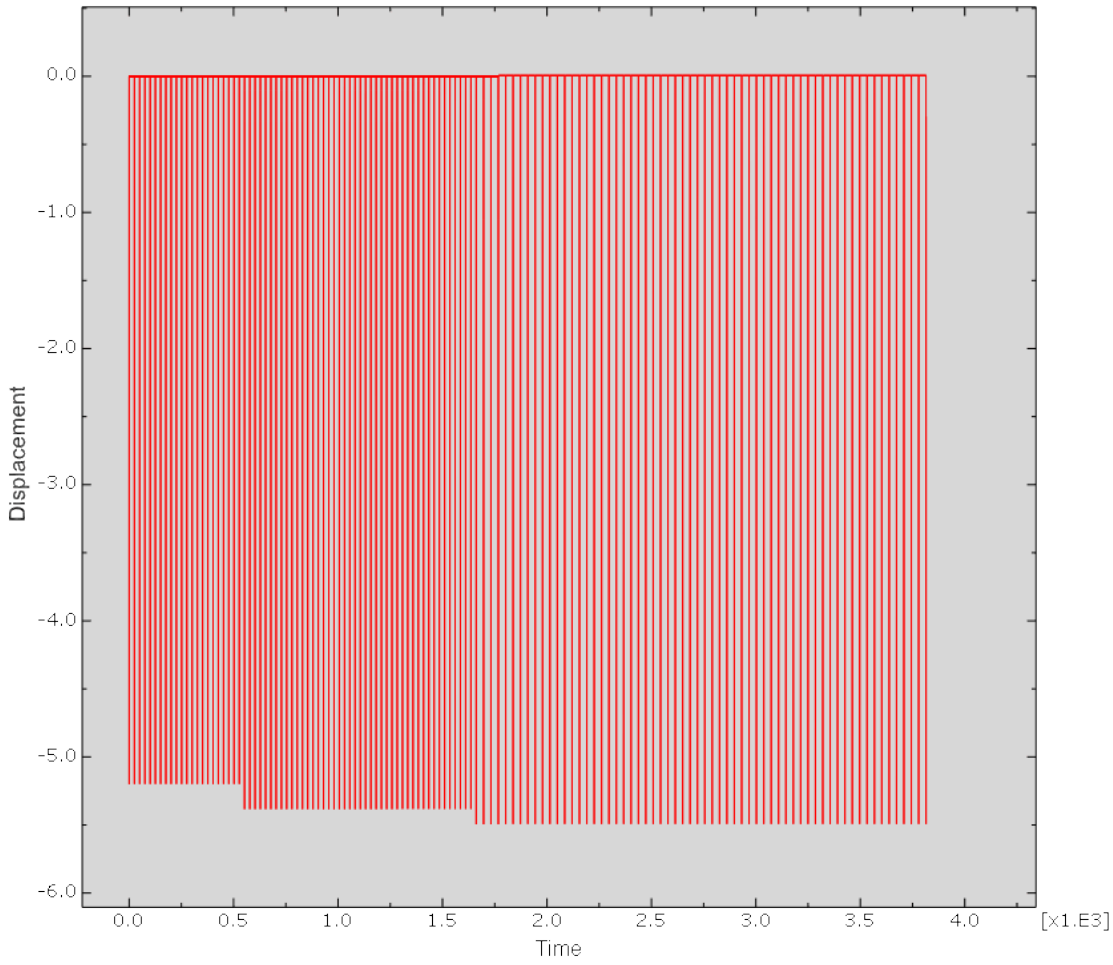

Figure 4.6: Deformation Profile with Elastic Base

modeled as linear elastic isotropic. As indicated in section above, the structure was subjected to 128 loading cycles with rest periods. The total loading time was, thus, 3814.75 s.

In both the cases, it is seen the peak displacement does not evolve after 67 cycles. After 66 load cycle applications (when the response tests have ended), the 67th load cycles is the first cycle of the traffic test. Here, the loading time increases from 0.2 to 0.35 s. Subsequently, after this cycle, peak displacement stops evolving and is the same up to the last loading cycle. The last peak displacement was about 5.5 mm for the elastic case and about 8.5 mm for the DP case. Also, the computational time, as recorded in the central processing unit (CPU) of the Texas A&M University High Performance Research Computing (TAMU HPRC) was about 15.27 $hours$ for the

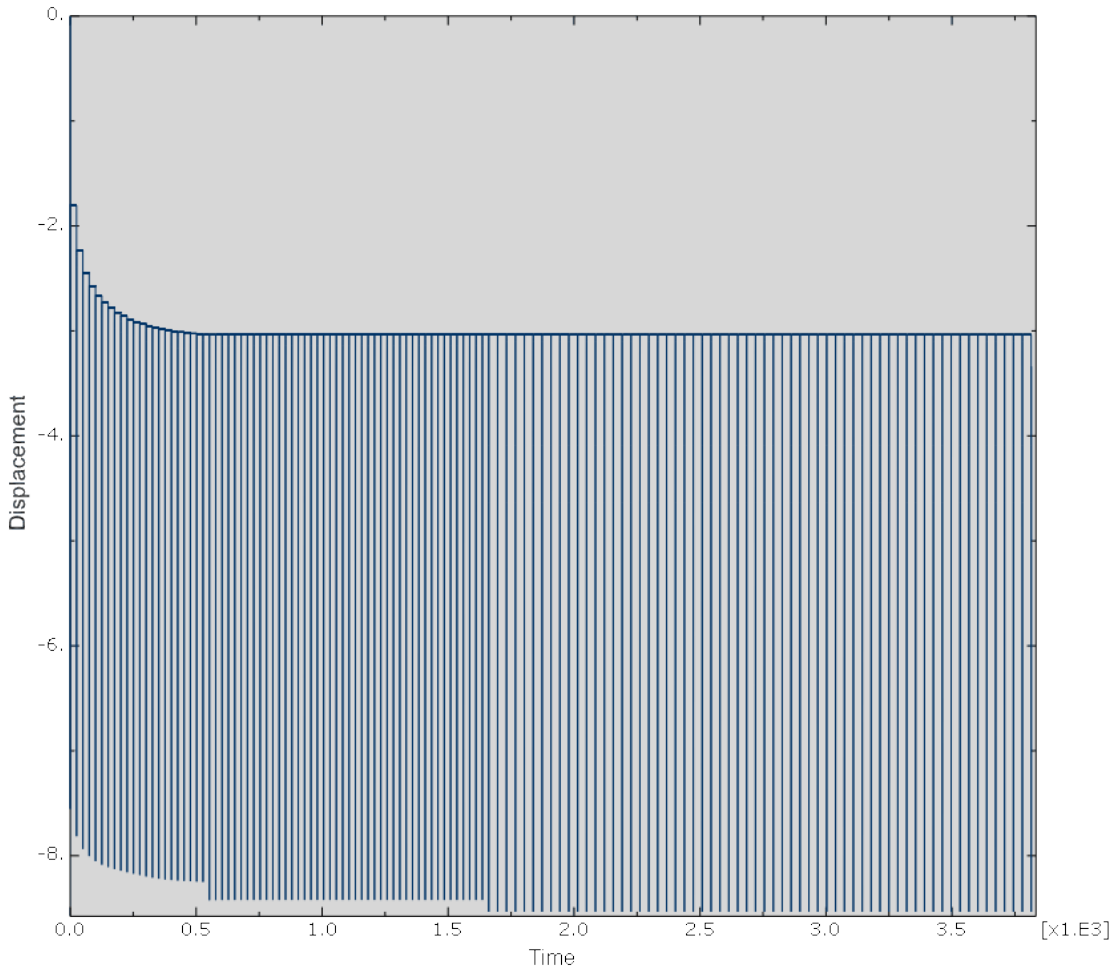

Figure 4.7: Deformation Profile with DP Base

elastic case and about 16.51 $hours$ for the plastic case. The CPU time and peak displacements for various cases run are presented in Table 4.13 and 4.14, respectively.

Table 4.13: Computational Time of FE Analysis

CPU Computational Time, hours		
Loading Type	Base Elastic	Base DP
Rest period (128 cycles)	15.27	16.51
No rest period (128 cycles)	0.14	0.2
No rest period (2914 cycles)	2.63	3.91

Table 4.14: Peak Displacements for Various Cases

Peak Displacement, mm		
Loading Type	Base Elastic	Base DP
Rest period (128 cycles)	-5.49262	-8.53479
No rest period (128 cycles)	-5.58274	-8.26923
No rest period (2914 cycles)	-5.58753	-8.51975

4.1.4.3 Load Cycles (128) with No Rest Period

Figure 4.8 below indicates the deformation profile with linear elastic isotropic base and Figure 4.9 below indicates the deformation profile with elasto-plastic (DP) base. The vertical displacement (U2) on top of the asphalt layer under the center of load is plotted against time.

In either case, the asphalt layer was modeled as nonlinear viscoelastic (NLVE) and visoplastic with hardening-relaxation and (VP-HR). Furthermore, the subbase and the subgrade were both modeled as linear elastic isotropic. As indicated in above, the structure was subjected to 128 loading cycles with no rest periods. The total loading time was, thus, 29.6 s.

In both the cases, with or without rest period, it is seen the peak displacement does not evolve after 67 cycles. Beyond 67^th cycle, peak displacement stops evolving and is the same up to the last loading cycle. The last peak displacement was about 5.6 mm for the elastic case and about 8.3 mm for the DP case, while the respective CPU times were 0.14 and 0.20 $hours$ as indicated in Table 4.13 and 4.14.

4.1.4.4 General Conclusions and Comparison with 2914 Cycles and No Rest Period

Finally, as a part of study of the applicability of the rest period, the cases were also run for a total of 2914 cycles with no rest period. The rutting data for NAPMRC accelerated pavement testing indicated that all the Lanes (1 through 8) were tested up to failure (defined as 1 inch rutting) and beyond. The second highest number of cycles for which any lane was tested for was 2914 cycles. Hence, after the completion of response tests (66 cycles), the traffic test (which starts at 67th cycle) was continued up to 2914th cycle of loading. In either case, the asphalt layer was

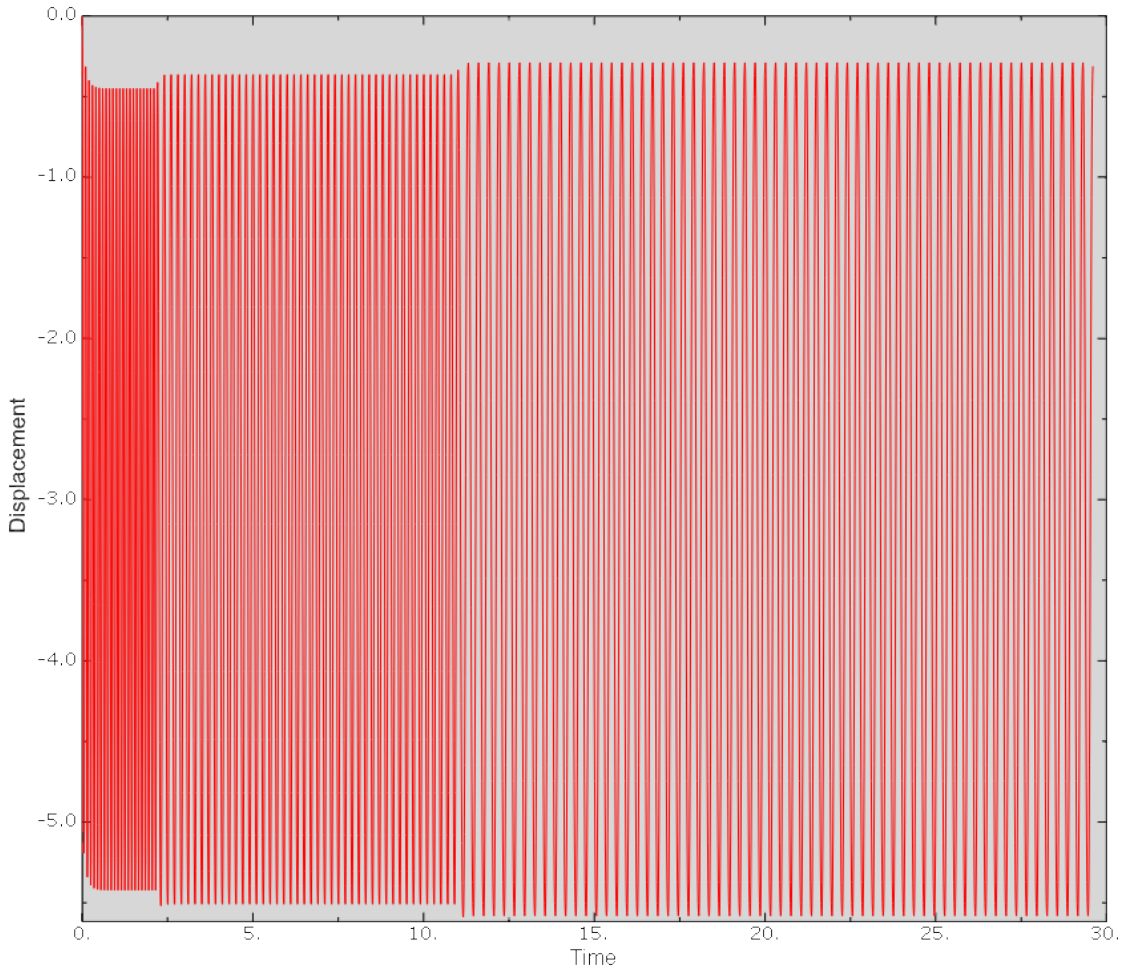

Figure 4.8: Deformation Profile with Elastic Base

modeled as nonlinear viscoelastic (NLVE) and visoplastic with hardening-relaxation and (VP-HR). Furthermore, the subbase and the subgrade were both modeled as linear elastic isotropic. The deformation profile for this case is not presented. However, Figures 4.10 and 4.11 indicate two plots of peak displacement versus load cycle number with linear elastic isotropic base and elasto-plastic (DP) base for up to 200 cycles only. The peak displacements of the cases studied in Sections 4.1.4.2 and 4.1.4.3 above are also plotted for respective elastic base and DP base cases.

It is seen the peak displacement does not evolve after 67 cycles. Beyond the 67th cycle, the peak displacement stops evolving and is constant up to the last loading cycle. The last peak displacement was about 5.6 mm for the elastic case and about 8.5 mm for the DP case, while the respective CPU

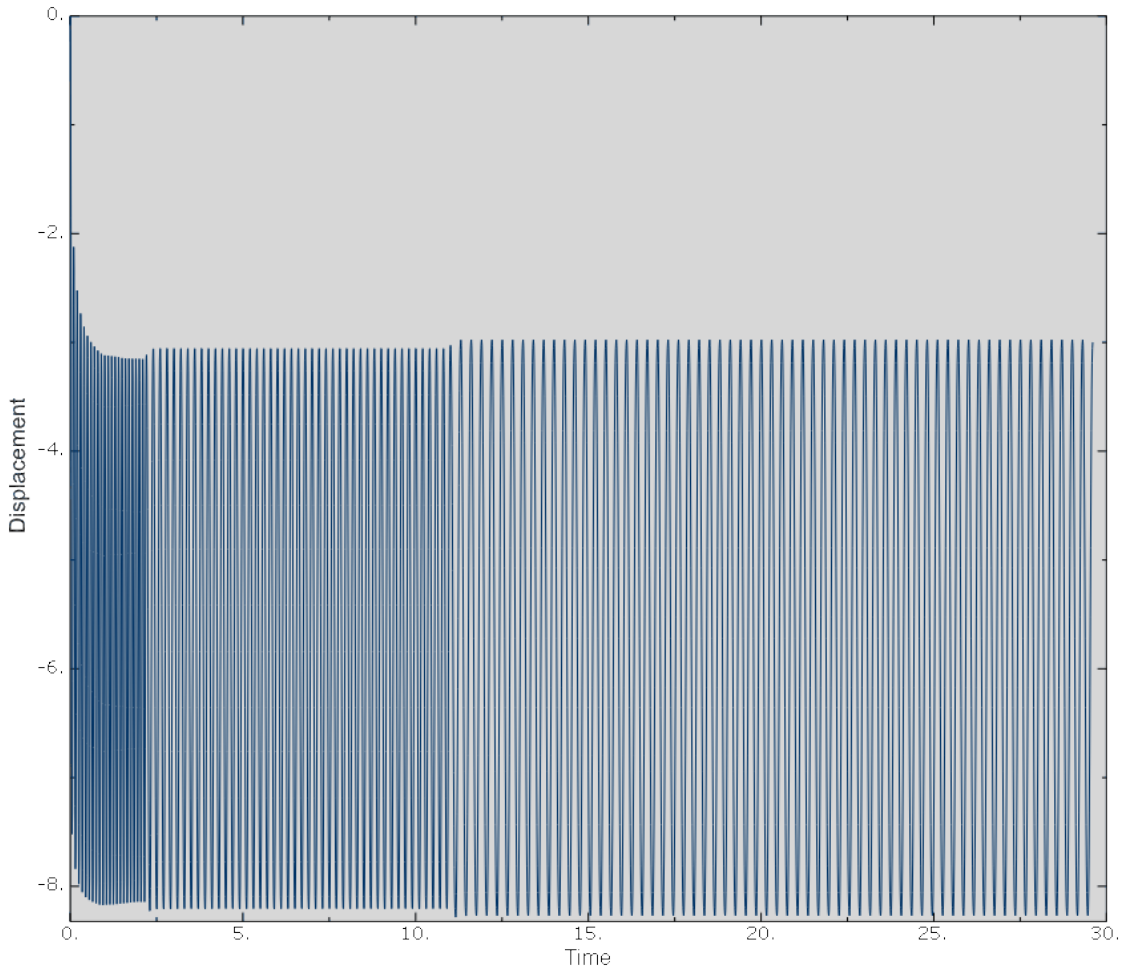

Figure 4.9: Deformation Profile with DP Base

times were 2.63 and 3.91 $hours$ as indicated in Table 4.13 and 4.14.

It can be seen that for both the base elastic case and the base DP case, the respective peak displacements do not change after 67 loading cycles. Also, for both base-type cases, the maximum (or final) value of peak displacement is essentially the same. From Table 4.14, it is clear that whatever the loading type (number of cycles or application of rest period), the peak displacements vary by about 1.6 % only for the elastic base case, and about 3 % for the DP base case. However, as indicated in Table 4.13, the cases run with 128 cycles and no rest period require a computational time (0.14 and 0.20 $hours$ for elastic base and DP base case, respectively) which is significantly less than the other loading type cases. Hence, for subsequent analyses, it was decided to adopt

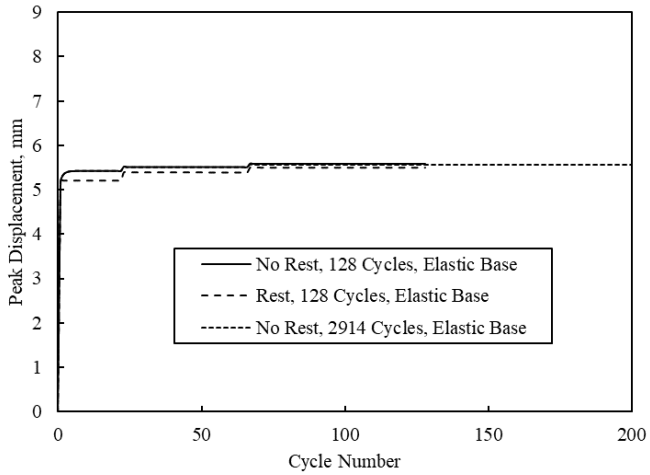

Figure 4.10: Rest Period and Load Cycle Number Analysis for Elastic Base

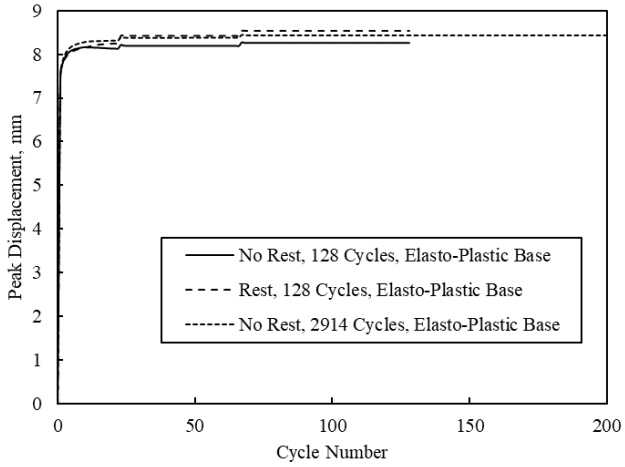

Figure 4.11: Rest Period and Load Cycle Number Analysis for Elasto-Plastic Base

loading pattern as 128 loading cycles with no rest period.

4.1.5 Lane 4 (North) Analysis for Establishing Necessity of Base Yielding

An analysis of Lane 4 (North) was conducted for identifying the peak displacements. This analysis was conducted for both the base elastic case, and the base DP case in order to compare the peak displacement at the top of asphalt surface under the tire load. The loading was 128 cycles with no rest period (NRP). In either case, the asphalt layer was modeled as nonlinear viscoelastic (NLVE) and visoplastic with hardening-relaxation and (VP-HR). Furthermore, the subbase and the subgrade were both modeled as linear elastic isotropic. The structure was subjected to 128 loading cycles with no rest periods. The total loading time was, thus, 29.6 s.

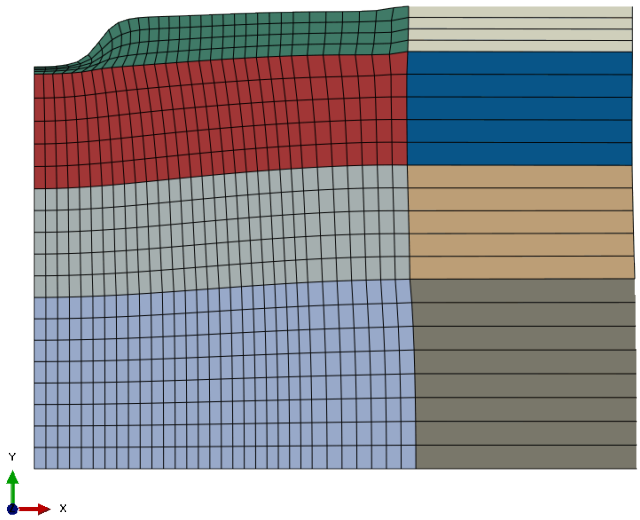

Figure 4.12: Deformation Profile with Elastic Base

Lane 4, as indicated in section above, consists of an asphalt concrete layer of HMA with binder PG 64-22 grade.

Figure 4.12 indicates the deformed section for the elastic base case and Figure 4.13 indicates the deformed section for the DP base case at the end of the loading period. The ABAQUS viewport

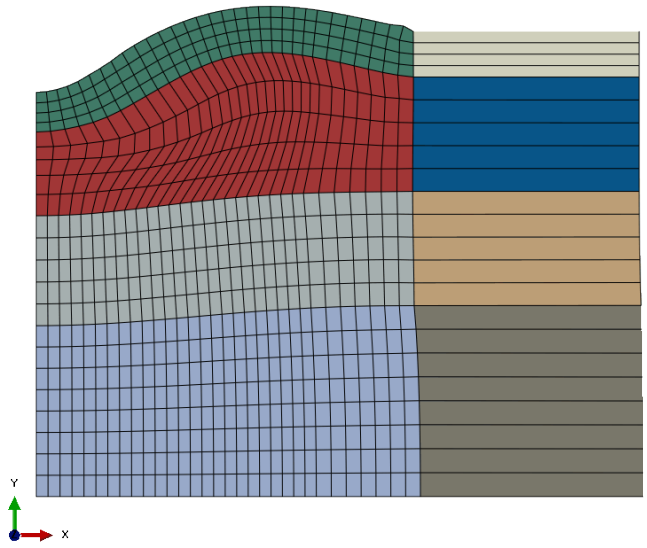

Figure 4.13: Deformation Profile with DP Base

deformation scale factors are 511.879 and 53.35 for the elastic base and DP base cases, respectively.

Figure 4.14 contains plots of peak displacement versus load cycle number with linear elastic isotropic base and elasto-plastic (DP) base. In the figure, "RP" indicates rest period and "NRP" indicates no rest period. The last peak displacement was about 5.6 mm for the elastic case ("E Base") and about 8.3 mm for the DP case ("E-P Base"). The NAPMRC field rutting data displacements are also plotted. Another case of PANDA-AP parameters obtained from University of Kansas, Lawrence research group was simulated with both base linear elastic isotropic and base elasto-plastic (DP) cases. In general, as compared to the elastic base case, the peak displacements for the final loading cycles of DP base case were about 48% greater. Even though the displacements did not closely match the actual lane rutting of 23.2 mm at NAPMRC at 124 cycles, it is clearly observed that using the elasto-plastic (DP) model for modeling the base layer results in a significantly better estimation of the actual rutting at high loading cycles.

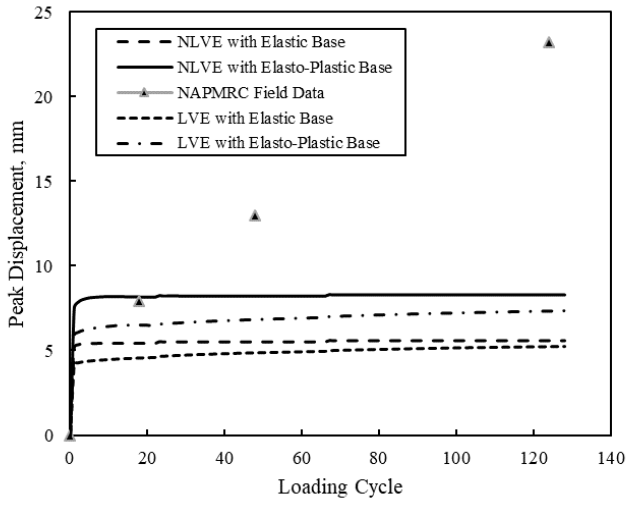

Figure 4.14: Peak Displacement Plots - Lane 4N

4.1.6 Lane 3 (North) Analysis for Establishing Necessity of Base Yielding

An analysis of Lane 3 (North) was conducted for identifying the peak displacements. This analysis was conducted for both, base elastic case, and base DP case in order to compare the peak displacement at the top of asphalt surface under the tire load. The loading was 128 cycles with no rest period (NRP). In either case, the asphalt layer was modeled as nonlinear viscoelastic (NLVE) and visoplastic with hardening-relaxation and (VP-HR). Furthermore, the subbase and the subgrade were both modeled as linear elastic isotropic. The structure was subjected to 128 loading cycles with no rest periods. The total loading time was thus, 29.6 s.

Lane 3 consists of an asphalt concrete layer of HMA with binder PG 76-22 grade. Figure 4.15 contains plots of peak displacement versus load cycle number with linear elastic isotropic base and elasto-plastic (DP) base. In the figure, "RP" indicates rest period and "NRP" indicates no rest period. The last peak displacement was about 4.8 mm for the elastic case ("E Base") and about 6.8 mm for the DP case ("E-P Base"). The NAPMRC field rutting data displacements are also plotted. In general, as compared to the elastic base case, the peak displacements for the final

loading cycles of DP base case were about 42% greater. Even though the displacements could not match the actual lane rutting of 10.8 mm at NAPMRC at 118 cycles, it is clearly seen that using the elasto-plastic (DP) model for modeling the base layer gives a better estimation of the actual rutting at high loading cycles.

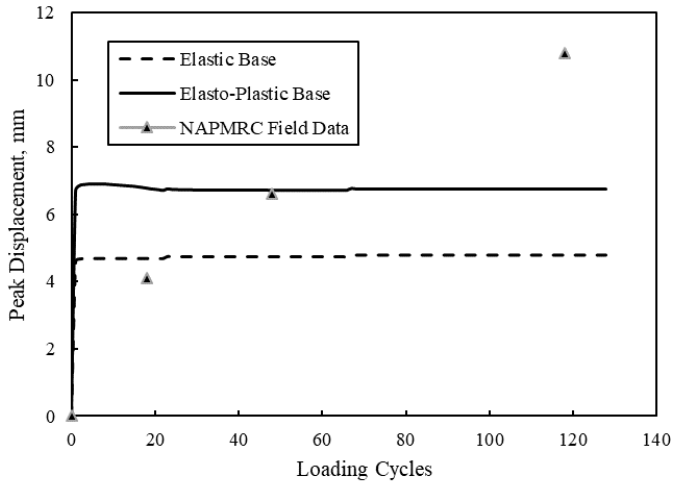

Figure 4.15: Peak Displacement Plots - Lane 3N

5. VALIDATION OF STRUCTURAL MODEL

This section details the experimental study conducted to validate the model proposed by using it in boundary value problems. Firstly, the finite element model is described in detail. Secondly, the material properties are detailed. Thirdly, the results are reported in terms of strains as well as deformations.

5.1 Validation With Inelasticity Only in Base Layer

In this section, the model proposed in Section 3.4 is validated on the NAPMRC pavement sections, assigning linear elastic material property to all of the structural layers except the base. The proposed Drucker-Prager modified combined hardening model with progressively reducing yield surface is used in the base layer. Findings are then reported on the critical location: *base layer bottom under the center of tire load*. The model is described in the following sections.

5.1.1 Pavement Structure and Materials

The pavement structural sections that were tested in this study were newly constructed four lanes at the NAPMRC facility. The pavement design was in accordance with the FAARFIELD (FAA 2009) computer program. Figure 5.1 indicates the general pavement cross-section for hot mix asphalt (HMA) as well as warm mix asphalt (WMA).

The pavement structure was composed of a bottom layer of sandy subgrade having a CBR value of 15. This was overlaid with a 12 $inch$ thick subbase layer of FAA standard specification item P-154. P-154 is a subbase course composed of granular materials. Over the subbase was laid a 12 $inch$ thick base layer of FAA standard specification item P-209. P-209 is a base course composed of crushed aggregates. The top layer was a 5 $inch$ pavement course of FAA standard specification item P-401. P-401 is a pavement course composed of mineral aggregate and bituminous material mixed in a central mixing plant. The pavement course was either HMA or WMA in accordance with the experimental design indicated in sections below.

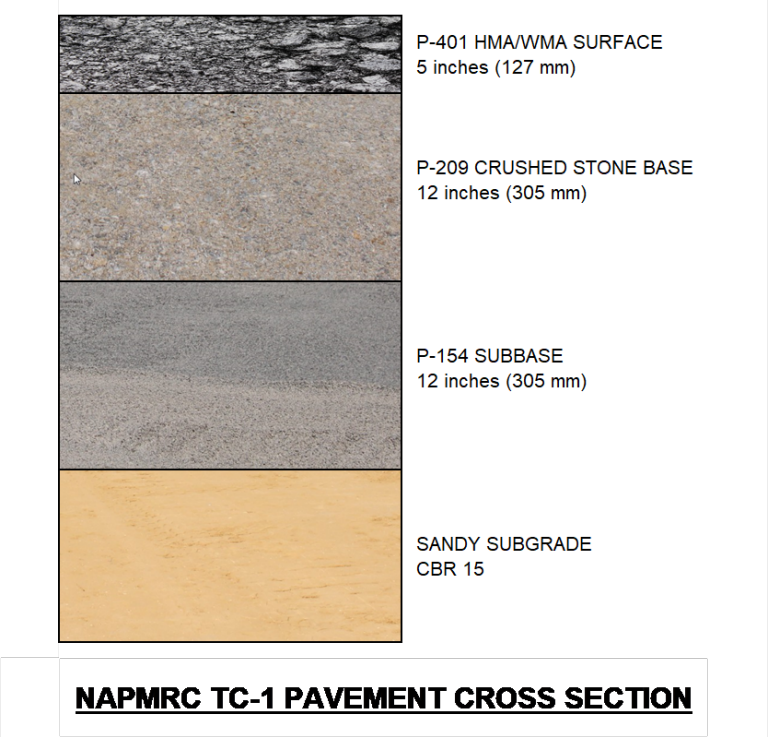

Figure 5.1: NAPMRC TC-1 Pavement Structure for Model Validation

5.1.2 Specific Design Simulation

The NAPMRC Test Cycle-1 (TC-1) test sections are described in Section 4.1.1.3 and indicated in Figure 4.2. Material parameters of outdoor Lane 1 were used for this analysis. Lane 1 consisted of a WMA pavement course having P-401 specifications and a PG 76-22 graded asphalt binder.

5.1.3 Material Parameters

This section describes the material parameters for asphalt, base, subbase, and subgrade layers. The analysis parameters and software used are also described.

5.1.3.1 Identification of Asphalt Layer Material Properties

The pavement section modeled was composed of an asphalt layer of FAA P-401 specification. The asphalt mix was 19 mm mix with all coarse aggregates procured from Springhouse, Springhouse, PA. The fine aggregates (Natural Sand) were procured from Hanson, Berlin, NJ. The asphalt binder content was 6%. Evotherm Type M was added for constructing the WMA layers.

The percentage by weight of binder added to PG 76-22 binder was 0.5%. In general, the warm mix asphalt (WMA) layer was modeled as linear elastic. The Young's modulus and Poisson's ratio were 1379.00 MPa and 0.35, respectively.

5.1.3.2 Identification of Base, Subbase, and Subgrade Layer Material Properties

The granular base and subbase materials used in the pavement sections were specified as P-209 and P-154, respectively. The NAPMRC P-209 base is a crushed aggregate base course, and the NAPMRC P-154 subbase is a course manufactured screening according to FAA Advisory Circular Number 150/5370-10F.

The base layer was modeled as linear elastic isotropic using the Drucker-Prager model (DP) (without CAP) or with the proposed Drucker-Prager modified combined hardening model with progressively reducing yield surface; depending on the type of analysis that was being conducted. The subbase layer was modeled as linear elastic isotropic. The subgrade layer was, in every case, modeled as linear elastic isotropic.

The linear elastic isotropic properties consisted of a Young's modulus of 165.47 MPa and a Poisson's ratio of 0.35. The subbase was modeled as linear elastic isotropic with Young's modulus of 150 MPa and a Poisson's ratio of 0.38; while the subgrade was modeled as linear elastic isotropic with Young's modulus of 40 MPa and a Poisson's ratio of 0.40.

The material angle of friction was 40°, the flow stress ratio was 1, and the dilation angle was 40°. Based on available material properties in literature, a hardening function was used in which the yield stress depends only on the plastic strain. In this case, a plot of uniaxial compression yield stress versus uniaxial compression plastic strain was used and is shown in Figure 5.2.

5.1.4 Finite Element Analysis

This section presents the two-dimensional (2D) finite element (FE) study that was conducted in order to simulate the rutting and strain profile of the eight pavement sections during the NAPMRC field tests. The geometry of the FE model, which includes the mesh and the loading scheme is described. This is followed by a description of the material properties. The finite element analysis

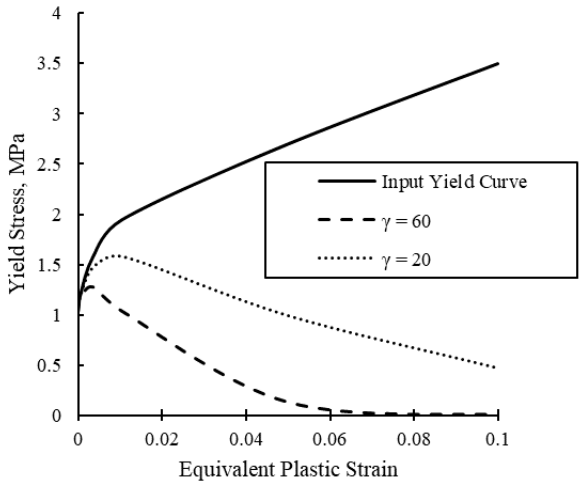

Figure 5.2: Input Yield Function

was conducted using the commercially available FE software ABAQUS. The version used was 6.14.2.

5.1.4.1 Geometry of the FE Model

The pavement section consists of a 2D plane strain half-section of dimensions 1600.0 × 1220.0 mm in width and height, respectively. The 2D FE mesh is shown in Figure 5.3. In order to simulate plane strain conditions, two boundary conditions were imposed on the model. Firstly, the vertical edge at the middle dividing the pavement section into two equal halves was constrained (fixed) against movement in the horizontally. Secondly, the bottom horizontal edge was constrained against movement vertically. The direction "X" indicated in the figure was named the positive 1-1 direction. Hence, the components of stress (S11), strain (E11), and displacement (U1) in this direction are named accordingly in the ABAQUS analysis output and results. Similarly, the "Y" direction was named positive 2-2. Hence, the direction positive 3-3 direction is the one perpendicular to the plane of the paper.

Two element types were used in this analysis. Figure 5.4 shows the mesh with the element types. The element type used for the central portion of the mesh (shaded white) was the ABAQUS

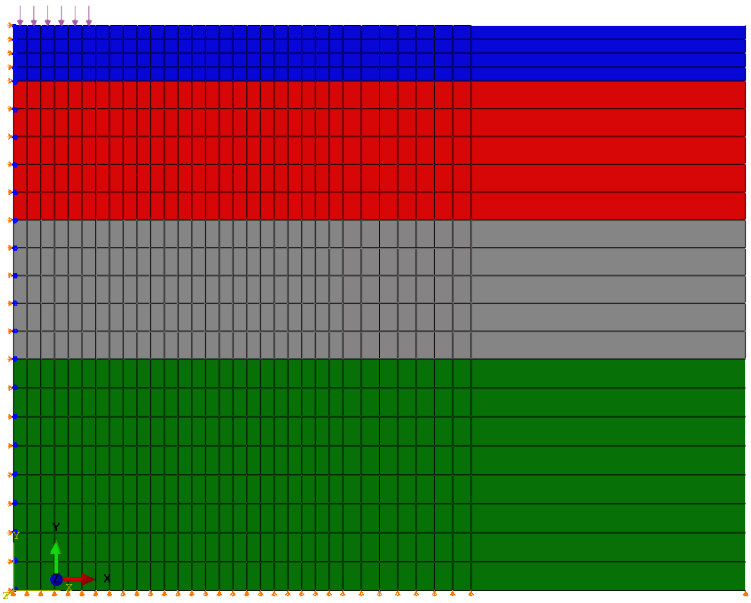

Figure 5.3: Two-dimensional FE Mesh

continuum plane strain four-node element with reduced integration (CPE4R). The element type used for the portions at the extreme right of the mesh (shaded green) was the ABAQUS continuum infinite plane strain four-node element (CINPE4). The infinite elements were used primarily for computational simplicity and to represent realistic boundary conditions.

The various sections used in the mesh are indicated in Figure 5.3 above. A maximum element aspect ratio of 1.6 was used. Element sizes used under the loads was $30 \times 30\ mm^2$ in asphalt section of the materials, shaded green. Maximum element size used, other than the infinite elements, was in the subgrade portion in the area farthest from loading and this was $40.0 \times 62.5\ mm^2$.

5.1.4.2 Loading Assumptions

The wheel load is of the type pressure, and is applied symmetrically at the middle on the top of pavement section. For calculation purpose, the tire imprint was assumed to be rectangular with the transverse dimension as 360 mm. In this study, four different tire loads were applied to the pavement, each with two different tire pressures. Hence, computationally in a 2D analysis for a constant tire pressure, an increase in load translates into an equivalent increase in the loading

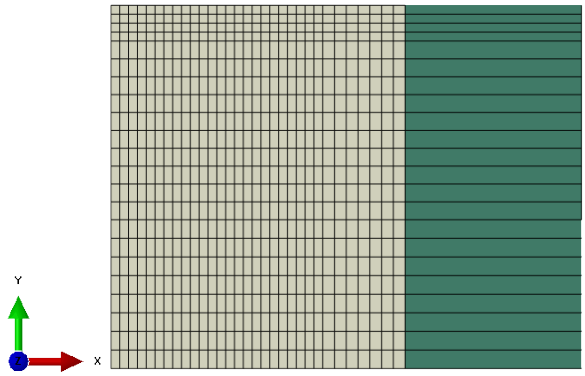

Figure 5.4: Element Types

application time of each cycle. This loading time is the time the tire takes to traverse the distance equal to the longitudinal dimension of the tire imprint.

The load was applied in cyclic manner. The loading time of each cycle was calculated as the time the tire takes to traverse the longitudinal tire imprint dimension with a speed of 3.0 mph.

Frictional and tangential effects of loading arising out of the wheel contact with asphalt surface were neglected. The loading was assumed to be applied on an infinite stripe bar along the length of the pavement at the center for a width of 360 mm. Hence, the assumed width (transverse to path of loading) of the tire imprint (or loading area) was 360 mm. From this, the length (in the longitudinal direction) of the tire imprint was calculated from two known quantities during testing: the tire load (20,000, 30,000, 40,000, or 61,300 pounds, depending on response/traffic tests) and tire pressure (254/210 psi for North/South lanes). Once this length was known, the duration of the load impulse was calculated by dividing the length by the speed of the tire.

In this study, since only Lane 1 was analyzed, a tire pressure of 254 psi (or 1.75 MPa) was desired. However, since the input yield curve was from the literature and not actually representing

the FAA P-209 base material, the applied load did not induce elasto-plastic behavior in the base material. Hence, various trials were conducted. From the trials and previous experience with material behaviors, load magnitude selected was 4.00 MPa. It may be noted that this magnitude is greater than a actual tire pressure. Also, for simplicity purpose, the loading time was kept as 0.1 s.

The total number of passes were 2914 cycles of loading with no rest periods. The number of passes closed resembled those in the NAPMRC experiment. Initial trial showed that plastic strain did not evolve beyond first 50 cycles. Hence, for computational efficiency, it was decided to conduct the simulations up to 296 cycles. The rest periods were neglected by proving that in the present material formulation, there is no significant difference in the surface displacement under the load center point.

5.1.4.3 Wander

As described in Section 4.1.1.3, tire wander was applied in the NAPMRC experiment. However, all the simulations and validations conducted in this study were conducted without the application of any tire wander. Consequently, it is assumed that all tire load is applied in the same wheel track from start to the end of the analysis.

5.1.5 Results for Friction Angle 30

The results of the analysis conducted using the elasto-plastic model in base layer and keeping all the other layers as linear elastic are presented in this section. First, results are presented for material with friction angle $\phi = 30°$. Second, rutting is compared in between two friction angle values for three γ values of 0, 20, and 60.

5.1.5.1 Deformation Profiles

The general deformation profiles were as indicated in Figure 5.5.

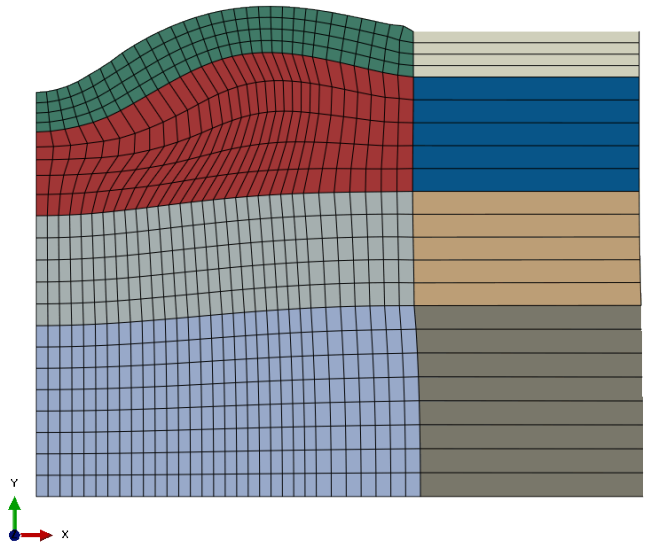

Figure 5.5: Deformation Profile - Conventional DP Model

5.1.5.2 Rutting and Surface Profile at End of Loading Cycles

The rutting and surface profiles were computed at the end of loading cycles for γ values of 0, 20, and 60. When $\gamma = 0$, there is no change in the original input hardening behavior of the base layer material. Values of 20 and 60 represent higher level of base softening. Figures 5.6, 5.7, and 5.8 indicate the variation in rutting of the pavement cross-section from the center (under the center of tire imprint) up to a distance of 1000 mm for the three values of γ. Since the asphalt layer was elastic, no permanent deformation occurred and as expected, total pavement rutting and base layer rutting were equal.

Since the asphalt layer was elastic, no permanent deformation occurred and as expected, total pavement rutting and base layer rutting were equal. The effect of $\gamma - value$ was illustrated in Figure 5.9 for base layer rutting and Figure 5.10 for total rutting.

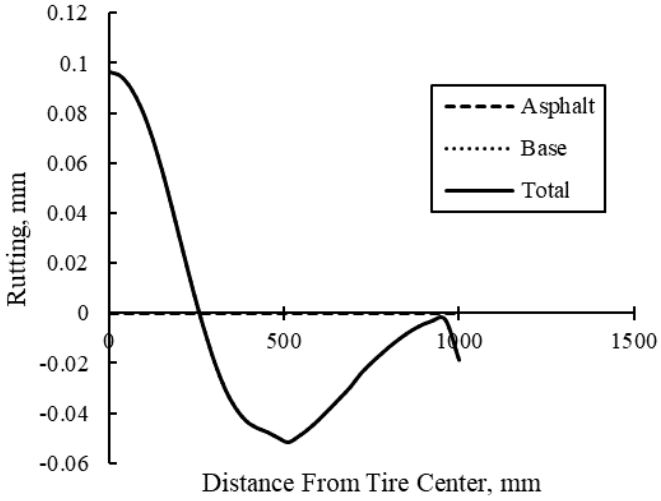

Figure 5.6: Rutting Distribution Across Pavement Cross-section, $\gamma = 0$

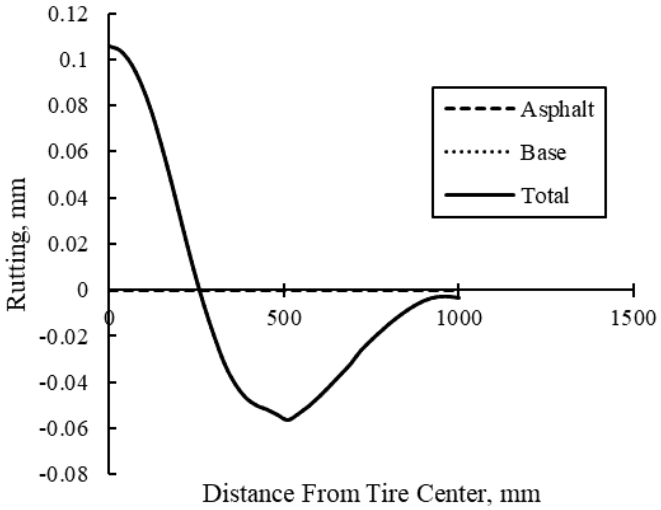

Figure 5.7: Rutting Distribution Across Pavement Cross-section, $\gamma = 20$

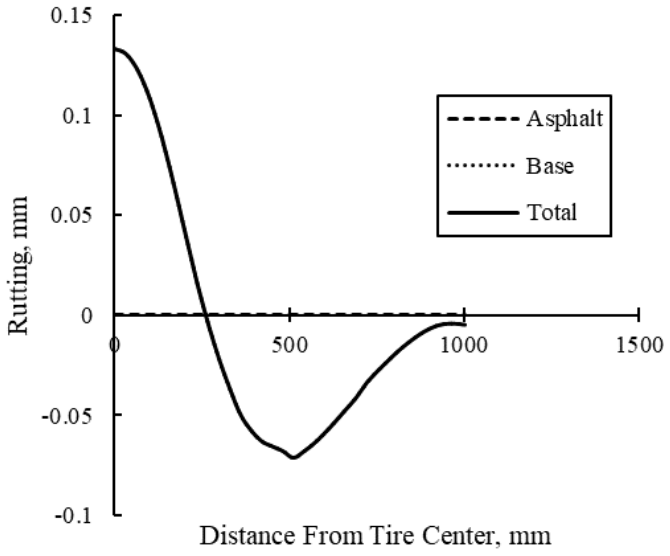

Figure 5.8: Rutting Distribution Across Pavement Cross-section, $\gamma = 60$

5.1.6 Effect of $\gamma - value$ on Variation of Rutting with Load Cycles

The variation of rutting with loading cycles was studied. Two base layers having $\phi - value$ of 20° and 30° were analyzed. Since the base rutting and total rutting values are the same for a layered pavement structure in which all other layers are linear elastic, only the total rutting plots are indicated. Figure 5.11 indicates rutting curve for the case with base layer $\phi = 20^\circ$ and Figure 5.12 indicates rutting curve for case with base layer $\phi = 30^\circ$.

For each friction angle, ϕ, total rutting curves for $\gamma = 0, 20, 60$ cases were plotted. Table 5.1 indicates the percentage increase in rutting due to inclusion of a progressively evolving yield surface ($\gamma - value$) in the base layer DP model.

An increasing in rutting of 49.95% was observed with $\gamma = 60$ in case of pavement section having friction angle, $\phi = 20^\circ$; while 38.4% increase was observed for the same $\gamma - value$ for the case of $\phi = 30^\circ$. The results establish the need for a continuously evolving yield surface for properly capturing rutting in a layered pavement system.

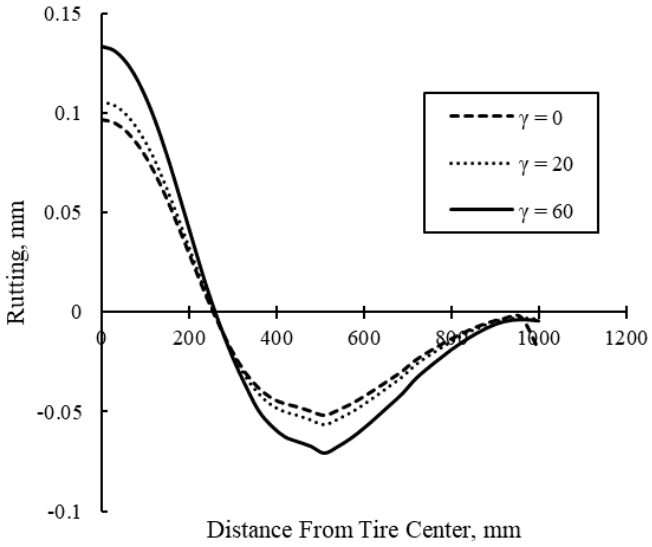

Figure 5.9: Effect of $\gamma - value$ on Base Layer Rutting ($\phi = 30°$)

Table 5.1: Percentage Increase in Rutting due to Effect of $\gamma - value$

Friction Angle	$\phi = 20°$		$\phi = 30°$	
Gamma (γ)	Total Rutting, mm	% Increase	Total Rutting, mm	% Increase
$\gamma = 0$	0.26	—	0.10	—
$\gamma = 20$	0.28	9.82	0.11	9.80
$\gamma = 60$	0.39	49.95	0.13	38.40

5.1.7 Effect of Material Friction Angle on Variation of Rutting with Load Cycles

The effect of friction angle on rutting for each $\gamma - value$ was studied to verify the sensitivity of the model to material friction angle. As mentioned elsewhere in this section, two base layer material friction angle were used in this study. It was observed that lower friction angle results in a higher rutting in the base; and hence higher total rutting. Figures 5.13, 5.14, and 5.15 indicate respective rutting variation for $\gamma = 0, 20, 60$.

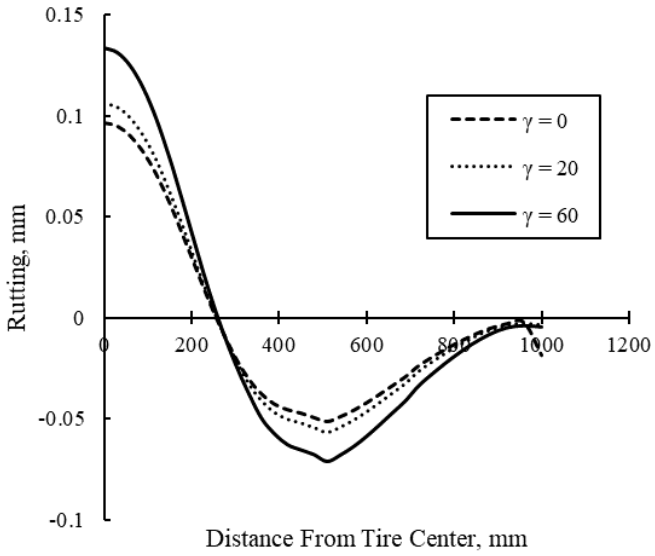

Figure 5.10: Effect of $\gamma - value$ on Total Rutting ($\phi = 30°$)

5.1.8 Discussion

The inclusion of $\gamma - factor$ in the DP model, which results in a progressively reducing yield surface leads to a higher rutting prediction for a layered pavement system as compared to using classical DP model. The increased rutting is a result of an increase in the equivalent plastic strain as well as vertical plastic strain in the material.

5.2 Validation With NAPMRC Experiment

In this section, the model proposed in Section 3.4 is validated on the NAPMRC pavement sections, assigning linear elastic material property to all of the structural section, except the base and asphalt concrete. The asphalt concrete is modeled using user subroutine PANDA. The proposed Drucker-Prager modified combined hardening model with progressively reducing yield surface is used in the base layer. The findings are then reported on critical location: *the base layer bottom under the center of tire load*. The model is described in the following sections.

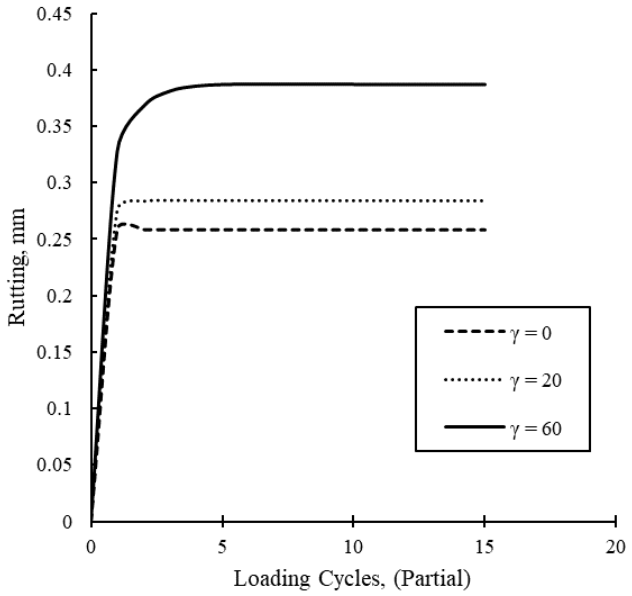

Figure 5.11: Effect of $\gamma - value$ on Total Rutting Variation ($\phi = 20°$)

5.2.1 Pavement Structure and Materials

The pavement structural sections that were tested in this study were newly constructed four lanes at the NAPMRC facility. The pavement design was in accordance with the FAARFIELD (FAA 2009) computer program. Figure 5.1 indicates the general pavement cross-section for hot mix asphalt (HMA) as well as warm mix asphalt (WMA).

The pavement structure was composed of a bottom layer of sandy subgrade having a CBR value of 15. This was overlaid with a 12 $inch$ thick subbase layer of FAA standard specification item P-154. P-154 is a subbase course composed of granular materials. Over the subbase was laid a 12 $inch$ thick base layer of FAA standard specification item P-209. P-209 is a base course composed of crushed aggregates. The top layer was a 5 $inch$ pavement course of FAA standard specification item P-401. P-401 is a pavement course composed of mineral aggregate and bituminous material mixed in a central mixing plant. The pavement course was either HMA or WMA in accordance with the experimental design indicated in sections below.

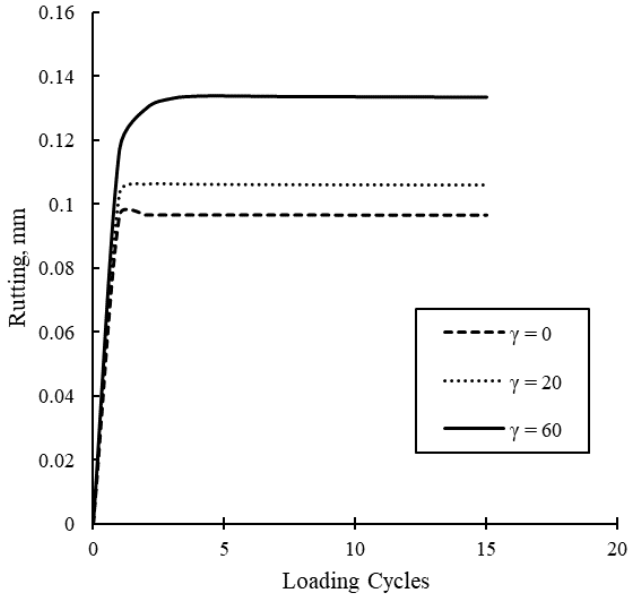

Figure 5.12: Effect of $\gamma - value$ on Total Rutting Variation ($\phi = 30°$)

5.2.2 Specific Design Simulation

The NAPMRC Test Cycle-1 (TC-1) test sections have already been described in Section 4.1.1.3 and shown in Figure 4.2. The analysis for this work was conducted using data for the outdoor Lane 1. Lane 1 consisted of a WMA pavement course having P-401 specifications. The asphalt binder used was PG 76-22.

5.2.3 Material Parameters

This section describes the material parameters for asphalt, base, subbase, and subgrade layers. The analysis parameters and software used are also described.

5.2.3.1 Identification of Asphalt Layer Material Properties

The pavement section modeled was composed of an asphalt layer of FAA P-401 specification. The asphalt mix was 19 mm mix with all coarse aggregates procured from Springhouse, Springhouse, PA. The fine aggregates (Natural Sand) were procured from Hanson, Berlin, NJ. The asphalt

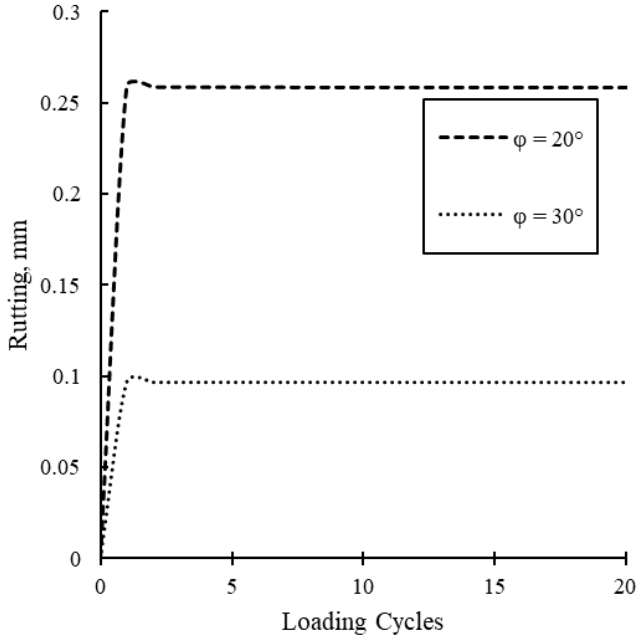

Figure 5.13: Effect of Friction Angle on Total Rutting Variation ($\gamma = 0$)

binder content was 6%. Evotherm Type M was added for constructing the WMA layers. The percentage by weight of binder added to PG 76-22 binder was 0.5%. Procedure outlined in [40] was followed to analyze the dynamic modulus and phase angle to identify the viscoelastic parameters associated with PANDA-AP. More information on characterization of linear and nonlinear viscoelastic properties can found in [41]. The general asphalt material parameters are presented in Figure 4.6 for linear viscoelastic, Figure 4.7 for non-linear viscoelastic, Figure **??** for viscoplastic, and Figure 4.11 for hardening-relaxation as applicable to Lane 1, which is WMA with PG 76-22 binder.

5.2.3.2 Identification of Base, Subbase, and Subgrade Layer Material Properties

The granular base and subbase materials used in the pavement sections were specified as P-209 and P-154, respectively. The NAPMRC P-209 base is a crushed aggregate base course, and the NAPMRC P-154 subbase is a course manufactured screening according to FAA Advisory Circular

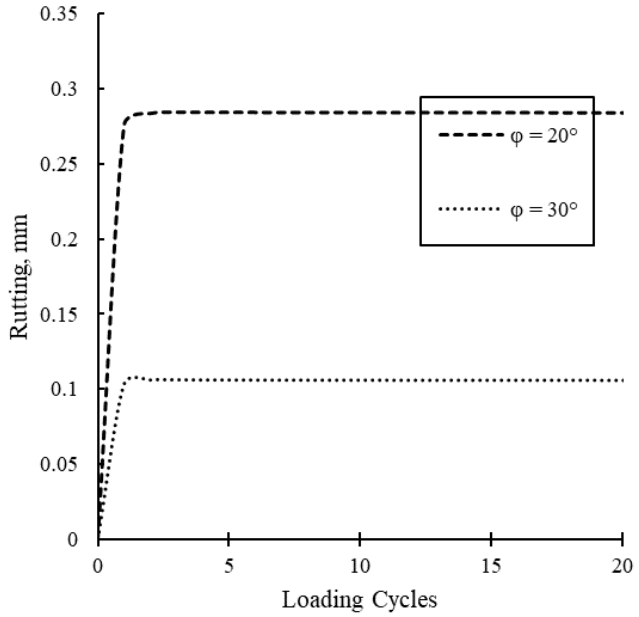

Figure 5.14: Effect of Friction Angle on Total Rutting Variation ($\gamma = 20$)

Number 150/5370-10F.

The base layer was modeled as linear elastic isotropic using the Drucker-Prager model (DP) (without CAP) or with the proposed Drucker-Prager modified combined hardening model with progressively reducing yield surface; depending on the type of analysis that was being conducted. The subbase layer was modeled as linear elastic isotropic. The subgrade layer was, in every case, modeled as linear elastic isotropic.

The linear elastic isotropic properties consisted of a Young's modulus of 165.47 MPa and a Poisson's ratio of 0.35. The subbase was modeled as linear elastic isotropic with Young's modulus of 150 MPa and a Poisson's ratio of 0.38; while the subgrade was modeled as linear elastic isotropic with Young's modulus of 40 MPa and a Poisson's ratio of 0.40.

The material angle of friction was 40°, the flow stress ratio was 1, and the dilation angle was 40°. Based on available material properties in literature, a hardening function was used in which the yield stress depends only on the plastic strain. In this case, a plot of uniaxial compression yield

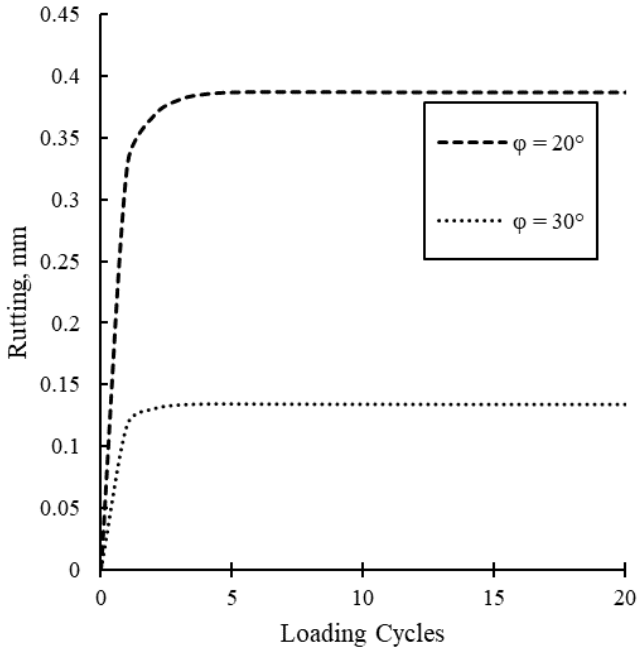

Figure 5.15: Effect of Friction Angle on Total Rutting Variation ($\gamma = 60$)

stress versus uniaxial compression plastic strain was used and is shown in Figure 3.4.

5.2.4 Finite Element Analysis

This section presents the two-dimensional (2D) finite element (FE) study that was conducted in order to simulate the rutting and strain profile of the eight pavement sections during the NAPMRC field tests. The geometry of the FE model, which includes the mesh and the loading scheme is described. This is followed by a description of the material properties. The finite element analysis was conducted using the commercially available FE software ABAQUS. The version used was 6.14.2.

5.2.4.1 Geometry of the FE Model

The pavement section consists of a 2D plane strain half-section of dimensions 1600.0 × 1220.0 mm in width and height, respectively. The 2D FE mesh is shown in Figure 5.3. In order to sim-

ulate plane strain conditions, two boundary conditions were imposed on the model. Firstly, the vertical edge at the middle dividing the pavement section into two equal halves was constrained (fixed) against movement in the horizontally. Secondly, the bottom horizontal edge was constrained against movement vertically. The direction "X" indicated in the figure was named the positive 1-1 direction. Hence, the components of stress (S11), strain (E11), and displacement (U1) in this direction are named accordingly in the ABAQUS analysis output and results. Similarly, the "Y" direction was named positive 2-2. Hence, the direction positive 3-3 direction is the one perpendicular to the plane of the paper.

Two element types were used in this analysis. Figure 5.4 shows the mesh with the element types. The element type used for the central portion of the mesh (shaded white) was the ABAQUS continuum plane strain four-node element with reduced integration (CPE4R). The element type used for the portions at the extreme right of the mesh (shaded green) was the ABAQUS continuum infinite plane strain four-node element (CINPE4). The infinite elements were used primarily for computational simplicity and to represent realistic boundary conditions.

The various sections used in the mesh are indicated in Figure 5.3. A maximum element aspect ratio of 1.6 was used. Element sizes used under the loads was 30 × 30 mm^2 in asphalt section of the materials, shaded green. Maximum element size used, other than the infinite elements, was in the subgrade portion in the area farthest from loading and this was 40.0 × 62.5 mm^2.

5.2.4.2 Loading Assumptions

The wheel load is of the type pressure, and is applied symmetrically at the middle on the top of pavement section. For calculation purpose, the tire imprint was assumed to be rectangular with the transverse dimension as 360 mm. Computationally in a 2D analysis for a constant tire pressure, an increase in load translates into an equivalent increase in the loading application time of each cycle. This loading time is the time the tire takes to traverse the distance equal to the longitudinal dimension of the tire imprint.

The load was applied in cyclic manner. The loading time of each cycle was calculated as the time the tire takes to traverse the longitudinal tire imprint dimension with a speed of 3.0 mph.

Frictional and tangential loading arising out of the wheel contact with asphalt surface were neglected. The loading was assumed to be applied on an infinite stripe bar along the length of the pavement at the center for a width of 360 mm. Hence, the assumed width (transverse to path of loading) of the tire imprint (or loading area) was 360 mm. From this, the length (in the longitudinal direction) of the tire imprint was calculated from two known quantities during testing: the tire load (20,000, 30,000, 40,000, or 61,300 pounds, depending on response/traffic tests) and tire pressure (254/210 psi for North/South lanes). Once this length was known, the duration of the load impulse was calculated by dividing the length by the speed of the tire.

In this study, since only Lane 1 was analyzed, a tire pressure of 254 psi (or 1.75 MPa) was desired. However, since the input yield curve was from the literature and not actually representing the FAA P-209 base material, the applied load did not induce elasto-plastic behavior in the base material. Hence, various trials were conducted. From the trials and previous experience with material behaviors, load magnitude selected was 4.00 MPa. It may be noted that this magnitude is greater than a actual tire pressure. Also, for simplicity purpose, the loading time was kept as 0.1 s.

The total number of passes were 2914 cycles of loading with no rest periods. The number of passes closed resembled those in the NAPMRC experiment. Initial trial showed that plastic strain did not evolve beyond first 50 cycles. Hence, for computational efficiency, it was decided to conduct the simulations up to 296 cycles. The rest periods were neglected by proving that in the present material formulation, there is no significant difference in the surface displacement under the load center point.

5.2.4.3 Wander

As described in Section 4.1.1.3, tire wander was applied in the NAPMRC experiment. However, all the simulations and validations conducted in this study were conducted without the application of any tire wander. Consequently, it is assumed that all tire load is applied in the same wheel track from start to the end of the analysis.

5.2.5 Results for Friction Angle 30

The results of the analysis conducted using the elasto-plastic model in base layer and viscoplastic with hardening-relaxation in asphalt layer are indicated in this section. First, results are presented for material with friction angle $\phi = 30°$. Second, rutting is compared in between two friction angle values for three γ values of 0, 20, and 60.

5.2.5.1 Rutting and Surface Profile at End of Loading Cycles

The rutting and surface profiles were computed at the end of loading cycles for γ values of 0, 20, and 60. When $\gamma = 0$, there is no change in the original input hardening behavior of the base layer material. Values of 20 and 60 represent higher level of base softening. Figures 5.16, 5.17, and 5.18 indicate the variation in rutting of the pavement cross-section from the center (under the center of tire imprint) up to a distance of 1000 mm for the three values of γ.

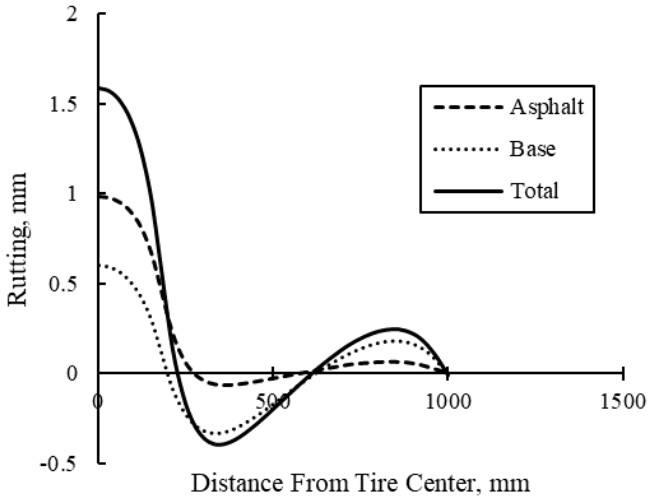

Figure 5.16: Rutting Distribution Across Pavement Cross-section, $\gamma = 0$

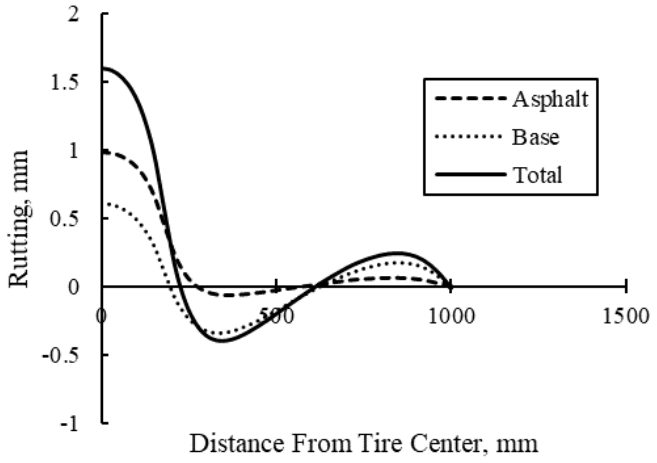

Figure 5.17: Rutting Distribution Across Pavement Cross-section, $\gamma = 20$

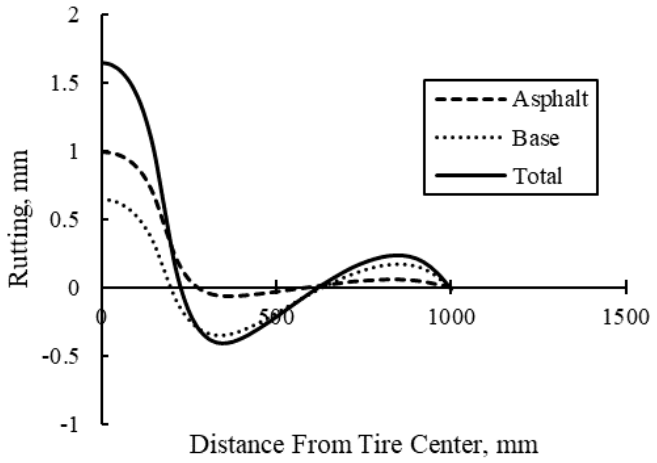

Figure 5.18: Rutting Distribution Across Pavement Cross-section, $\gamma = 60$

The effect of $\gamma - value$ was illustrated in Figure 5.19 for base layer rutting and Figure 5.20 for total rutting.

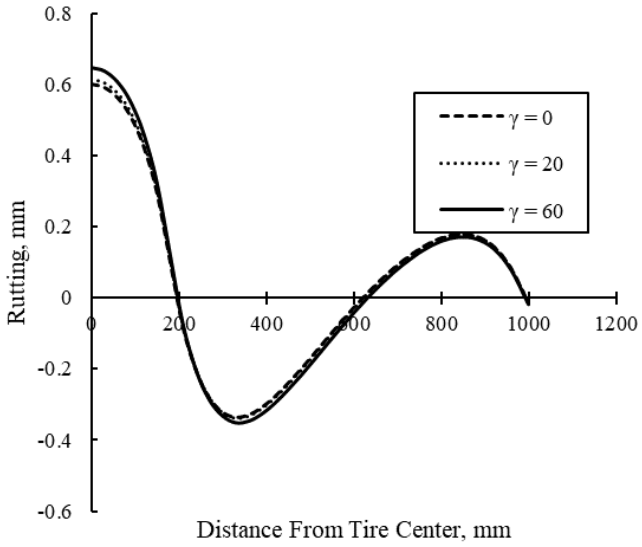

Figure 5.19: Effect of $\gamma - value$ on Base Layer Rutting ($\phi = 30°$)

5.2.6 Effect of $\gamma - value$ on Variation of Total Rutting with Load Cycles

The variation of total rutting with loading cycles was studied. Pavement sections with two base layers having $\phi - value$ of $30°$ and $40°$ were analyzed. Figure 5.21 indicates total rutting curve for the case with base layer $\phi = 30°$ and Figure 5.22 indicates total rutting curve for case with base layer $\phi = 40°$.

For each friction angle, ϕ, total rutting curves for $\gamma = 0, 20, 60$ cases were plotted. Table 5.2 indicates the percentage increase in rutting due to inclusion of a progressively evolving yield surface ($\gamma - value$) in the base layer DP model.

An increasing in rutting of 3.4% was observed with $\gamma = 60$ in case of pavement section having friction angle, $\phi = 30°$; while 0.24% increase was observed for the same $\gamma - value$ for the case of $\phi = 40°$. The results establish the need for a continuously evolving yield surface for properly capturing rutting in a layered pavement system.

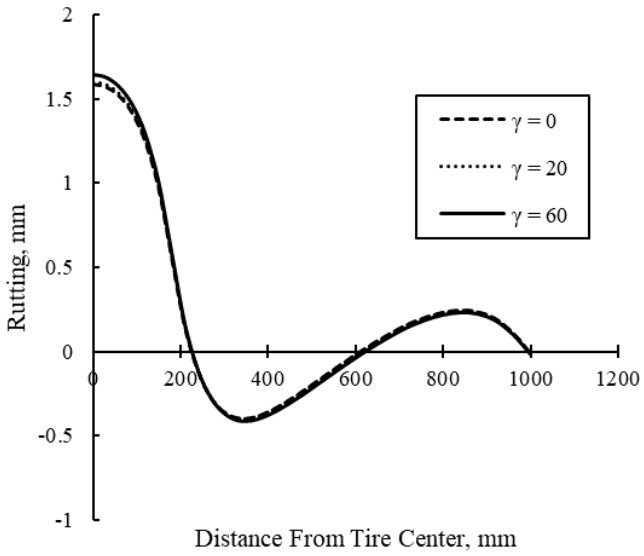

Figure 5.20: Effect of $\gamma - value$ on Total Rutting ($\phi = 30°$)

Table 5.2: Percentage Increase in Total Rutting due to Effect of $\gamma - value$

Friction Angle	$\phi = 30°$		$\phi = 40°$	
Gamma (γ)	Total Rutting, mm	% Increase	Total Rutting, mm	% Increase
$\gamma = 0$	1.59	—	1.48	—
$\gamma = 20$	1.60	0.88	1.48	0.07
$\gamma = 60$	1.64	3.40	1.48	0.24

5.2.7 Effect of $\gamma - value$ on Variation of Base Rutting with Load Cycles

The variation of rutting with loading cycles was studied. The two base layers having $\phi - value$ of $30°$ and $40°$ were analyzed. Figure 5.23 indicates base rutting curve for the case with base layer $\phi = 30°$ and Figure 5.24 indicates base rutting curve for case with base layer $\phi = 40°$.

For each friction angle, ϕ, total rutting curves for $\gamma = 0, 20, 60$ cases were plotted. Table 5.3 indicates the percentage increase in rutting due to inclusion of a progressively evolving yield surface ($\gamma - value$) in the base layer DP model.

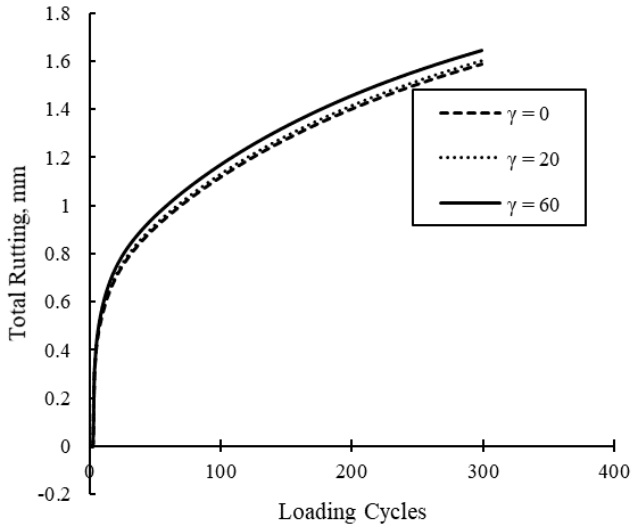

Figure 5.21: Effect of $\gamma - value$ on Total Rutting Variation ($\phi = 30°$)

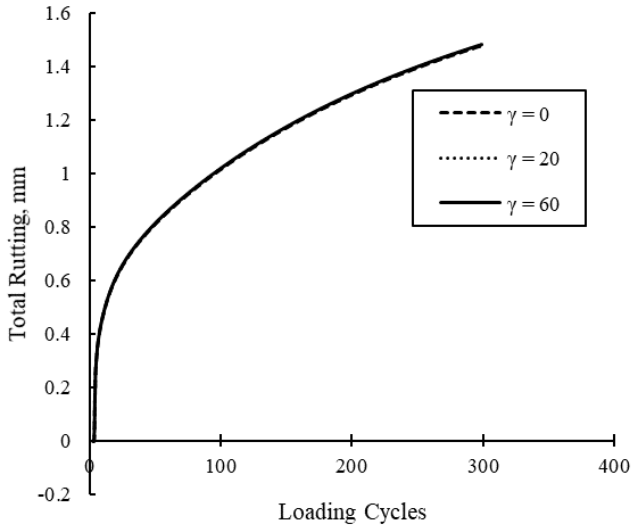

Figure 5.22: Effect of $\gamma - value$ on Total Rutting Variation ($\phi = 40°$)

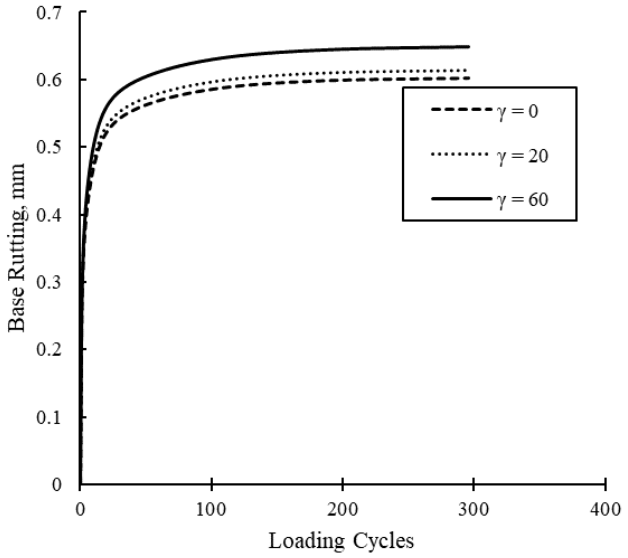

Figure 5.23: Effect of $\gamma - value$ on Base Rutting Variation ($\phi = 30°$)

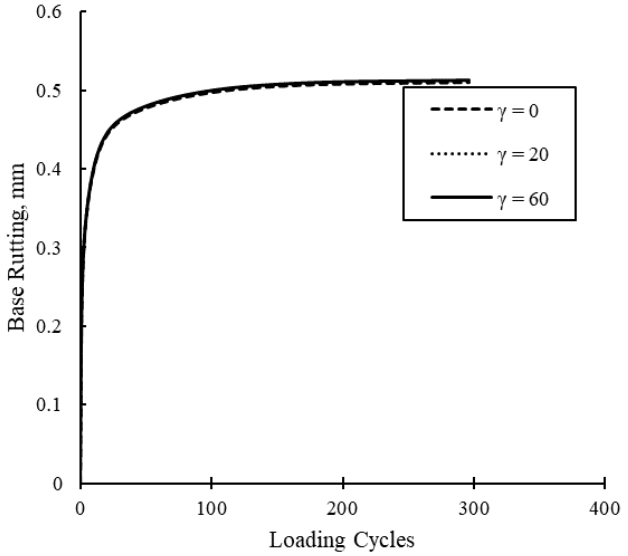

Figure 5.24: Effect of $\gamma - value$ on Base Rutting Variation ($\phi = 40°$)

Table 5.3: Percentage Increase in Total Rutting due to Effect of $\gamma - value$

Friction Angle	$\phi = 30°$		$\phi = 40°$	
Gamma (γ)	Total Rutting, mm	% Increase	Total Rutting, mm	% Increase
$\gamma = 0$	0.60	—	0.51	—
$\gamma = 20$	0.61	2.00	0.51	0.17
$\gamma = 60$	0.65	7.70	0.51	0.58

An increasing in rutting of 7.7% was observed in the base with $\gamma = 60$ in case of pavement section having friction angle, $\phi = 30°$; while 0.58% increase was observed for the same $\gamma - value$ for the case of $\phi = 40°$. As observed above elsewhere in this section and also in case of layered pavement structure with only base layer inelastic, the results establish the need for a continuously evolving yield surface for properly capturing rutting in a layered pavement system.

5.2.8 Effect of Material Friction Angle on Variation of Total Rutting with Load Cycles

The effect of friction angle on rutting for each $\gamma - value$ was studied to verify the sensitivity of the model to material friction angle. As mentioned elsewhere in this section, two base layer material friction angle were used in this study. It was observed that lower friction angle results in a higher rutting in the base; and hence higher total rutting. Figures 5.25, 5.26, and 5.27 indicate respective total rutting variation for $\gamma = 0, 20, 60$.

5.2.9 Effect of Material Friction Angle on Variation of Base Rutting with Load Cycles

The effect of friction angle on rutting for each $\gamma - value$ was studied to verify the sensitivity of the model to material friction angle. As mentioned elsewhere in this section, two base layer material friction angle were used in this study. It was observed that lower friction angle results in a higher rutting in the base. Figures 5.28, 5.29, and 5.30 indicate respective base rutting variation for $\gamma = 0, 20, 60$.

5.2.10 Discussion

The inclusion of γ factor in the DP model, which results in a progressively reducing yield surface leads to a higher rutting prediction for a layered pavement system as compared to using

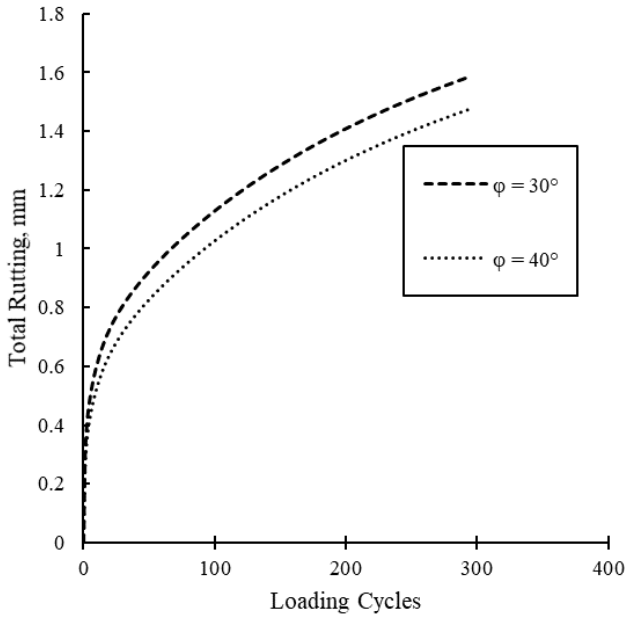

Figure 5.25: Effect of Friction Angle on Total Rutting Variation ($\gamma = 0$)

classical DP model. The increased rutting is a result of an increase in the equivalent plastic strain as well as vertical plastic strain in the material.

5.3 Case Study for Inclusion of $\gamma - factor$

As a culmination of this dissertation work, the importance of the $\gamma - factor$ was emphasized by combining the rutting results of the various pavement structural model cases analyzed in Sections 5.1 and 5.2.

The pavement structure was composed of a bottom layer of sandy subgrade having a CBR value of 15. This was overlaid with a 12 $inch$ thick subbase layer of FAA standard specification item P-154. P-154 is a subbase course composed of granular materials. Over the subbase was laid a 12 $inch$ thick base layer of FAA standard specification item P-209. P-209 is a base course composed of crushed aggregates. The top layer was a 5 $inch$ pavement course of FAA standard specification item P-401. P-401 is a pavement course composed of mineral aggregate and bituminous material

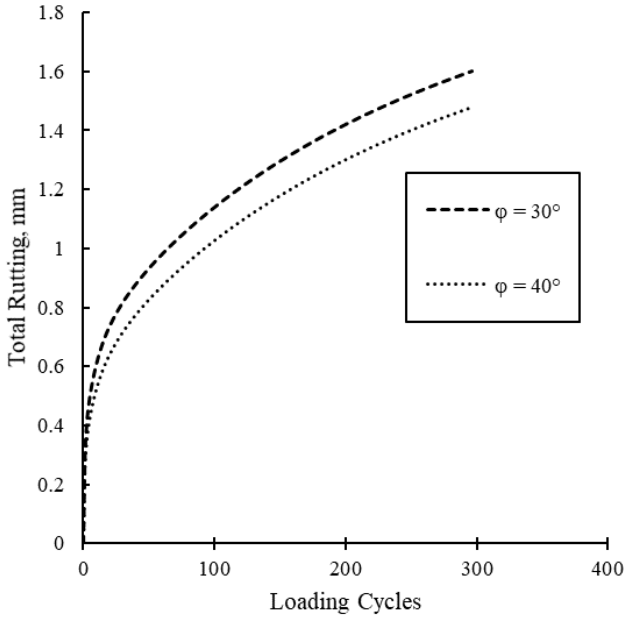

Figure 5.26: Effect of Friction Angle on Total Rutting Variation ($\gamma = 20$)

mixed in a central mixing plant. The pavement course was viscoplastic asphalt WMA layer.

The analysis was conducted for base material with friction angle, $\phi = 30°$. Five cases were analyzed based on results of 296 loading cycles. Finally, a logarithmic model was published for prediction of rutting for 10,000, 100,000, and 1000,000 cycles of loading. The five cases were:

1. **Case A**: Asphalt Elastic, Base Inelastic, $\gamma = 0$
2. **Case B**: Asphalt Elastic, Base Inelastic, $\gamma = 60$
3. **Case C**: Asphalt Viscoplastic, Base Elastic
4. **Case D**: Asphalt Viscoplastic, Base Inelastic, $\gamma = 0$
5. **Case E**: Asphalt Viscoplastic, Base Inelastic, $\gamma = 60$

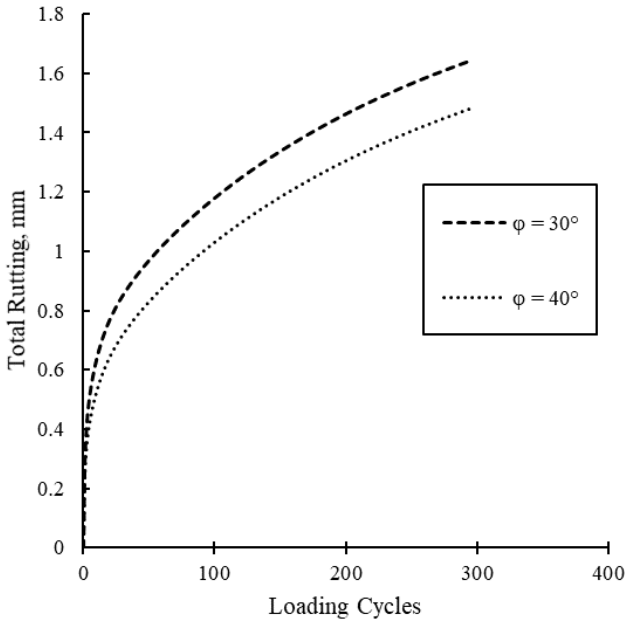

Figure 5.27: Effect of Friction Angle on Total Rutting Variation ($\gamma = 60$)

5.3.1 Rutting Comparison

Figure 5.31 indicates the rutting curves for the various cases analyzed in this section. Figure 5.32 represents the same curves, but only for 10 cycles of loading for a clearer graphical representation of the initial loading cycles.

Table 5.4 indicates percentage increase in rutting as a result of inclusion of PANDA constitutive modeling in asphalt layer as well as $\gamma - factor$ (progressively evolving yield surface) in the base layer.

It was noted that when asphalt was modeled as viscoplastic using the PANDA constitutive package and base was linear elastic, the applied tire pressure was too high for the assigned material parameters. It was observed that rutting increased ten times with the inclusion of PANDA constitutive modeling in asphalt. Furthermore, the inclusion of a progressive evolving yield surface model in the standard elasto-plastic DP model in base layer modeling resulted in about 38.4%

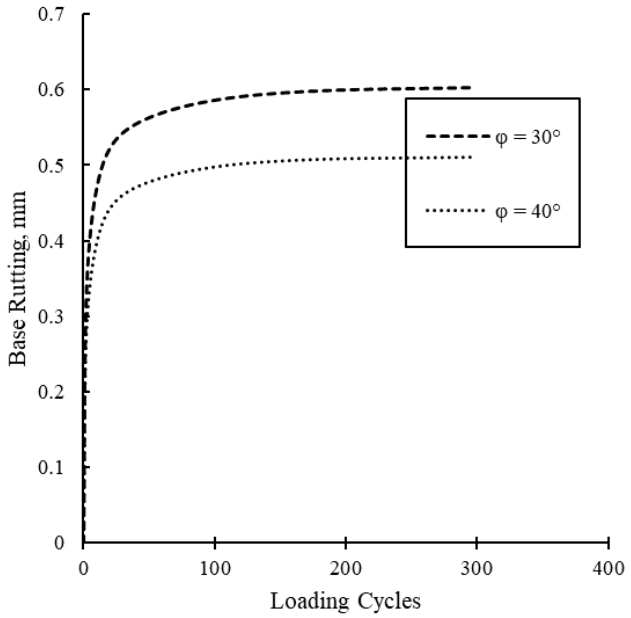

Figure 5.28: Effect of Friction Angle on Base Rutting Variation ($\gamma = 0$)

increase in rutting when only base layer was modeled as inelastic. Finally, increase in rutting due to $\gamma - factor$ in pavement structure with asphalt modeled with PANDA constitutive package was about 3.4%.

5.3.2 A Simple Logarithmic Prediction of Rutting

Figure 5.33 indicates the rutting predictions for cases analyzed with asphalt modeled as viscoplastic using PANDA and base layer with the DP model along with the progressively evolving yield surface modification in this dissertation work. A simple logarithmic model was fitted for Case D (with $\gamma = 0$) and Case E (with $\gamma = 60$) as outlined in Section 5.3.

A simple logarithmic linear model was fitted. Equation 5.1 was predicted for Case D and Equation 5.2 was predicted for Case E.

$$y = 0.0032 \times x + 0.7437 \tag{5.1}$$

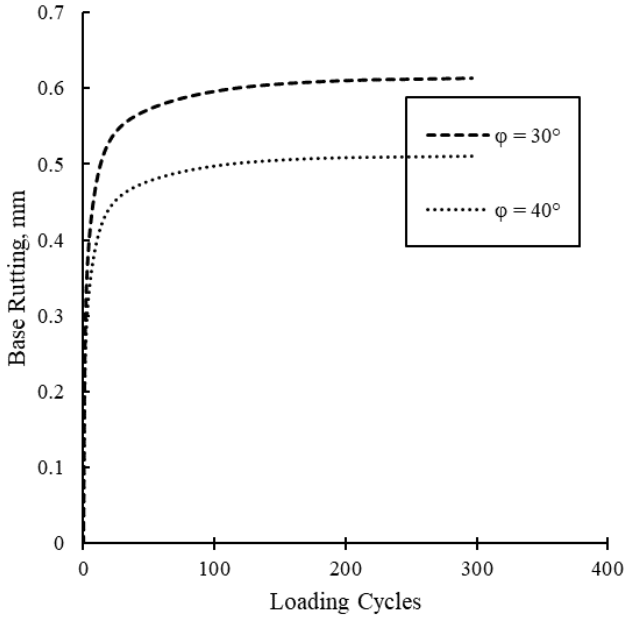

Figure 5.29: Effect of Friction Angle on Base Rutting Variation ($\gamma = 20$)

$$y = 0.0033 \times x + 0.7853 \tag{5.2}$$

Table 5.5 indicates the rutting values based on the model fit equations.

Based on this, it can be concluded that the increase in rutting due to a progressively evolving yield surface ($\gamma = 60$) is about 10 mm after 100,000 cycles of loading. It was observed that the model needs improvement in order to capture evolution of equivalent plastic strain and vertical plastic strain components.

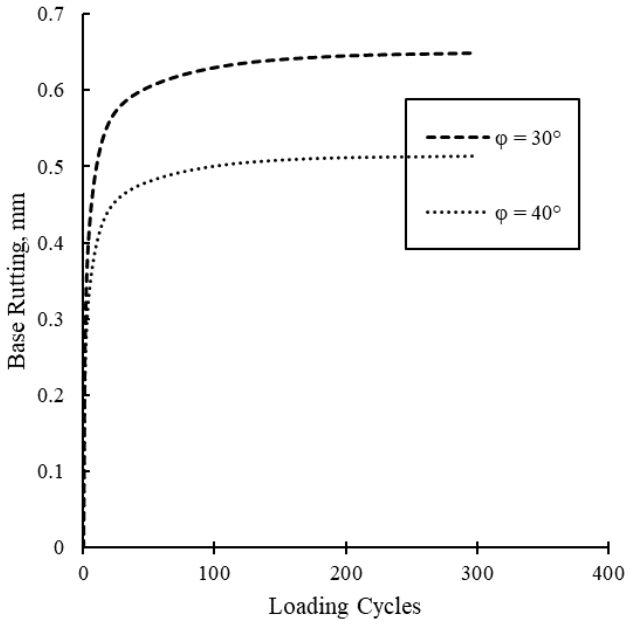

Figure 5.30: Effect of Friction Angle on Base Rutting Variation ($\gamma = 60$)

Table 5.4: Percentage Increase in Rutting Due to $\gamma - factor$ Inclusion

Pavement Structural Model	Design Code	Total Rutting, mm	% Increase from A to D (Due to PANDA)	% Increase from B to E (Due to PANDA)	% Increase from A to B (Due to $\gamma - factor$)	% Increase from D to E (Due to $\gamma - factor$)
Asphalt Elastic_Base Inelastic_$\gamma = 0$	A	0.096369	—	—	—	—
Asphalt Elastic_Base Inelastic_$\gamma = 60$	B	0.133378	—	—	38.40	—
Asphalt VP_Base Elastic	C	—	—	—	—	—
Asphalt VP_Base Inelastic_$\gamma = 0$	D	1.58853	1548.38	—	—	—
Asphalt VP_Base Inelastic_$\gamma = 60$	E	1.64256		1131.50	—	3.40

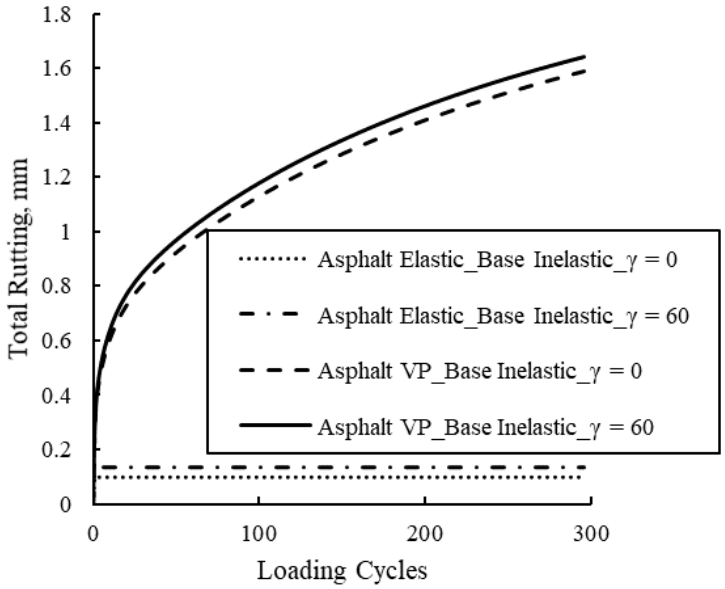

Figure 5.31: Rutting Curves for Various Pavement Structural Models, All Loading Cycles

Table 5.5: Rutting Prediction - Logarithmic

Pavement Model	Rutting (mm) for Loading Cycles		
$\gamma - value$	296	10,000	100,000
0	1.69	32.74	320.74
60	1.76	33.79	330.79

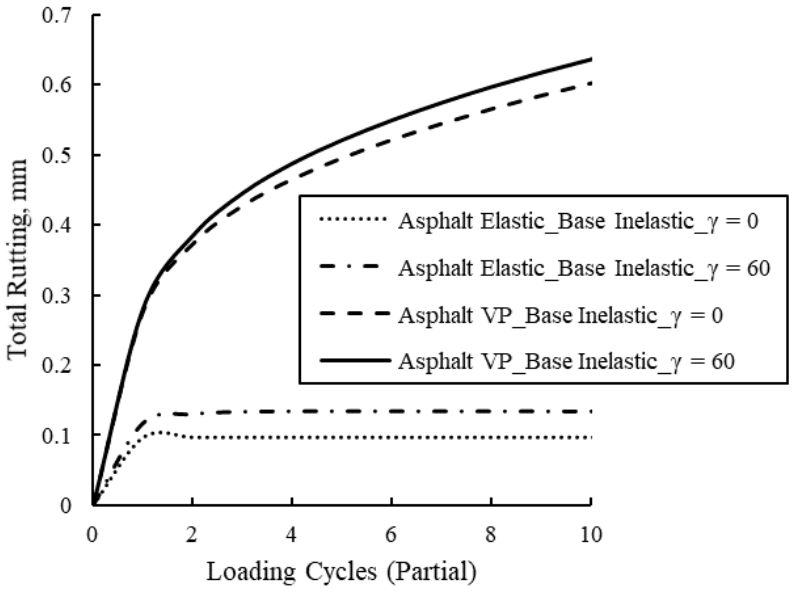

Figure 5.32: Rutting Curves for Various Pavement Structural Models, 10 (Initial) Loading Cycles

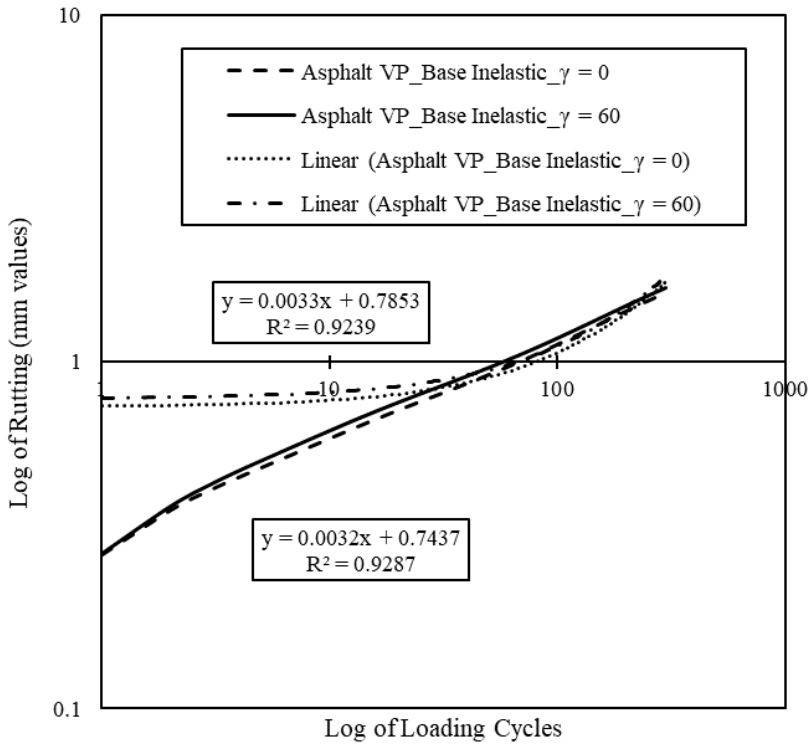

Figure 5.33: Rutting Prediction - Logarithmic

6. CONCLUSIONS AND RECOMMENDATIONS

In this research, a combined hardening modified Drucker-Prager elasto-plastic model has been proposed, which has a progressively evolving yield surface. Coupled with the PANDA constitutive relationships developed at the Texas A&M University, this model has the potential to better predict rutting in asphalt pavements. The following conclusions are drawn:

1. The existing Drucker-Prager elasto-plastic model cannot predict realistically the permanent deformations in asphalt concrete pavements in case of cyclic loading conditions.

2. The permanent deformations predicted on top of the pavement structure do not increase beyond the first few loading cycles because the granular base layer stops yielding.

3. For the case of pavement structures wherein only the base layer was inelastic and all other layers elastic, with the addition of combined hardening model for Drucker-Prager along with incorporation of $\gamma - factor$, equivalent plastic strain and vertical strains increased. This results in an increase in rutting.

   An increase in rutting of 49.95% was observed with $\gamma = 60$ in case of pavement section having friction angle, $\phi = 20°$; while 38.4% increase was observed for the same $\gamma - value$ for the case of $\phi = 30°$. These results establish the need for a continuously evolving yield surface for properly capturing rutting in a layered pavement system. Hence, it is observed that the permanent deformation continues to grow.

   The small increase is attributed potentially to limitations in modeling an input yield stress versus equivalent plastic strain curve, which is for a material from the literature, but not existing in a pavement runway or taxiway which was modeled in this dissertation work.

4. In cases wherein the asphalt layer was modeled using PANDA constitutive relationships, the addition of combined hardening model for Drucker-Prager along with incorporation of $\gamma - factor$ also resulted in the equivalent plastic strain and vertical strains increasing as

compared to the classical Drucker-Prager model used in the base layer. Consequently, rutting increased.

An increasing in rutting of 7.7% was observed with $\gamma = 60$ in case of pavement section having friction angle, $\phi = 30°$; while 0.58% increase was observed for the same $\gamma - value$ for the case of $\phi = 40°$. As observed above elsewhere in this section and also in case of layered pavement structure with only base layer inelastic, the results establish the need for a continuously evolving yield surface for properly capturing rutting in a layered pavement system. Hence, it is observed that the permanent deformation continues to grow.

The small increase is attributed potentially to limitations in modeling an input yield stress versus equivalent plastic strain curve, which is for a material from the literature, but not existing in a pavement runway or taxiway.

5. The results of this study show significant differences in rutting with the usage of the $\gamma - factor$, which results in a progressively evolving yield surface. However, it is noted that the absolute magnitude of rutting is a function of the input parameters. Availability of more refined and material-specific input parameters shall result in a more refined model. Since it is observed that the permanent deformation continues to grow, more refinements to the model shall be sought in future work.

Future research is required to improve the model. The following recommendations are made:

- The γ parameter needs a refinement in order to make the proposed model more realistic. This refinement may be sought by researching through the fundamentals of the granular base material's micro-mechanics and studies based thereof.

- Testing on the base material using monotonic loading is required in order to get the stress-strain curve that realistically simulates the field conditions.

- Reverse-mapping the monotonic test stress-strain curve by conducting cyclic tests and using a parameter which reverses the applicability of γ parameter is also recommended.

REFERENCES

[1] D. N. Little, D. H. Allen, and A. Bhasin, *Modeling and design of flexible pavements and materials*. Springer, 2018.

[2] J. W. Button, D. Perdomo, and R. L. Lytton, "Influence of aggregate on rutting in asphalt concrete pavements," *Transportation Research Record*, no. 1259, 1990.

[3] M. K. Darabi, R. K. A. Al-Rub, E. A. Masad, and D. N. Little, "A thermodynamic framework for constitutive modeling of time-and rate-dependent materials. part ii: Numerical aspects and application to asphalt concrete," *International Journal of Plasticity*, vol. 35, pp. 67–99, 2012.

[4] R. A. Schapery, "On the characterization of nonlinear viscoelastic materials," *Polymer Engineering & Science*, vol. 9, no. 4, pp. 295–310, 1969.

[5] P. Perzyna, "Thermodynamic theory of viscoplasticity," in *Advances in Applied Mechanics*, vol. 11, pp. 313–354, Elsevier, 1971.

[6] M. K. Darabi, R. K. A. Al-Rub, E. A. Masad, C.-W. Huang, and D. N. Little, "A modified viscoplastic model to predict the permanent deformation of asphaltic materials under cyclic-compression loading at high temperatures," *International Journal of Plasticity*, vol. 35, pp. 100–134, 2012.

[7] M. K. Darabi, R. K. A. Al-Rub, E. A. Masad, C.-W. Huang, and D. N. Little, "A thermo-viscoelastic–viscoplastic–viscodamage constitutive model for asphaltic materials," *International Journal of Solids and Structures*, vol. 48, no. 1, pp. 191–207, 2011.

[8] M. Shakiba, R. K. A. Al-Rub, M. K. Darabi, T. You, E. A. Masad, and D. N. Little, "Continuum coupled moisture–mechanical damage model for asphalt concrete," *Transportation Research Record*, vol. 2372, no. 1, pp. 72–82, 2013.

[9] R. K. A. Al-Rub, M. K. Darabi, S.-M. Kim, D. N. Little, and C. J. Glover, "Mechanistic-based constitutive modeling of oxidative aging in aging-susceptible materials and its effect

on the damage potential of asphalt concrete," *Construction and Building Materials*, vol. 41, pp. 439–454, 2013.

[10] E. Rahmani, M. K. Darabi, D. N. Little, and E. A. Masad, "Constitutive modeling of coupled aging-viscoelastic response of asphalt concrete," *Construction and Building Materials*, vol. 131, pp. 1–15, 2017.

[11] M. Shakiba, M. K. Darabi, R. K. A. Al-Rub, E. A. Masad, and D. N. Little, "Microstructural modeling of asphalt concrete using a coupled moisture–mechanical constitutive relationship," *International Journal of Solids and Structures*, vol. 51, no. 25-26, pp. 4260–4279, 2014.

[12] J. F. Rushing, M. K. Darabi, E. Rahmani, and D. N. Little, "Comparing rutting of airfield pavements to simulations using pavement analysis using nonlinear damage approach (PANDA)," *International Journal of Pavement Engineering*, vol. 18, no. 2, pp. 138–159, 2017.

[13] N. Garg and G. F. Hayhoe, "Permanent deformation behavior of the granular layers tested at the FAA's National Airport Pavement Test Facility," in *APT'08. Third International ConferenceCentro de Estudios y Experimentación de Obras Públicas (CEDEX) Transportation Research Board*, 2008.

[14] G. F. Hayhoe and N. Garg, "Posttraffic testing on medium-strength subgrade flexible pavements at the National Airport Pavement Test Facility," in *Airfield Pavements: Challenges and New Technologies*, pp. 136–146, 2004.

[15] N. Garg, F. Pecht, and Q. Jia, "Subgrade stress measurements under heavy aircraft gear loading at FAA National Airport Pavement Test Facility," in *Paving Materials and Pavement Analysis*, pp. 484–491, 2010.

[16] R. D. Barksdale, "Compressive stress pulse times in flexible pavements for use in dynamic testing," *Highway Research Record*, vol. 345, no. 4, pp. 32–44, 1971.

[17] C. L. Monismith, N. Ogawa, and C. Freeme, "Permanent deformation characteristics of subgrade soils due to repeated loading," *Transportation research record*, no. 537, 1975.

[18] G. T. Sweere, "Unbound granular bases for roads.," 1992.

[19] R. v. Mises, "Mechanics of solid bodies in the plastically-deformable state," *Göttin Nachr Math Phys*, vol. 1, pp. 582–592, 1913.

[20] M. Huber, "Specific work of strain as a measure of material effort, Towarzystwo Politechniczne," *Czas. Techniczne, Lwow*, 1903.

[21] H. Tresca, "Memoir on the flow of solid bodies under strong pressure," *Comptesrendus de l'académie des sciences, Paris, France*, vol. 59, p. 754, 1864.

[22] C. Coulomb, "Essai sur une application des rèles des maximis et minimis a quelques problems de statique," *Memoires Acad. Royale des Sciences*, vol. 7, 1776.

[23] D. C. Drucker and W. Prager, "Soil mechanics and plastic analysis or limit design," *Quarterly of applied mathematics*, vol. 10, no. 2, pp. 157–165, 1952.

[24] D. C. Drucker, "Soil mechanics and work-hardening theories of plasticity," *Trans. ASCE*, vol. 122, pp. 338–346, 1957.

[25] I. Sandler and D. Rubin, "An algorithm and a modular subroutine for the cap model," *International Journal for Numerical and Analytical Methods in Geomechanics*, vol. 3, no. 2, pp. 173–186, 1979.

[26] M. F. Saleh, B. Steven, and D. Alabaster, "Three-dimensional nonlinear finite element model for simulating pavement response: study at Canterbury accelerated pavement testing indoor facility, new zealand," *Transportation Research Record*, vol. 1823, no. 1, pp. 153–162, 2003.

[27] M. S. Mamlouk and M. Y. Mikhail, "Concept for mechanistic-based performance model for flexible pavements," *Transportation Research Record*, vol. 1629, no. 1, pp. 149–158, 1998.

[28] R. Bonaquist and M. W. Witczak, "Plasticity modeling applied to the permanent deformation response of granular materials in flexible pavement systems," *Transportation research record*, vol. 1540, no. 1, pp. 7–14, 1996.

[29] C. Desai, S. Somasundaram, and G. Frantziskonis, "A hierarchical approach for constitutive modelling of geologic materials," *International Journal for Numerical and Analytical Methods in Geomechanics*, vol. 10, no. 3, pp. 225–257, 1986.

[30] J. Uzan, "Permanent deformation of a granular base material," *Transportation Research Record*, vol. 1673, no. 1, pp. 89–94, 1999.

[31] P. Vermeer, "A formulation and analysis of granular flow," in *Proc. Int. Symp. Mech. Behavior of Structured Media, Ottawa, Part B*, pp. 325–339, 1981.

[32] P. Vermeer, "A double hardening model for sand," *Geotechnique*, vol. 28, no. 4, pp. 413–433, 1978.

[33] D. Rakić and M. Živković, "Stress integration of the Drucker-Prager material model with kinematic hardening," *Theoretical and applied mechanics*, vol. 42, no. 3, pp. 201–209, 2015.

[34] P. A. Allen, "Hydrostatic stress effects in low cycle fatigue," *A Dissertation Presented for the Doctor of Philosophy Degree, Tennessee Technology University*, 2002.

[35] N. Aravas, "Use of pressure-dependent plasticity models in ABAQUS," in *ABAQUS Users' Conference, Newport, Rhode Island*, 1996.

[36] C. O. Frederick and P. Armstrong, "A mathematical representation of the multiaxial Bauschinger effect," *Materials at High Temperatures*, vol. 24, no. 1, pp. 1–26, 2007.

[37] M. A. Buechler, "Viscoelastic-viscoplastic combined hardening constitutive model based on the drucker prager yield and flow potentials," tech. rep., Los Alamos National Lab.(LANL), Los Alamos, NM (United States), 2012.

[38] L. Prandtl, "Ein gedankenmodell zur kinetischen theorie der festen körper," *ZAMM-Journal of Applied Mathematics and Mechanics/Zeitschrift für Angewandte Mathematik und Mechanik*, vol. 8, no. 2, pp. 85–106, 1928.

[39] D. M. Smith, "Response of granular layers in flexible pavements subjected to aircraft loadings.," tech. rep., ENGINEER RESEARCH AND DEVELOPMENT CENTER VICKSBURG MS GEOTECHNICAL LAB, 2000.

[40] E. Rahmani, M. K. Darabi, R. K. A. Al-Rub, E. Kassem, E. A. Masad, and D. N. Little, "Effect of confinement pressure on the nonlinear-viscoelastic response of asphalt concrete at high temperatures," *Construction and Building Materials*, vol. 47, pp. 779–788, 2013.

[41] M. Bazzaz, M. K. Darabi, D. N. Little, and N. Garg, "A straightforward procedure to characterize nonlinear viscoelastic response of asphalt concrete at high temperatures," *Transportation Research Record*, vol. 2672, no. 28, pp. 481–492, 2018.

APPENDIX A

UMAT FOR THE CONSTITUTIVE MATERIAL MODEL

```
C Subroutine to compute DRUCKER-PRAGER COMBINED MULTILINEAR HARDENING
C Stress increments from strain increments.
C————————————————————————————————————————
SUBROUTINE UMAT(STRESS,STATEV,DDSDDE,SSE,SPD,SCD,
1 RPL,DDSDDT,DRPLDE,DRPLDT,
2 STRAN,DSTRAN,TIME,DTIME,TEMP,DTEMP,PREDEF,DPRED,CMNAME,
3 NDI,NSHR,NTENS,NSTATV,PROPS,NPROPS,COORDS,DROT,PNEWDT,
4 CELENT,DFGRD0,DFGRD1,NOEL,NPT,LAYER,KSPT,KSTEP,KINC)
C
INCLUDE 'ABA.PARAM.INC'
C
PARAMETER (ZERO=0.D0,ONE=1.D0,TWO=2.D0,THREE=3.D0,SIX=6.D0)
PARAMETER (ENUMAX=.4999D0,TOLER=1.0D-6,NEWTON=10000)
C
REAL SYIELD,EG,EG2,EG3,EBULK,EBULK3,ELAM,A,BETA,SYINIT,
+ SMISES,SHYDRO,DPYIEL,SYT1,SYT2,SYPREV,DEQPL,RHS,EQPLAS,
+ P,Q,DEP,DEQ,EFFG,EFFG2,EFFG3,EFFLAM,EFFHRD,TABLE,EQPL0,
+ SYIEL0,SYIEL1,DSYIEL,EQPLA2,EQPL1,DEQPLS,EMOD,ENU,
+ EPT1,GAPPA,SYT0,GAMMA,GAPP,SYT3,DPYIELN,SYPREVN,HBETA,
+ GAPP1,GAPPA1
C
CHARACTER*8 CMNAME
C
```

```
      DIMENSION STRESS(NTENS),STATEV(NSTATV),
     + DDSDDE(NTENS,NTENS),DDSDDT(NTENS),DRPLDE(NTENS),
     + STRAN(NTENS),DSTRAN(NTENS),TIME(2),PREDEF(1),DPRED(1),
     + PROPS(NPROPS),COORDS(3),DROT(3,3),DFGRD0(3,3),DFGRD1(3,3)
C
C LOCAL ARRAYS
C ——————————————————————————
C EELAS - ELASTIC STRAINS
C EPLAS - PLASTIC STRAINS
C AKPHA - SHIFT TENSOR
C FLOW - DIRECTION OF PLASTIC FLOW
C OLDS - STRESS AT START OF INCREMENT
C OLDPL - PLASTIC STRAINS AT START OF INCREMENT
C ——————————————————————————
C
      DIMENSION EELAS(6),EPLAS(6),ALPHA(6),FLOW(6),OLDS(6),OLDPL(6),
     + HARD(3),DEPLAS(6)
C
      DOUBLE PRECISION I1
C
C ——————————————————————————
C UMAT FOR ISOTROPIC ELASTICITY AND DRUCKER-PRAGER PLASTICITY
C WITH MULTILINEAR ISOTROPIC AND KINEMATIC HARDENING
C CANNOT BE USED FOR PLANE STRESS
C ——————————————————————————
C PROPS(1) - E
C PROPS(2) - NU
```

```
C PROPS(3) - A, DRUCKER-PRAGER CONSTANT, LET A=ZERO FOR
C CLASSICAL VON MISES PLASTICITY
C PROPS(4) - BETA, SCALAR PARAMETER TO DETERMINE
C PERCENTAGE OF EACH TYPE OF HARDENING
C 0.0 <= BETA <= 1.0
C PROPS(5) - GAMMA RATE OF YIELD SURFACE SIZE REDUCTION
C PROPS(6..) - SYIELD VS PLASTIC STRAIN DATA
C ———————————————————————————————
C
IF (NDI.NE.3) THEN
WRITE(6,*) '***ERROR - ONLY 3 DIRECT STRESS COMPONENT ALLOWED'
ENDIF
C
C ELASTIC PROPERTIES
C
EMOD=PROPS(1)
ENU=MIN(PROPS(2),ENUMAX)
EBULK3=EMOD/(ONE-TWO*ENU)
EG2=EMOD/(ONE+ENU)
EG=EG2/TWO
EG3=THREE*EG
ELAM=(EBULK3-EG2)/THREE
EBULK=EBULK3/THREE
C CONSTITUTIVE MODEL PROPERTIES
A=PROPS(3)
BETA=PROPS(4)
GAMMA=PROPS(5)
```

```
C READ INITIAL YIELD STRESS
SYINIT=PROPS(6)
C
C ELASTIC STIFFNESS
C
DO K1=1,NDI
DO K2=1,NDI
DDSDDE(K2,K1)=ELAM
END DO
DDSDDE(K1,K1)=EG2+ELAM
END DO
DO K1=NDI+1,NTENS
DDSDDE(K1,K1)=EG
END DO
C RECOVER ELASTIC AND PLASTIC STRAINS AND AND SHIFT TENSOR AND
C ROTATE NOTE: USE CODE 1 FOR (TENSOR) STRESS, CODE 2 FOR
C (ENGINEERING) STRAIN
C
CALL ROTSIG(STATEV( 1),DROT,EELAS,2,NDI,NSHR)
CALL ROTSIG(STATEV( NTENS+1),DROT,EPLAS,2,NDI,NSHR)
CALL ROTSIG(STATEV(2*NTENS+1),DROT,ALPHA,1,NDI,NSHR)
EQPLAS=STATEV(3*NTENS+1)
C SYPREVN=STATEV(3*NTENS+5)
C DPYIELN=STATEV(3*NTENS+6)
DO K1=1,NTENS
EELAS(K1)=STATEV(K1)
EPLAS(K1)=STATEV(K1+NTENS)
```

```
ALPHA(K1)=STATEV(K1+2*NTENS)
END DO
C
C SAVE STRESS AND PLASTIC STRAINS AND
C CALCULATE PREDICTOR STRESS AND ELASTIC STRAIN
C
DO K1=1,NTENS
OLDS(K1)=STRESS(K1)
OLDPL(K1)=EPLAS(K1)
EELAS(K1)=EELAS(K1)+DSTRAN(K1)
DO K2=1,NTENS
STRESS(K2)=STRESS(K2)+DDSDDE(K2,K1)*DSTRAN(K1)
END DO
END DO
C
C CALCULATE EQUIVALENT VON MISES STRESS
C
SMISES=(STRESS(1)-ALPHA(1)-STRESS(2)+ALPHA(2))**2
& +(STRESS(2)-ALPHA(2)-STRESS(3)+ALPHA(3))**2
& +(STRESS(3)-ALPHA(3)-STRESS(1)+ALPHA(1))**2
DO K1=NDI+1,NTENS
SMISES=SMISES+SIX*(STRESS(K1)-ALPHA(K1))**2
END DO
SMISES=SQRT(SMISES/TWO)
SHYDRO=(STRESS(1)+STRESS(2)+STRESS(3))/THREE
I1=SHYDRO*THREE
C EQUIVALENT DRUCKER-PRAGER STRESS
```

```
C
DPYIEL=SMISES+A*I1
C
C GET YIELD STRESS FROM THE SPECIFIED HARDENING CURVE
C
NVALUE=(NPROPS-5)/2
CALL UHARD(SYIELD,HARD,EQPLAS,EQPLASRT,TIME,DTIME,TEMP,
DTEMP,NOEL,NPT,LAYER,KSPT,KSTEP,KINC,CMNAME,NSTATV,
STATEV,NUMFIELDV,PREDEF,DPRED,NVALUE,PROPS)
C
C CALCULATE PREVIOUS YIELD VALUE AND DETERMINE IF
C ACTIVELY YIELDING
C
C STORE PREVIOUS TABLE VALUE FOR SYIELD
SYT1=SYIELD
GAPP=-GAMMA*EQPLAS
GAPPA=EXP(GAPP)
SYT0=SYT1*GAPPA
C BETA=HBETA*GAPPA
SYPREV=SYINIT+(SYT0-SYINIT)*BETA
C
C IF (DPYIELN.GT.DPYIEL) THEN
C SYPREV=SYINIT*GAPPA
C ELSE
C SYPREV=SYINIT+(SYT0-SYINIT)*BETA
C END IF
C
```

```
IF (DPYIEL.GT.(ONE+TOLER)*SYPREV) THEN
C
C ACTIVELY YIELDING
C SEPARATE THE HYDROSTATIC FROM THE DEVIATORIC STRESS
C CALCULATE THE FLOW DIRECTION
C
C
DO K1=1,NDI
FLOW(K1)=(STRESS(K1)-ALPHA(K1)-SHYDRO)/SMISES
END DO
DO K1=NDI+1,NTENS
FLOW(K1)=(STRESS(K1)-ALPHA(K1))/SMISES
END DO
C
C SOLVE FOR NEW YIELD STRESS
C AND EQUIVALENT PLASTIC STRAIN INCREMENT USING NEWTON ITERATION
C
SYIELD=SYPREV
DEQPL=ZERO
DO KEWTON=1,NEWTON
C
RHS=SMISES-SYPREV-(THREE*EBULK3*A*A+EG3)*DEQPL-SYIELD
& +A*I1+SYT1
DEQPL=DEQPL+RHS/(THREE*EBULK3*A*A+EG3+HARD(1))
EQPLA2=EQPLAS+DEQPL
CALL UHARD(SYIELD,HARD,EQPLA2,EQPLASRT,TIME,DTIME,
& TEMP,DTEMP,NOEL,NPT,LAYER,KSPT,KSTEP,KINC,CMNAME,
```

```
& NSTATV,STATEV,NUMFIELDV,PREDEF,DPRED,NVALUE,PROPS)
IF(ABS(RHS).LT.TOLER*SYPREV) GOTO 10
END DO
C
C WRITE WARNING MESSAGE TO THE .MSG FILE
WRITE(7,*) '***WARNING - DID NOT CONVERGE'
C
10 CONTINUE
C
C STORE THE CURRENT TABLE YIELD VALUE
SYT2=SYIELD
GAPP1=-GAMMA*EQPLAS
GAPPA1=EXP(GAPP1)
SYT3=SYT2*GAPPA1
C UPDATE THE EQUIVALENT PLASTIC STRAIN
EQPLAS=EQPLAS+DEQPL
C
C SOLVE FOR UPDATED YIELD STRESS
C
SYIELD=SYINIT+(SYT3-SYINIT)*BETA
C
C CALCULATE NEEDED CONSTANTS
C
P=(-EBULK*A*SYIELD-SHYDRO*EG+EBULK*A*SMISES)/(EBULK3*A*A+EG)
Q=(EBULK3*A*A*SMISES+SYIELD*EG-A*I1*EG)/(EBULK3*A*A+EG)
DEP=(A*(SMISES-SYIELD+A*I1))/(EBULK3*A*A+EG)
DEQ=(SMISES-SYIELD+A*I1)/(THREE*EBULK3*A*A+EG3)
```

```
C
C UPDATE STRESS, ELASTIC AND PLASTIC STRAINS AND SHIFT TENSOR
C
DO K1=1,NDI
C
ALPHA(K1)=ALPHA(K1)+(SYT2-SYT1)*FLOW(K1)*(ONE-BETA)
C
EPLAS(K1)=EPLAS(K1)+DEP/THREE+THREE*DEQ*FLOW(K1)/TWO
EELAS(K1)=EELAS(K1)-(DEP/THREE+THREE*DEQ*FLOW(K1)/TWO)
C
STRESS(K1)=ALPHA(K1)-P+Q*FLOW(K1)
END DO
DO K1=NDI+1,NTENS
C
ALPHA(K1)=ALPHA(K1)+(SYT2-SYT1)*FLOW(K1)*(ONE-BETA)
C
EPLAS(K1)=EPLAS(K1)+THREE*DEQ*FLOW(K1)
EELAS(K1)=EELAS(K1)-THREE*DEQ*FLOW(K1)
C
STRESS(K1)=ALPHA(K1)+Q*FLOW(K1)
END DO
C
C CALCULATE THE PLASTIC DISSIPATION
C
SPD=ZERO
DO K1=1,NTENS
SPD=SPD+(STRESS(K1)+OLDS(K1))*(EPLAS(K1)-OLDPL(K1))/TWO
```

```
END DO
C
C FORMULATE THE JACOBIAN (MATERIAL TANGENT)
C FIRST CALCULATE THE EFFECTIVE MODULI
C
EFFG=EG*SYIELD/SMISES
EFFG2=TWO*EFFG
EFFG3=THREE*EFFG
EFFLAM=(EBULK3-EFFG2)/THREE
EFFHRD=EG3*HARD(1)/(EG3+HARD(1))-EFFG3
DO K1=1,NDI
DO K2=1,NDI
DDSDDE(K2,K1)=EFFLAM
END DO
DDSDDE(K1,K1)=EFFG2+EFFLAM
END DO
DO K1=NDI+1,NTENS
DDSDDE(K1,K1)=EFFG
END DO
DO K1=1,NTENS
DO K2=1,NTENS
DDSDDE(K2,K1)=DDSDDE(K2,K1)+EFFHRD*FLOW(K2)*FLOW(K1)
END DO
END DO
ENDIF
C
C STORE ELASTIC STRAINS, PLASTIC STRAINS AND SHIFT TENSOR
```

```
C IN STATE VARIABLE ARRAY
C
DO K1=1,NTENS
STATEV(K1)=EELAS(K1)
STATEV(K1+NTENS)=EPLAS(K1)
STATEV(K1+2*NTENS)=ALPHA(K1)
END DO
STATEV(3*NTENS+1)=EQPLAS
STATEV(3*NTENS+2)=SYIELD
STATEV(3*NTENS+3)=DEQPL
STATEV(3*NTENS+4)=EQPLA2
STATEV(3*NTENS+5)=DEP
STATEV(3*NTENS+6)=DEQ
STATEV(3*NTENS+7)=GAPPA
C DO K2=1,NPROPS
C STATEV(3*NTENS+2+K2)=PROPS(K2)
C END DO
C
RETURN
END
```

APPENDIX B

ABAQUS UMAT FOR HARDENING

```
C CODING FOR SUBROUTINE UHARD
SUBROUTINE UHARD(SYIELD,HARD,EQPLAS,EQPLASRT,TIME,DTIME,TEMP,
& DTEMP,NOEL,NPT,LAYER,KSPT,KSTEP,KINC,CMNAME,NSTATV,
& STATEV,NUMFIELDV,PREDEF,DPRED,NVALUE,PROPS)
C
INCLUDE 'ABA.PARAM.INC'
C
CHARACTER*80 CMNAME
C
DIMENSION HARD(3),STATEV(NSTATV),TIME(*),PREDEF(NUMFIELDV)
DIMENSION TABLE(2,NVALUE),DPRED(*),PROPS(*)
C
PARAMETER(ZERO=0.D0)
C
REAL SYIELD,EG,EG2,EG3,EBULK,EBULK3,ELAM,A,BETA,SYINIT,
+ SMISES,SHYDRO,DPYIEL,SYT1,SYT2,SYPREV,DEQPL,RHS,EQPLAS,
+ P,Q,DEP,DEQ,EFFG,EFFG2,EFFG3,EFFLAM,EFFHRD,TABLE,EQPL0,
+ SYIEL0,SYIEL1,DSYIEL,EQPLA2,EQPL1,DEQPLS,EMOD,ENU,
+ EPT1,GAPPA,SYT0,GAMMA,GAPP
C
C FILL IN SY VS EQPLAS TABLE FROM PROPS ARRAY
I=6
DO K2=1,NVALUE
```

```
TABLE(1,K2)=PROPS(I)
TABLE(2,K2)=PROPS(I+1)
I=I+2
END DO
C SET YIELD STRESS TO LAST VALUE OF TABLE, HARDENING TO ZERO
SYIELD=TABLE(1,NVALUE)
HARD(1)=ZERO
C
C Search Table
C
IF(NVALUE.GT.1) THEN
DO K1=1,NVALUE-1
EQPL1=TABLE(2,K1+1)
IF(EQPLAS.LT.EQPL1) THEN
EQPL0=TABLE(2,K1)
IF(EQPL1.LE.EQPL0) THEN
WRITE(7,*)'***ERROR - ENTER IN ASCENDING ORDER'
CALL XIT
ENDIF
C CURRENT YIELD STRESS AND HARDENING
DEQPLS=EQPL1-EQPL0
SYIEL0=TABLE(1,K1)
SYIEL1=TABLE(1,K1+1)
DSYIEL=SYIEL1-SYIEL0
HARD(1)=DSYIEL/DEQPLS
SYIELD=SYIEL0+(EQPLAS-EQPL0)*HARD(1)
GO TO 10
```

```
ENDIF
END DO
10 CONTINUE
ENDIF
RETURN
END
```